

# Nature and timing of brittle structures at the Challenger Gold Mine

---

**Caitlin Rowett- corresponding author**

*Dept of Geology and Geophysics, School of Earth and Environmental Sciences*

*University of Adelaide, South Australia, 5005*

*caitlin.rowett@student.adelaide.edu.au*

**Prof. David Giles**

*Director, Centre for Mineral Exploration Under Cover, School of Earth and Environmental Sciences,*

*University of Adelaide, South Australia, 5005.*



**TABLE OF CONTENTS**

ABSTRACT.....	4
1.0 INTRODUCTION.....	6
1.1 Regional Geology .....	7
2.0 METHOD.....	13
3.0 RESULTS.....	16
3.1 Geometry of the Late Structures .....	16
3.2 Relationship to intrusions .....	19
3.3 Textures and Mineralogy of Alteration.....	20
3.4 <sup>40</sup> Argon/ <sup>39</sup> Argon Results.....	22
<i>CHALLENGER-880-8</i> .....	22
<i>CHALLENGER-880-9A</i> .....	23
<i>CHALLENGER-880-9B</i> .....	23
4.0 DISCUSSION.....	23
4.1 Significance of Argon Data .....	23
4.2 Interpretation of Fault Geometry .....	27
4.3 Regional Setting of Structures .....	31
4.4 Regional Setting of Lamprophyres.....	33
5.0 CONCLUSION.....	36
REFERENCES.....	38
ACKNOWLEDGEMENTS.....	41
FIGURE CAPTIONS.....	42
Figure 1: Background .....	42
Figure 2: Stereo-graphic representations of structural data .....	43
Figure 3: Photomicrographs.....	43
Figure 4: Wall Maps and Photos of Mapped Area .....	44
Figure 5: Field Observations .....	45
Figure 6: goCad® Model.....	46
Figure 7: Potential Model Geometry .....	46
Figure 8: Argon Age Plateau Plots.....	47
Figure 9: Interpretation of Stress and Strain .....	48
Figure 10: Cooling History of the Challenger Deposit.....	48
Figure 11: Geological History of Selected Gawler Craton Domains.....	49
TABLE CAPTIONS.....	49

---

Table 1: Joint Characteristics .....	49
APPENDICES .....	50
Appendix 1: goCad® Legend .....	50
Appendix 2: Wall and Backs Maps .....	51
Appendix 3: Challenger-880-8 Raw Data .....	66
Appendix 4: Challenger-880-8 Normal and Inverse Isochron .....	69
Appendix 5: Challenger-880-9a Raw Data .....	70
Appendix 6: Challenger-880-9a Normal and Inverse Isochron .....	73
Appendix 7: Challenger-880-9b Raw Data .....	74
Appendix 8: Challenger-880-9b Normal and Inverse Isochron .....	77
FIGURES.....	78
Figure 1: Background .....	78
Figure 2: Stereo-graphic Representations of Structural Data.....	80
Figure 3: Photomicrographs.....	81
Figure 4: Wall Maps and Photos of Mapped Area .....	82
Figure 5: Field Observations .....	84
Figure 6: goCad® Model representations and mapped data .....	85
Figure 7: Potential Model Geometries.....	87
Figure 8: Argon Age Plateau Graphs .....	88
Figure 9: Interpretation of Stress and Strain .....	90
Figure 10: Cooling History of the Challenger Gold Mine .....	91
Figure 11: Geological History of Selected Gawler Craton Domains.....	92

## ABSTRACT

The Challenger Gold Mine in the western Gawler Craton exhibits brittle deformation features that post-date mineralisation. This study has looked at the geometric relationships of the observed joint sets and has identified a dominant shallowly north-east dipping thrust fault package with a crosscutting vertical joint set. In the 880rL, a lamprophyric sill is emplaced within the shallowly north-east dipping fault.

Structural observations were made over 40 vertical metres in three of the underground mining levels the 920rL, the 900rL and the 880rL. Observations of these structural features culminated in the production of an interpreted 3D model using goCad® showing the connection of the fault package between the mapped levels. These observations in conjunction with alteration information and structural data showed that the fault network had a consistent dip across the package despite the undulations in the fault plane and that the series of splays observed linked the package together. The displacement and structural data both concluded that the shallowly north-east dipping fault network is a brittle deformation thrust system.

Three biotite samples from the lamprophyre were analysed using  $^{39}\text{Ar}/^{40}\text{Ar}$  Argon Thermochronology. Challenger-880-8 shows a plateau with 90% of cumulative  $^{39}\text{Ar}$  released between 1750 Ma and 1900 Ma. Challenger-880-9a produced a plateau using 55% cumulative  $^{39}\text{Ar}$  realised between 1800 Ma and 2100 Ma. Challenger-880-9b produces a plateau at 1860 Ma using five continuous steps where 45% of Cumulative  $^{39}\text{Ar}$  is released. Sample Challenger-880-9a provided an approximate crystallisation age of 1950 Ma. This is a coarser grained sample from close to the lamprophyre centre and produced a poorly defined plateau and consequently is thought to represent the minimum age of crystallisation. Challenger-880-9b and Challenger-880-8 both are fine grained samples from

the chill margin of the lamprophyre and present ages of approximately 1860 Ma. This is interpreted as an age of structural significance associated with the Cornian Orogeny, illustrating reactivation along the fault package during the Paleoproterozoic which had not been previously recognised in the western Gawler Craton.

The lamprophyre intruded into a pre-existing fault indicating that the shallowly north-east dipping fault package is older than 1950 Ma (the age of crystallisation). This provides information regarding the early-mid Paleoproterozoic in the western Gawler Craton.

**Key Words:** Challenger Gold Mine, Structural Analysis,  $^{40}\text{Ar}/^{39}\text{Ar}$  Thermochemistry, Paleoproterozoic Gawler Craton

## 1.0 INTRODUCTION

Faults define fundamental architecture for both Orogenic events and basin development accommodating a significant component of strain during deformation. In addition they are often the focus for intraplate deformation by exploiting crustal weaknesses (Hand & Sandiford 1999). Faults have been observed to cause lithospheric weakening and as a result are the sites of reactivation in varying extensional and compressional events (Hand & Sandiford 1999).

Faults also have the potential to be used as conduits for melts and hydrothermal fluids (Barton *et al.* 1995; Caine *et al.* 1996). Brittle fault zones are a primary control on the permeability of the rock type and can act as either conduits or barriers for fluid (Caine *et al.* 1996) as a result of connectedness, movement direction and hydraulic conductivity (Barton *et al.* 1995). A record of fluid movement along faults is often preserved by some combination of veining (Brown & Bruhn 1996), hydrothermal alteration of the fault zone and wall rock (Curewitz & Karson 1997) or in the case of melt migration by the preservation of igneous rocks (dykes and sills) in the fault zone (Murphy 2006).

Structural features of ore deposits have long been studied and used as an exploration tool, of particular interest are associations between fault movement and mineralisation for which we require an understanding of fault geometry, connectivity kinematics and timing. A strong understanding of such features is critical in determining deposit shape and style, fluid transport, predicting potential offsets and determining paleo-stress directions (Miller & Wilson 2002, 2004a). These exploration techniques are also vital to determine the offset within a deposit which has been dismembered (Miller & Wilson 2004b). A key problem associated with the study of faults and shear zones is the accurate dating of deformation. This is due to the lack of fault rocks which can be dated by Electron

Spin Resonance spectroscopy (Buhay *et al.* 1988) or in the case of ductile rocks which can be dated using isotopic methods (Eide *et al.* 1997). Brittle fault rocks are more difficult to date using standard isotopic methods than ductile fault rocks due to their low temperature and associated open system (Eide *et al.* 1997).

This project aims to produce a detailed analysis of the brittle deformation structures associated with the Challenger Gold Mine in the Gawler Craton, South Australia. An analysis of the surrounding joints sets, linking structures and provide a regional context. The data collected throughout this project can be of both geotechnical and economic benefit. The project links the Christie Domain's structural geology with that of the Challenger deposit through the dating of the lamprophyre in order to constrain the age of the late fault set. Challenger provides one of the few outcrops within the domain and therefore this information will have regional significance.

### **1.1 Regional Geology**

The Challenger Gold Mine is situated approximately 1180km northwest of Adelaide, in the Gawler Craton South Australia (Tomkins & Mavrogenes 2002). The Gawler Craton has had a long tectonic and metamorphic history, dominated by two major periods of tectonic activity, the late Archean and the late Paleoproterozoic to early Mesoproterozoic (Hand *et al.* 2007).

The Archean period is associated with basin development in the Gawler Craton with arc-like felsic magmatism, localised mafic to ultra-mafic magmatism (Hand *et al.* 2007). It was during the Archean that the Christie Gneiss which plays host to the Challenger Gold Deposit was developed (Tomkins & Mavrogenes 2002). The Christie Gneiss comprises banded-iron-formation, cordierite-garnet gneiss, layered calc-silicate rocks, marble (locally

dolomite), basic gneiss and a quartzite (Tomkins & Mavrogenes 2002). At the Challenger site the host rock is known as the Challenger Gneiss which is defined as pelitic garnet-biotite gneiss with varying amounts of cordierite and orthopyroxene (Tomkins & Mavrogenes 2002). At a mine scale there are 6 different types of gneiss logged based on differences in texture and mineralogy. These have been interpreted as granulite facies metasedimentary rocks with interbedded pelitic and psammopelitic sediments.

The Challenger deposit was metamorphosed during the Sleafordian Orogeny. The Sleafordian Orogeny occurred during the Archean with prograde metamorphism occurring at approximately 2460 to 2440 Ma (Reid *et al.* 2008). This is followed by the Kimban Orogeny at approximately 1730-1700 (Reid *et al.* 2008), which was concurrent with the Strangeways Orogeny in Central Australia (Betts & Giles 2006). Within the literature there is some ambiguity over the exact dates of the Kimban Orogeny, with some authors believing there were 3 phases of deformation recorded (Hand *et al.* 2007). During the Kimban Orogeny deformation was most intense along the eastern edge of the Galwer Craton (within the Hutchinson Group). However, deformation and metamorphism was regional, affecting the entire Craton (Betts & Giles 2006). The early stages of the orogeny observed on the Eyre Peninsula, were subjugated by transpressional deformation, illustrated by dextral top to the north shearing and contemporary north-south shearing (Vassallo & Wilson cited in Betts & Giles 2006). This resulted in orogen parallel shear zones and crustal scale sheath folds (Vassallo & Wilson cited in Betts & Giles 2006).

Prior to the commencement of the Kararan Orogeny approximately 1570-1540 Ma (Hand *et al.* 2007) the Ifould and the Tunkillia Suites were emplaced along the western edge of the Craton (Betts & Giles 2006). This orogenic event follows the emplacement of the Gawler Range Volcanics and the Hiltaba Suite which are commonly associated with Cu, Au



and U mineralisation in the Olympic Dam region (Hand *et al.* 2007; Reid *et al.* 2008). Hand *et al.*, 2007 states that the youngest phase of deformation is observed between 1470 and 1450 Ma in the reactivation of shear zones and regional cooling.

Peak metamorphic conditions recorded in the Challenger Gneiss are  $\sim 7.5 \pm 1.5$  kbars and at least  $800^\circ\text{C}$  (Tomkins & Mavrogenes 2002). This was determined by Zircon U-Pb and garnet Sm-Nd dating which indicated that peak metamorphism was at  $\sim 2440$  Ma (Early Proterozoic) (Tomkins & Mavrogenes 2002). From correlation of the Challenger gneiss with the Christie gneiss it has been proposed that the peak metamorphic conditions could be associated with the Sleafordian Orogeny (2637-2300 Ma) (Tomkins *et al.* 2004).

The Archean basins and subsequent metamorphism and deformation have been interpreted as being associated with subduction related tectonism (Betts & Giles 2006; Reid *et al.* 2008). The Sleaford and Mulgathing complexes which host the Challenger deposit have had a complex history which has involved many rift and accretionary phases (Betts & Giles 2006). This has involved three main orogenic events, at least two accretionary phases, plate convergence and subduction events, with a late period of tectonic stabilisation within the structures of the western Gawler Craton (Swain *et al.* 2005). The Christie Gneiss which plays host to the Challenger Gold Mine is the dominant lithology of the Christie domain (Tomkins & Mavrogenes 2002). The domain is located in the northwest of the craton (Fig. 1c). The Christie domain has had a unique history and records some of the events which affected the Gawler Craton as a whole.

Subsequent to peak metamorphism the deposit and host rocks were overprinted by brittle faulting and the intrusion of mafic and lamprophyric dykes and sills. Preliminary  $^{40}\text{Ar}/^{39}\text{Ar}$  suggests cooling of the hot gneiss between approximately 2000 and 1500

Ma. However the timing of faulting, magmatism and exhumation is poorly constrained and relationships with Paleoproterozoic tectonics elsewhere in the Gawler Craton are unknown.

The Christie Domain is distinguished from adjacent domains in the Gawler Craton by a series of large shear zones (Tomkins *et al.* 2004; Direen *et al.* 2005). The northern boundary is defined by the Karari Shear Zone and the southern boundary is largely defined by the Tallacootra Shear Zone (Tomkins *et al.* 2004; Direen *et al.* 2005). The use of gravity and magnetic forward modelling has indicated that these shear zones form an imbricate oblique thrust stack with movement top to the west and left lateral transport (Direen *et al.* 2005). The Challenger sub-domain is centrally located and between two interpreted subsidiary faults (Fig. 1c). These are the Tallacootra shear zone and the Coorabie fault zone (Direen *et al.* 2005). The Coorabie fault zone is a nucleus for splaying faults (Direen *et al.* 2005).

Interpretation of structural relationships have suggested that these features occurred after ca. 1590 Ma (Direen *et al.* 2005). This period of tectonic reworking has been associated with the stabilisation of Rodinia in the Proterozoic based on the metamorphism and deformation in the Gawler Craton between ca. 1550 and 1450 Ma (Direen *et al.* 2005).

As a result of recent above ground drilling a large brittle fault has been identified intersecting the Challenger deposit at approximately the 220rL (Reid *et al.* 2010). This fault has been observed to show left lateral transport of between 120 to 150m (Reid *et al.* 2010). This offset was determined by the use of the ore body as indicators on each side of the fault (Reid *et al.* 2010). Through the use of K-Ar Thermochronology on a sample of fault gouge this faulting event has been dated at  $1405 \pm 28$  Ma which infers that the area was approximately 2km below the Earth's surface at that time (Reid *et al.* 2010).

Geochronology work carried out at Challenger provides a timeline of events that shaped the metamorphic evolution of the deposit and regionally the effects of the Kimban and Sleafordian orogenies on the Christie/Challenger Gneiss (Tomkins *et al.* 2004). In addition to the geochronology described above, work was carried out on biotite, white mica and potassium feldspar using argon-argon analysis (Tomkins *et al.* 2004). The minerals being tested came from three samples of Challenger Gneiss unaffected by subsequent deformation and two samples that had been strongly altered by a fluid infiltration event (Tomkins *et al.* 2004).

This argon analysis provided inconclusive dates for the initial closure of the minerals. This can be observed on the age spectrum charts (Fig.1(d)). These show there is no distinct plateau in argon loss which would provide more consistent ages (Tomkins *et al.* 2004). The analyses conducted on the micas show no overlap in dates, including the error margins (Tomkins *et al.* 2004). Tomkins *et al.* (2004) concluded that the argon could have been partially reset by a series of short-lived moderate heating events after the initial closure. Consequently, the inconclusive nature of the results has meant that the Kimban and the Kararan orogenies cannot be resolved from one another (Tomkins *et al.* 2004).

Other geochronology work done by Tomkins and Mavrogenes (2002) was conducted using Sm-Nd dating of garnet. These whole rock ages identify the rocks as Archean (Tomkins & Mavrogenes 2002).

The Challenger ore body is defined by a laterally extensive shear zone with the ore shoots plunging at  $\sim 30^\circ$  ( $30^\circ$ - $35^\circ$ ) (Andrović *et al.* 2008). The ore body has been defined as four distinct regions these are the M1, M2, M3 and the M1 Shadow zone (DML, 2010). Current exploration has concluded that the high-grade gold-bearing M1, M2, and M3 shoots

extend to considerable depths (DML, 2010). The ore body is characterised by a series of tightly folded leucosomes which show ptygmatic folding (Andrović *et al.* 2008). Specifically the M1 ore shoot is an anticlinal fold that is defined by a package of upright tightly folded quartz veins and leucosomes, the fold axes of this package are parallel to the ore shoot at 30° towards 60° (Andrović *et al.* 2008).

The ore shoot lithologies are a dark-grey granoblastic garnet-cordierite proximal gneiss with locally elevated arsenic, metatexite migmatites containing 30-40% coarse grained stromatic leucosomes and bluish quartz-rich veins (McFarlane *et al.* 2007). These proximal lithologies contain disseminated pyrrhotite, arsenopyrite, löllingite, chalcopyrite, pentlandite, gold and bismuth (McFarlane *et al.* 2007). Other lithologies encountered at Challenger include late mafic-ultramafic dykes and sills (Tomkins *et al.* 2004). These have been observed to crosscut the gneissic foliation and exploit the joint networks. The dykes and sills have been affected by greenschist facies retrograde metamorphism where muscovite and chlorite have replaced all minerals, except quartz (Tomkins *et al.* 2004). This localised metamorphism has been attributed to competency contrasts between the mafic intrusions and the Challenger Gneiss developed when the fluid intruded (Tomkins *et al.* 2004).

## 2.0 METHOD

I collected Challenger field data while mapping wall and backs over three underground levels, i.e. the 880rL, 900rL and the 920rL. In the course of the project a total of 2110 m<sup>2</sup> was mapped. Maps were created using a 1:100 ratio with metres derived from distance from survey station. Mapping had a focus on the geometric relationships of joints, dip and dip direction data, displacement of gneissic features, size of joint planes and the scale of these interactions. An example of this can be observed in appendix 2.

In conjunction with the mapping, a series of field observations identifying displacement and characteristics of the fault plane, paying specific attention to texture, mineralogy along the plane, degree of infill and rock type. Further diagrams were produced that show small scale features such as linking structures and kinematic features. Structural information was presented using Georient<sup>®</sup>. The joint sets were plotted as both poles to planes and as planes. This information was subsequently plotted with the mineral lineations to indicate movement direction and to confirm data validity.

I selected a series of petrographic samples to show the progression of alteration into a joint and how it is changed along the joint margins. These were selected as representatives of the changes in the Challenger Gneiss, the lamprophyre and the mafic intrusion. The mafic sample was collected from the 360rL to confirm the difference between the lamprophyre and the mafic intrusion. One lamprophyre sample was collected from outside the mapping area to illustrate an example of a wide lamprophyric sill, all other samples were from the 3 mapped levels. Mineralogy, textural features and micro-tectonics were determined using an optical microscope.

I constructed a 3D model of the joint geometry using goCad<sup>®</sup> modelling software. Each wall map was imported and aligned with the wall segments in the solid polygons

representing the 880rL, 900rL and 920rL. Using the survey station and associated distances the maps were correctly aligned and the joints were digitised onto the level solid (provided by Dominion Survey). The dip data was imported onto the joint planes and represented as a disc, which allowed for surfaces to be created linking the joints. Like joints were linked across the drives and throughout the levels. Where readings were consistent some interpretation was made to link features between levels and across drives.

Argon-argon analysis was conducted on biotite grains from within three samples from a lamprophyre in the 880rL. These samples I prepared at the University of Adelaide. The samples were coarsely crushed and sieved using a 1mm mesh. Following this the fines were panned saving the light fraction. This light fraction was then dried and separated using the Frantz magnetic separator at 0.5 and 0.8 mV. Large impurities were removed from the heavy fraction using a microscope, leaving a pure biotite sample.

The samples were then sent to the West Australian Argon Isotope Institute for analysis, where three representative samples from Challenger Gold Mine samples Challenger-880-8, Challenger-880-9A and Challenger-880-9B were selected by them for  $^{40}\text{Ar}/^{39}\text{Ar}$  dating and separated into 580x310 $\mu\text{m}$  and 520x320  $\mu\text{m}$  sized single biotite grains for sample Challenger-880-9A and Challenger-880-9B respectively. For sample Challenger-880-8 a few smaller biotite grains were selected. These minerals were further separated using a Frantz magnetic separator before being carefully handpicked under a binocular microscope. The selected biotite grains were then thoroughly rinsed using distilled water in an ultrasonic cleaner.

The selected samples were loaded into 3 large wells with a 1.9cm diameter and 0.3cm depth aluminium disc. These wells were bracketed by smaller wells that contained Fish Canyon sanidine (FCs) which was used as a neutron fluence monitor for which an age of

28.305±0.036 Ma (1 $\sigma$ ) was adopted (Renne *et al.* 2010) based on the calibration by (Jourdan & Renne 2007). The aluminium discs were cadmium-shielded (to minimise nuclear interference reactions) and irradiated for a period of 25 hours in the Hamilton McMaster University (Canada) nuclear reactor in position 5C.

Mean J-values of  $0.0095820 \pm 0.0000517$  (0.54%) were computed from standard grains within the small wells. These were determined to be the average and standard deviation of the J values of the standards for each radiation disc. Mass discrimination was monitored using an automated air pipette and provided a mean value of 1.002703 n(0.28%) per dalton (atomic mass unit) relative to an air ratio of  $298.56 \pm 0.31$  (Lee *et al.* 2006). The correction factors for interfering isotopes were  $(^{39}\text{Ar}/^{37}\text{Ar})_{\text{Ca}} = 7.30 \times 10^{-4}$  ( $\pm 11\%$ ),  $(^{36}\text{Ar}/^{37}\text{Ar})_{\text{Ca}} = 2.82 \times 10^{-4}$  ( $\pm 1\%$ ) and  $(^{40}\text{Ar}/^{39}\text{Ar})_{\text{K}} = 6.76 \times 10^{-4}$  ( $\pm 32\%$ ).

The Western Australian Argon Isotope Institute is operated by a consortium consisting of Curtin University and the University of Western Australia, where I assisted in data acquisition. Sample 8 was wrapped in O-blank Niobium foil to create a package of grains whereas samples 9A and 9B were single grain analyses and step-heated using an 110W Spectron Laser Systems, with a continuous Nd-YAG (IR; 1064 nm) laser rastered over the package during 1mn to ensure a homogenously temperature distribution. The gas was purified in a stainless steel extraction line using a GP50 and 2 AP10 SAES getters and a liquid nitrogen condensation trap. Argon isotopes were measured in static mode using a MAP 215-50 mass spectrometer (resolution of  $\sim 500$ ; sensitivity of  $4 \times 10^{-14}$  mol/V) with a Balzers SEV 217 electron multiplier generally using 9 to 10 cycles of peak-hopping.

The data acquisition was performed using the Argus program written by M.O. McWilliams and ran under a LabView environment. The raw data were processed using the ArArCALC software (Koppers 2002) and the ages have been calculated using the decay

constants described by Renne *et al.* (2010). Blanks were monitored every 3 to 4 steps with typical  $^{40}\text{Ar}$  blanks ranging from  $1 \times 10^{-16}$  to  $2 \times 10^{-16}$  mol. Argon isotopic data which were corrected for blank, mass discrimination and radioactive decay are given in appendix 3.

The criteria used for the determination of plateaus are as follows:

- Plateaus must include at least 70% of  $^{39}\text{Ar}$ .
- The plateau should be distributed over a minimum of 3 consecutive steps with a 95% confidence level and satisfying a probability of fit (P) of at least 0.05.
- Plateau ages (appendices 3,5 and 7 and Fig.8) are given at the  $2\sigma$  level and are calculated using the mean of all the plateau steps, each weighted by the inverse variance of their individual analytical error.

Mini-plateaus are defined using similar features except that they include between 50% and 70% of  $^{39}\text{Ar}$ . Integrated ages ( $2\sigma$ ) are calculated using the total gas released for each Argon isotope and inverse isochrons include the maximum number of steps with a probability of fit  $\geq 0.05$ . All sources of uncertainties have been accounted for within the calculation.

## 3.0 RESULTS

### 3.1 Geometry of the Late Structures

Three main joint sets have been observed in the Walls and Backs at Challenger. These are the shallowly dipping joints and one set of conjugate vertical joints. The shallowly dipping joints have a range of dips from approximately north to east with an average of approximately north-east with east-west trending vertical joints. The joint sets are seen to crosscut one another with minor displacement to the vertical joints observed. The vertical



joints had two main orientations at approximately 90° to each other. A third set of joints was not observed in the 880rL and consequently has been deemed a minor feature.

A common feature of all the joints observed was their tendency to form splays from a dominant joint. The shallowly north-east dipping faults often occurred in packages with a dominant fault plane that had a series of splays linking to form a duplex-like structure (Fig. 5(c&d)). Another feature common to the joint sets was the presence of shear bands which vary in thickness from 10cm to 50cm and represent an area of intense deformation caused by continual splaying and linking between joints that follow the same general trend.

The observed large shallowly north-east dipping faults offset the quartz (qz) - veining and pegmatite emplacements. In the 900 Right Hand (RH) pillar the shallowly dipping joint offsets a pegmatite vein by approximately 3m (seen in the map and photo in Fig. 4(b)). This offset indicated a thrusting motion and was concluded to be a thrust fault with top to the north-east. An offset was also observed in the 920 RH drive where quartz veining that passed through both the left and right walls had been truncated by a shallowly dipping fault (Fig. 5(b)). However, the distance of the offset could not be quantified as the veining package could not be confidently identified in the drive. The movement along this same fault has produced brecciation of a large quartz-vein observed in the RH wall. This brecciation is shown in Fig. 5g where a change in the clast size can be observed towards the centre of the shear zone.

Occasional offsets were also observed along the vertical joints. These were on a much smaller scale approximately 2-5cm (as illustrated in Fig. 5(a & b)). Many of the vertical joints did not show signs of movement and were tightly closed.

Varying types of brittle deformation features were observed in the walls in conjunction with the brittle faults. In the 900 vent-return left hand (LH) wall boudinaging of

the qz-veining was observed (photo at Fig.5 (f)). Other structural features observed were a series of linking structures, which merge into one another along a specific plane (images available in Fig. 5 (c &d)).

In some situations the gneissic foliation was observed to follow the joint planes. In these cases the foliation became intensely strung out with mottled intergrowths of garnet and cordierite. Generally, the gneissic fabric has been disrupted by the jointing.

A key observation made about the joint sets was the level of undulation along the joint surface, particularly in the vertical joints which ran parallel with the walls. Along these joint planes large curvatures of the plane could be observed. These planes gave varying dip direction data, which in some cases varied by approximately 30 degrees such as in the 900 internal stockpile.

Four stereonet were produced showing the relationships between the joint sets and their associated mineral lineations (Fig. 2). Fig. 2a shows the measured joint planes and their associated mineral lineations. This image shows three distinct groups of joints. These three groups are further recognised in Fig. 2 b, c and d. In Fig. 2b the poles to planes were plotted, demonstrating a cluster of data on a central band. There is a concentration of data in the north to north-east quadrant and another minor grouping in the west to north-west quadrant. Fig.2c further confirms the three groups.

The band of data centrally located corresponds to the shallowly north-east dipping faults and the two other data populations correspond to the conjugate vertical joint sets. This density of data is also represented in Fig 2c which shows an example of a contoured density plot which indicates three zones of greater than 8% correlating to the joint sets described above.

Fig. 2d is a contoured density plot that illustrates the concentration of mineral lineations. This plot shows two regions of high density, one approximately 90° from the shallowly north-east dipping faults providing evidence for their movement direction. The second group is smaller in size and shows no specific alignment with a joint set.

Joint characteristics have been summarised in Table 1 which highlights three joint sets, the first two are the most dominant throughout the three mapped levels. With the set named vertical joint 2 being dominant in the 900rL.

### **3.2 Relationship to intrusions**

In the 880rL access right hand wall a lamprophyre sill is observed to be exploiting the shallowly dipping joint set (Fig. 4). In this wall two lamprophyre sills are observed, one is seen to run through into the neighbouring vent return and the other tapering off in the wall. The lower sill is observed to have a mineral lineation running along the base of the lamprophyre with an approximate strike of 70/230 SE. The joint plane at this location has a dip direction of 20/014. The lamprophyre was observed to be fine grained at the contact with the gneiss and gradually coarsening towards the centre of the sill. In some of the very narrow sills (approximately 10cm wide) the lamprophyres were very fine grained, with individual minerals undeterminable by the naked eye.

The lamprophyres have not seen major displacement and are only observed to be offset by a single joint where displacement is less than 10cm. The geometry of the lamprophyre system can be observed in Fig.4c where the lamprophyres can be seen to run along the shallowly dipping joint surfaces and link through linking structures. Within this level the lamprophyre is not observed without structural control.

Fine grained mafic intrusions were more common in the 920 and 900 levels. They showed intense jointing (of the intrusion) but were not seen to be exploiting the joint sets. The mafic intrusions have a distinct fracture pattern in which the mafic breaks off in circular fractures. In the 920 level the mafic intrusion was seen to be offset by the vertical joint set. Large gneissic inclusions are observed in the intrusions both the 920 and 900 levels. These inclusions did not follow the gneissic trend. In Fig.5(e) there is a small gneiss inclusion with quartz veining trending in a different direction to the surrounding veining.

### **3.3 Textures and Mineralogy of Alteration**

#### *Challenger Gneiss*

The Challenger Gneiss has a dominant composition of quartz, plagioclase, cordierite, biotite, and garnet with sericite alteration. The collected samples of gneiss: Challenger-900-1, Challenger-900-3, Challenger-900-4 and Challenger-880-2 are all dominantly granoblastic with no distinct foliation. Along the fracture planes there is a slight elongation to the garnet grains in some areas but this is not observed in all cases.

The gneiss shows the greatest alteration along joints of the three rock types. The gneiss shows a reduction in grain size closest to a joint surface. Moving from a joint plane the level of sericitisation also decreases, with the majority of sericitisation focused along the joint margin (Fig.3a). Sericitisation has preferentially occurred within the cordierite grains. This was particularly evident in sample Challenger-900-3 where a large altered cordierite grain is observed in hand specimen but is not observed in the thin-section, where at the same location sericite is abundant. The sericite was observed to be an alteration product and was subsequently observed close to the joint margin. This was particularly noticeable in

a fracture set which ran parallel to the joint plane in sample Challenger-900-3 where sericite had begun to infill these fractures.

Along the contact between the lamprophyre and gneiss (Fig.3e & f), is microcrystalline quartz which occurs in a very fine band. Other examples of microcrystalline quartz within fractures are observed (Fig.3a) where the individual quartz grains are approximately 10 microns in diameter and all exhibit undulose extinction.

The quartz grains provided the best evidence of movement along the joint planes. In sample Challenger-880-4 a series of splaying micro-fractures are observed coming from the lamprophyre gneiss contact. These micro-fractures dissect a series of quartz grains, within an individual grain there are three micro-fractures each showing a few  $\mu\text{m}$  of movement. This is illustrated in Fig.3(g) where the offset is demonstrated.

### *Mafic*

The mafic intrusion is a fine-grained igneous rock composed of abundant disseminated magnetite, biotite, chlorite and plagioclase with minor carbonate and sulphides. The groundmass is dominated by plagioclase lathes with biotite and chlorite intergrowths and euhedral fine grained magnetite. Dispersed throughout are minor groups of carbonates.

Sample Challenger-360-1 shows a veinlet of chalcopyrite indicating sulphide mineralisation does occur within the unit. A fracture running through the sample shows a concentration of magnetite along the feature, delineating the area. The magnetite has grown to fill in the fracture, producing larger grains. This area also shows a reduction in grain size of the biotite and the growth of sericite in the area. Other fractures observed are infilled by very fine grained sericite.

### *Lamprophyre-*

The lamprophyre is an intrusive igneous rock with an ultra-mafic mineral composition. The lamprophyre has an amphibole-rich matrix composed of acicular intergrown aegirine and sanderine/nepheline grains with minor biotite. Supported by the matrix are a series of olivine porphyroblasts, that are retrogressed to actinolite and tremolite, clinopyroxene (including diopside), orthopyroxene, and plagioclase (Fig 3b). The lamprophyre is dominantly fine grained in the narrow intrusions of the mapping area. In the larger sill sampled in the 640rL the lamprophyre is coarse grained with large porphyroblasts (Fig 3d).

These grain size reductions correspond with the size of the sill and the distance from the contact. In Fig. 3(c) an increase in grain size can be seen progressing away from the contact between the gneiss and the lamprophyre. Similarly the number of phenocrysts also increases away from the margins. The lamprophyre also exhibits a distinct foliation which can be observed bending around the phenocrysts (observed in Fig. 3 c).

## **3.4 <sup>40</sup>Argon/<sup>39</sup>Argon Results**

### *CHALLENGER-880-8*

This sample shows little evidence of contamination from atmospheric argon with an inverse isochron showing data clustered around 0.00 <sup>36</sup>Ar/<sup>40</sup>Ar ratio. The few outliers observed however all sit below 0.0020 <sup>36</sup>Ar/<sup>40</sup>Ar ratio. The age plateau (Fig. 8(a)) shows a gradual increase in the percentage of <sup>39</sup>Argon released with ages varying between approximately 1750 Ma and 1900 Ma with approximately 90% of <sup>39</sup>Argon being discharged in this range. A plateau-like region is reached using 13 of the sampled steps producing an

age of  $1851 \pm 14$  Ma (0.77%). This number is qualified by a MSWD of 1.14 and a probability of 0.32.

#### *CHALLENGER-880-9A*

This sample shows little contamination from atmospheric argon with all data on the inverse isochron plotting at 0.00  $^{36}\text{Ar}/^{40}\text{Ar}$  ratio. The age plateau (Fig. 8 (b)) shows an initial step at approximately 1100 Ma before increasing in age to 1800 Ma with the following step. A plateau-like feature is observed between 1800 and 2100 Ma during which 55% cumulative  $^{39}\text{Ar}$  is released. This produces an age of  $1944 \pm 45$  Ma ( $\pm 2.31\%$ ). This is qualified with a MSWD of 1.86.

#### *CHALLENGER-880-9B*

This sample shows no contamination from atmospheric argon with all data on the inverse isochron plotting at 0.00  $^{36}\text{Ar}/^{40}\text{Ar}$  ratio. The age spectrum (Fig. 8(c)) has an initial step at approximately 1400 Ma before increasing to approximately 1450 Ma. From this range the age significantly increases to approximately 1700 Ma before producing a plateau-like region at approximately 1860 Ma where 47% of the cumulative  $^{39}\text{Ar}$  is released. This sample produces an age of  $1861 \pm 16$  Ma ( $\pm 0.84\%$ ). Following this is a minor decline to approximately 1800 Ma. This data is qualified by a MSWD of 0.40.

## **4.0 DISCUSSION**

### **4.1 Significance of Argon Data**

Sample Challenger-880-9a was sampled close to the centre of the lamprophyric sill and consequently has a coarser grain size than the other two samples analysed. This sample provided a mean age of approximately 1950 Ma and a large standard deviation of 50 Ma. We interpret the degree of scatter to be the result of post-crystallisation isotopic

disturbance (possibly at 1860 Ma) and thus infer that rapid cooling following igneous crystallisation occurred prior to approximately 1950 Ma.

Samples Challenger-880-9b and Challenger-880-8 yielded plateau-like regions with ages of approximately 1860 Ma. These samples are observed in hand specimen and in thin section to have finer grained matrix than sample Challenger-880-9a. The fine-grained nature corresponds to the chilled margins caused by the temperature contrasts between the hot lamprophyric magma and the colder Challenger Gneiss at the time of intrusion. Within these margins a foliation can be observed (Fig. 3 c) which is thought to have developed during the faulting event which in turn has caused the mineral lineation observed on the lamprophyre when exposed in the fault plane.

Challenger-880-9b and Challenger-880-8 show a minimum age of 1860 Ma. Due to the location of these samples, the textural differences, the overprinting foliation and the replication of this result it is thought that the younger date is of structural significance. Further evidence for this is the idea that the chilled margins would cool quicker than the centre of the sill providing an older crystallisation age. This has not happened which supports an overprinting event. The lack of overprinting event provides further constraints on the timing of fault movement to be applied. As such the relationship of the lamprophyre and the fault implies that the lamprophyre was emplaced into an existing joint which infers that the fault must be older than 1950 Ma.

One of the benefits of  $^{40}\text{Ar}/^{39}\text{Ar}$  thermochronology is that it allows the determination of temperature from the closure temperature of the analysed mineral. The closure temperature of biotite is approximately 300°C with variation due to grain size and shape (McDougall & Harrison 1999). This information in conjunction the cooling history



developed by Tomkins *et al* (2004) and recent information from Reid *et al* (2010) has allowed revision of the cooling history of the Challenger area.

From the original cooling history produced by Tomkins *et al*, (2004) two data points have been excluded due to the inconclusive nature of the data (Fig. 10). One was a biotite sample that produced an age of 2060 Ma that had no obvious plateau in cumulative <sup>39</sup>argon released and was inconsistent with the other samples of biotite analysed during the 2004 study. The other sample excluded was a monazite grain. The rims of which provided an age of 1710 Ma, however the temperature at which the monazite rims grew is unknown. Monazite rims can grow in low temperature and pressure metamorphic conditions when there is a hydrothermal fluid present (Rasmussen *et al*. 2001). The reasoning for the assigned temperature is not provided by Tomkins *et al* (2004). Further concerns with the assigned temperature of 350°C are that the older biotite has not been reset, despite it being above the biotite closure temperature.

Muscovite is not a primary mineral within the Challenger Gneiss, and as such, the 1614 Ma age of the white mica (Tomkins *et al*. 2004), is thought to represent an alteration phase. Reid *et al* (2010), described this sample as sericite alteration along a mafic intrusion and suggested that the age relates to the crystallisation of the sericite in response to the presence of the mafic intrusion fluids. Similarly the 1950 Ma age from the biotite grain from the centre of the 880rL lamprophyre sill is thought to represent the crystallisation age of the biotite (Fig. 10).

The closure temperature of the Sm-Nd system within the garnets has been estimated at 850-750°C by Tomkins *et al* (2004). This closure temperature is consistent with the temperature used by Tomkins *et al* (2004) and takes into account the suggestion that garnets can preserve their Sm-Nd character up to 900°C (Cohen *et al*. 1988), that the

temperature of peak metamorphism was above 800°C (Tomkins & Mavrogenes 2002) and that age data indicates its after the peak metamorphism.

The closure temperature for un-mixed potassium feldspar (Ksp) is approximately 150°C. However, variation in grain size, shape and composition can greatly influence the temperature span over which argon gas is retained (Lovera *et al.* 2002);(McDougall & Harrison 1999). For example Lovera *et al.* (2002) demonstrates that closure temperatures can span window between approximately 300°C and 150°C, which is illustrated on Fig. 10 with large error bars on the Ksp samples.

The illite sample on Fig. 10, is a result of movement along the 79 fault at the approximate 200rL (Reid *et al.* 2010) and is thought to have an approximate closure temperature of 100°C (Roden *et al.* 1993).

The resultant cooling history (Fig. 10) is consistent with monotonic cooling between 2450 Ma and approximately 1860 Ma at a rate of approximately 1°C/Ma, followed by a period of slower cooling to 1400 Ma. However, a number of cooling paths cannot be ruled out in the interval 2450 Ma to 1860 Ma, including rapid cooling followed by reheating to approximately 350°C at 1860 Ma or rapid cooling at 1860 Ma after a period of prolonged high temperature.

A low temperature setting during faulting is supported by microcrystalline quartz that was identified within the Challenger Gneiss as fracture fill. This alteration style is considered an example of dynamic recrystallisation by Passchier & Trouw (2005). Movement along the fracture plane, however results in the internal lattices of the quartz grains becoming distorted producing the undulose extinction and the observed decrease in grain size.

Deformation is also observed within the cordierite grains. These grains are defined by their twins tapering towards the centre and being incomplete across the grain (fig 3a). All these features are described by Passchier and Trouw (2005) as evidence for deformation twinning. However, as there are relatively few preserved cordierite grains close to the joint planes, it has been concluded that these deformation features are evidence of a prior deformation event and are unconnected with the brittle joint features. The overprinting of the cordierite grains occurs close to the joint planes, where pinitisation of the cordierite grains is common. The pinitisation process is thought to be a retrograde reaction, where sericite is replacing the cordierite grain as a result of the change in pressure and temperature conditions resulting from the movement along the joint structures.

#### **4.2 Interpretation of Fault Geometry**

The Challenger Gold Mine shows evidence for two different joint sets and one fault set. The orientation and the geometry of the joints have helped to demonstrate the fault hierarchy and the interactions between the joint sets. The shallowly north-east dipping fault set has been deemed dominant due to the decimetre to metre offsets observed across the mapping area. In some situations the offset was unable to be quantified due to the drive lengths. The overall direction of shortening from the northerly Paleoproterozoic faults is north-east.

The shallowly north-east dipping faults showed, thrust movement with displacement in the 900rL indicating top block to the north-east. The mineral lineation data plots at approximately  $90^{\circ}$  from the poles to the fault plane, supporting the direction of thrust movement (Fig. 9(b & c)). The shallowly north-east dipping joints are shown to record large

displacements greater than 3m and as such are more accurately described as faults (Kearey 2001).

The vertical joints had two main orientations which were inferred as conjugates of one another. This was evident when looking at the mapped walls and seeing wedges of rock missing due to similarly angled faults dipping in the opposite direction. The change in dip of similarly angled joints was also observed in closed joints in the walls.

The geometric relationships of the joint sets have also helped to identify a relative time line for the observed brittle deformation. The shallowly north-east dipping faults have undergone very minor, non-systematic offsets caused by the vertical east-west joint sets. There are a number of possibilities for this relationship that would also explain the offsets observed to the other joint sets. It is possible that the surrounding joints have developed as a sympathetic form of brittle deformation in the weakened area (Fig. 9(a)). This could be in a similar manner as to how Riedel Structures form (Katz *et al.* 2004) or they possibly were the initial structures that developed, weakening the area allowing linking features to cut through and produce the fault network. Both possibilities suggest that the geometric relationship cannot be used to determine age relationships.

This fault network could have a number of different geometries such as those displayed in Fig. 7. Each of these models (Fig. 7) represent an end member whereas the interpreted model uses a combination of Fig. 7b and c as this represents the observed features best. The model produced in goCad® (Fig. 6a) uses the shallowly north-east dipping faults as the dominant set with at least two faults linked between the mapped levels. This interpretation is based on dip information and the knowledge the joints have undulating surfaces and that the faults have a tendency to splay off one another. Regardless of the

model selected the fault network has a consistent dip that can be projected through the mine levels.

The resultant model (Fig. 6a) shows that the fault network is an imbricate stack which includes splays that follow the same general trend as the dominant faults. The vertical joints in this model would be brittle structures formed as the result of the thrusting motion. These east-west trending features were not observed to link across levels however due to their dip direction information they would not have been seen in the corresponding levels.

The thrust fault network has variable dips from approximately northerly to easterly dipping. In some cases these variations may be splays of the dominant structure, and in others they are demonstrable undulations on a fault segment. Lohr *et al* (2008) stated that undulations in the principal fault surface are a result of growth and coalescence of the numerous segments through time. This has been interpreted as having occurred at the fault set at the Challenger Deposit. That is, a series of similarly orientated joint sets, with different episodes of movement linked to form the large shallowly north-east dipping faults. This is consistent with the large splaying features and the linking structures between joints observed across the mine infrastructure. This undulation in fault surface also explains the variation in dip direction measured across the same joint. The undulations are represented on the stereonet by poles to the fault surface distributed on a great circle with a pole to the great circle, parallel to the mineral lineation (Fig. 9(b)). The axes of undulations are parallel to the mineral lineation showing that the undulations are parallel to the movement direction.

The lamprophyre is observed to have a mineral lineation running along the top of the intrusion found within a joint plane. It was concluded that the lamprophyre was emplaced prior to movement along this fault plane. Grain size reduction of the lamprophyre

occurs progressing toward the joint planes. This reduction of grain size is thought to be related to the cooling history of the intrusion. When the lamprophyre is found in a wider sill such as observed in the 640rL, grain size is greatly increased. Evidence shows that the temperature contrast of the gneiss and the lamprophyric intrusion is the major control on grain size (Tomkins *et al.* 2004).

Greenschist facies metamorphism is observed in the rocks surrounding the fault planes due to the spatial relationship to the brittle deformation. The alteration was identified as greenschist facies due to the presence sericitic alteration surrounding the joint sets. The relationship between the distribution of lamprophyre in the shallowly north-east dipping fault network and the subsequent lack of crosscutting or displacement features in the lamprophyre, indicate that the faults were developed earlier or concurrently with the lamprophyre emplacement, suggesting fault development prior to 1950 Ma. The lineations on the lamprophyre indicate activity on the faults following the lamprophyre intrusion at approximately 1860 Ma. Therefore there were two events, with a minimum age of 1950 Ma and a second after emplacement at 1860 Ma.

Previous work carried out by Tomkins and Mavrogenes (2002) suggest that the localised retrograde metamorphism is the result of fluid infiltration along the competency contrasts between the gneiss and the intrusions. In some areas there is evidence of carbonate alteration in-filling fractures and brecciation along the joint planes which could be supporting evidence for movement of fluid along some joint sets or to support multiple periods of activity using these brittle features. However there is little evidence to support this across the mapping area as the joint sets are all mostly tightly closed with minor alteration on the joint plane. In some cases the movement has produced gouges instead of mineral lineations reflecting the low level of mineral development.

The lamprophyre displays some alteration properties such as the breakdown of olivine to actionolite and tremolite. This change in mineralogy is thought to be a result of the change in melt composition during crystallisation following the principles from Bowen's reaction series and the varying mineral stabilities (Winter 2010). However there is little retrograde metamorphism recorded within the lamprophyre found in the shallowly north-east dipping fault in the 880rL that correlates with the alteration observed in the adjacent Challenger Gneiss.

### **4.3 Regional Setting of Structures**

Since the peak metamorphism of the Sleafordian Orogeny at approximately 2440 Ma (Tomkins *et al.* 2004) the Challenger Deposit has undergone only low grade greenschist facies metamorphism. This lack of significant later thermal events would suggest that the Christie Domain was largely exhumed at the time of the Kimban and Kararan Orogenies which affected the surrounding Gawler Craton. From the geometry of the faults and the overprinting relationships observed in the mapping area, it has been interpreted that the lamprophyres intruded after the faults formed as they have not been crosscut or displaced and show the same level of alteration as the surrounding gneiss. This would suggest that the lamprophyres are syn-deformational.

The assumption that the faults are older than the lamprophyre crystallisation age of approximately 1950 Ma supports the suggestion that the Christie Domain was exhumed earlier than the Kimban and Kararan Orogenies. The brittle nature of the faults would suggest that they developed in the upper top 10 to 15km of the crust depending on the geothermal gradient and fluid presence in the local area (Davis & Reynolds 1996). The geothermal gradient within the Christie Domain is not known therefore it is hard to

constrain the depth of the deformation zones from the standard range of brittle deformation (Davis & Reynolds 1996).

The minimum age of 1860 Ma for movement along the fault corresponds with the timing of the Cornian Orogeny which has been approximated at 1850 Ma (Reid & Hand 2008) or 1860 Ma to 1850 Ma (Payne *et al.* 2006). This orogeny has previously been recorded only in the south-eastern Gawler Craton (Fig. 11), where the event has been characterised by emplacement of the Donnington Suite within a compressional tectonic setting (Reid & Hand 2008). Reid and Hand (2008) have interpreted the event as occurring over a 10 Ma window from 1850-1840 Ma with contractional deformation and peak metamorphism of amphibolite to granulite facies.

From the data collected at Challenger Gold Mine it could be suggested that the Cornian Orogeny had a much larger spatial distribution than originally thought. The focus of deformation may have been associated with the Donnington Suite in the south-east of the Gawler Craton (Fig. 11), and only brittle deformation occurring within the Christie Domain in the initial contractional phase. It is thought that rapid changes in subduction zone dynamics are the cause for the deformation observed in the south-east of the craton and these have an inboard reach of hundreds of kilometres from the subduction zone (Collins, cited in Reid & Hand 2008), which could also explain the deformation within the Christie Domain.

The areas that underwent the highest levels of deformation during the Cornian Orogeny reached pressure levels of 600 MPa and temperatures of 700°C (Payne *et al.* 2008), which are most likely to have occurred with depth. The lack of such high temperatures and pressures at the Challenger Deposit is consistent with the brittle deformation observed, being an upper crustal expression of the Cornian Orogeny.



Reid *et al* (2010) has proposed that brittle faulting along the 79 fault which offsets the Challenger ore body occurred at shallow depth of less than 2km. This suggests that the Christie Domain continued to be subjected to episodic fault activity and possibly exhumation into the Mesoproterozoic. The period of brittle deformation is consistent with the regional tectonic setting where reactivation of faults at this time was thought to be associated with a period of regional stabilisation (Swain *et al.* 2005). It commenced at approximately 1500 Ma when a series of faults and shear zone were active in the western Gawler Craton and persisted till approximately 1450 Ma (Swain *et al.* 2005). This is constant with the second thermal event observed on the argon plateaus in samples Challenger-880-9b which provided an approximate age of 1400 Ma.

#### **4.4 Regional Setting of Lamprophyres**

There is little consensus on the development of lamprophyres with many different settings identified as hosting lamprophyric intrusions. This may be due to the lack of a single definition or classification for ultra-mafic lamprophyres (Tappe *et al.* 2005). Winter (2010) described the lamprophyre group as being a repository for any difficult to characterise porphyritic rock and its exclusion from the International Union of Geological Sciences (IUGS) classification scheme (Tappe *et al.* 2005). As a result the term lamprophyre is used to describe many ultra-mafic alkaline porphyritic rock types. Without the chemical composition of the lamprophyre sampled it cannot be further classified but the petrographic data collected does provide a general idea of the composition and allows the assumption to be made that the lamprophyre is part of the general group.

The tectonic settings of alkaline rocks have been classified into three main settings by Srivastava & Chalapathi Rao (2007) (from (Blichert-Toft *et al.* 1996)): (i) continental rift

and intra-plate magmatism, (ii) oceanic intra-plate magmatism and (iii) alkaline magmatism related to subduction processes (island and continental arcs). With further analysis the Challenger lamprophyres can be potentially designated to one of these three broad categories through their chemical signature.

Lamprophyres are closely associated with some mesothermal gold deposits and are thought to be a transporting agent for gold from gold-rich mantle sources (Rock & Groves 1988). However, at Challenger the lamprophyre has not been associated with mineralisation and due to its relationship with the brittle deformation (which is observed crosscutting the mineralisation) it is considered a secondary event. The three samples which were analysed using  $^{40}\text{Ar}/^{39}\text{Ar}$  Thermochemistry provided crystallisation ages of later than 1950 Ma. This period within the Gawler Craton is generally thought to be a period of tectonic quiescence (Hand *et al.* 2007).

As the lamprophyre has intruded along an existing fault it can be assumed that the fault is older than the crystallisation age of the biotite grains within the lamprophyre. The gneissic foliation of the deposit can also be used as a control on the age of the fault, as the fault crosscuts the foliation and is a brittle deformation feature. It can be inferred that the gneiss was deformed and crystallised prior to the faults movement, providing a window of fault development prior to approximately 1950 Ma.

A possible explanation for the preferential emplacement of the lamprophyre within the fault network comes from the theory that lamprophyre magmatism is associated with deep faulting (Vaughn 1996). This idea fits with the observed features of the fault network and the proposed model of the fault network (Fig. 6).

Vaughn (1996) provides a model for the emplacement of lamprophyric and shoshonitic intrusions within Riedel Shear structures associated with primary shear zones.

As the lamprophyre found at the Challenger Deposit is found within a secondary splay feature off a dominant fault, a similar model for its development could be applied. However, as not all faults in the mapping area contain lamprophyre intrusions and in the absence of a significant vertical cross-section being observed it is impossible to note the systematic variations that may be related to the fault and/or the intrusion mechanism, when referring to the secondary features and consequently such a model is only speculative.

The generation of the lamprophyic magmas is thought to be a result of adiabatic decompression; resulting from a lithospheric scale fault which intersects the continental crust down to the mechanical boundary within the lithospheric mantle (Vaughn 1996). This boundary is located at the base of the cold rigid mantle anchor, which is attached to the base of the continental crust and through this area heat is transmitted via conduction (Vaughn 1996). The area directly below the mechanical boundary is a site of metasomatism where the potassium-rich intrusions have frozen and remain isolated for significant periods (Vaughn 1996). A series of methods have been suggested for the melting and migration of these intrusions. However, due to the conditions identified within the Gawler Craton at the time of the biotite crystallisation, the notion of adiabatic gradient changes as a result of a crustal scale faulting event seems the most plausible.

In the period preceding the intrusion of the lamprophyres the Gawler Craton is known to have experienced granulite facies metamorphism during the Sleafordian Orogeny (2637-2300 Ma) (Tomkins *et al.* 2004). This large scale orogenic event produced pressure and temperature conditions of approximately 9 kbars and temperatures between 800-860°C (Daly *et al.* 1998). The interpreted arc-back arc setting could provide a regional setting for the mantle wedge metasomatism from subduction.

The subduction of hot, young Archean crust may have been the source of potassium enrichment when the crust reached the melting conditions prior to becoming dehydrated (Martin 1986), allowing for the metasomatism of the mantle. Such conditions were thought to be associated with the generation of komatiites (Martin 1986), which in the past have been described as being genetically similar to lamprophyres (Rock 1977). This metasomatism is important in order to provide the chemical composition of the fluid required to produce a lamprophyre (Vaughn 1996).

The fault network being the path of least resistance acted as a focus for the potassium-rich magma. This melting during simple shear processes focuses melts within the fault, which acts as a conduit resulting in hydrostatic overpressure which facilitates rapid fluid extraction (Vaughn 1996). As the lamprophyres are preferentially found in sills of varying width throughout the mine it can be assumed that these represent the sites of percolation within features analogous to the Riedel Shear structures described by Vaughn (1996).

## **5.0 CONCLUSION**

The consequence of having multiple low angle faults is that care needs to be taken when there are multiple intersecting splays. However, as the fault network has a consistent dip throughout the package it allows the fault network to be easily predicted in the subsequent mined levels. These shallowly north-east dipping faults have been observed as the most problematic set for mining operations due to their shallow dip and the potential to cause rock-wedges where splays intersect one another. Of further concern are the presence of the lamprophyre within the fault plane and the alteration mineralisation of chlorite and sericite along the fault plane, potentially causing weakness along the fault.

The presence of a lamprophyre sill provided evidence about the potential for lithospheric mantle intersecting faults and the metasomatism of the mantle as a result of subducted material prior to the age of emplacement.

From the  $^{40}\text{Ar}/^{39}\text{Ar}$  thermochronology and the geometric relationships between the lamprophyre and the shallowly north-east dipping fault network, it has been concluded that these faults are Paleoproterozoic in age with development occurring prior to emplacement of the lamprophyres at approximately 1950 Ma. This minimum age of crystallisation is also thought to be overprinted by an event of structural significance at approximately 1860 Ma. The timing of this event is consistent with the Cornian Orogeny and is thought to show an upper crustal manifestation of the Cornian event. This data has provided important information about the Paleoproterozoic era in the western Gawler Craton where previously there has been very little information. This study provides important links between observed features elsewhere in the craton.

## REFERENCES

- ANDROVIC P., BAMFORD P. & SANDY M. 2008. The Challenger Gold Mine. *Narrow Vein Mining Conference Proceedings*, Ballarat Vic.
- BARTON C. A., ZOBACK M. D. & MOOS D. 1995. Fluid flow along potentially active faults in crystalline rock. *Geology* **23**, 683-686.
- BETTS P. G. & GILES D. 2006. The 1800-1100 Ma tectonic evolution of Australia. *Precambrian Research* **144**, 92-125.
- BLICHERT-TOFT J., ARNDT N. T. & LUDDEN J. N. 1996. Precambrian alkaline magmatism. *Lithos* **37**, 97-111.
- BROWN S. R. & BRUHN R. L. 1996. Formation of voids and veins during faulting. *Journal of Structural Geology* **18**, 657-671.
- BUHAY W. M., SCHWARCZ H. P. & GRÜN R. 1988. ESR dating of fault gouge: The effect of grain size. *Quaternary Science Reviews* **7**, 515-522.
- CAINE J. S., EVANS J. P. & FORSTER C. B. 1996. Fault zone architecture and permeability structure. *Geology* **24**, 1025-1028.
- COHEN A. S., O'NIONS R. K., SIEGENTHALER R. & GRIFFIN W. L. 1988. Chronology of the pressure-temperature history recorded by a granulite terrain. *Contributions to Mineralogy and Petrology* **98**, 303-311.
- CUREWITZ D. & KARSON J. A. 1997. Structural settings of hydrothermal outflow: Fracture permeability maintained by fault propagation and interaction. *Journal of Volcanology and Geothermal Research* **79**, 149-168.
- DALY S. J., FANNING C. M. & FAIRCLOUGH M. C. 1998. Tectonic Evolution and exploration potential of the Gawler Craton, South Australia. *AGSO Journal of Australian Geology and Geophysics* **17**, 145-168.
- DAVIS G. & REYNOLDS S. 1996. *Structural Geology of Rocks and Regions* (2nd edition). John Wiley and Sons, Inc.
- DIREEN N. G., CADD A. G., LYONS P. & TEASDALE J. P. 2005. Architecture of Proterozoic shear zones in the Christie Domain, western Gawler Craton, Australia: Geophysical appraisal of a poorly exposed orogenic terrane. *Precambrian Research* **142**, 28-44.
- EIDE E. A., TORSVIK T. H. & ANDERSEN T. B. 1997. Absolute dating of brittle fault movements: Late Permian and late Jurassic extensional fault breccias in western Norway. *Terra Nova* **9**, 135-139.
- HAND M., REID A. & JAGODZINSKI L. 2007. Tectonic Framework and Evolution of the Gawler Craton, Southern Australia. *Economic Geology* **102**, 1377-1395.
- HAND M. & SANDIFORD M. 1999. Intraplate deformation in central Australia, the link between subsidence and fault reactivation. *Tectonophysics* **305**, 121-140.
- JOURDAN F. & RENNE P. R. 2007. Age calibration of the Fish Canyon sanidine  $^{40}\text{Ar}/^{39}\text{Ar}$  dating standard using primary K-Ar standards. *Geochimica et Cosmochimica Acta* **71**, 387-402.
- KATZ Y., WEINBERGER R. & AYDIN A. 2004. Geometry and kinematic evolution of Riedel shear structures, Capitol Reef National Park, Utah. *Journal of Structural Geology* **26**, 491-501.
- KEAREY P. 2001. *The New Penguin Dictionary of Geology* (2nd edition). The Penguin Group.
- KOPPERS A. A. P. 2002. ArArCALC--software for  $^{40}\text{Ar}/^{39}\text{Ar}$  age calculations. *Computers & Geosciences* **28**, 605-619.

- LEE J.-Y., MARTI K., SEVERINGHAUS J. P., KAWAMURA K., YOO H.-S., LEE J. B. & KIM J. S. 2006. A redetermination of the isotopic abundances of atmospheric Ar. *Geochimica et Cosmochimica Acta* **70**, 4507-4512.
- LOHR T., KRAWCZYK C. M., ONCKEN O. & TANNER D. C. 2008. Evolution of a fault surface from 3D attribute analysis and displacement measurements. *Journal of Structural Geology* **30**, 690-700.
- LOVERA O. M., GROVE M. & HARRISON T. M. 2002. Systematic analysis of K-feldspar  $^{40}\text{Ar}/^{39}\text{Ar}$  step heating results II: relevance of laboratory argon diffusion properties to nature. *Geochimica et Cosmochimica Acta* **66**, 1237-1255.
- MARTIN H. 1986. Effect of steeper Archean geothermal gradient on geochemistry of subduction-zone magmas. *Geology* **14**, 753-756.
- MCDUGALL I. & HARRISON T. M. 1999. *Geochronology and Thermochronology by the  $^{40}\text{Ar}/^{39}\text{Ar}$  Method* (2nd edition). Oxford University Press, New York.
- McFARLANE C. R. M., MAVROGENES J. A. & TOMKINS A. G. 2007. Recognizing hydrothermal alteration through a granulite facies metamorphic overprint at the challenger Au deposit, South Australia. *Chemical Geology* **243**, 64-89.
- MILLER J. M. & WILSON C. J. L. 2002. The Magdala Lode System, Stawell, Southeastern Australia: Structural Style and Relationship to Gold Mineralization across the Western Lachlan Fold Belt. *Economic Geology* **97**, 325-349.
- MILLER J. M. & WILSON C. J. L. 2004a. Stress Controls on Intrusion-Related Gold Lodes: Wonga Gold Mine, Stawell, Western Lachlan Fold Belt, Southeastern Australia. *Economic Geology* **99**, 941-963.
- MILLER J. M. & WILSON C. J. L. 2004b. Structural analysis of faults related to a heterogeneous stress history: reconstruction of a dismembered gold deposit, Stawell, western Lachlan Fold Belt, Australia. *Journal of Structural Geology* **26**, 1231-1256.
- MURPHY J. B. 2006. Fault-controlled emplacement of arc-related magmas along the Neoproterozoic northern Gondwanan margin: An example from the Antigonish Highlands, Nova Scotia. *Precambrian Research* **147**, 305-319.
- PASSCHIER C. W. & TROUW R. A. J. 2005. Deformation Mechanisms *In, Micro-Tectonics* (2 edition), pp 25-66, Springer Berlin
- PAYNE J. L., BAROVICH K. M. & HAND M. 2006. Provenance of metasedimentary rocks in the northern Gawler Craton, Australia: Implications for Palaeoproterozoic reconstructions. *Precambrian Research* **148**, 275-291.
- PAYNE J. L., HAND M., BAROVICH K. M. & WADE B. P. 2008. Temporal constraints on the timing of high-grade metamorphism in the northern Gawler Craton: implications for assembly of the Australian Proterozoic. *Australian Journal of Earth Sciences: An International Geoscience Journal of the Geological Society of Australia* **55**, 623 - 640.
- POUSTIE T. 2009. *Challenger A Mine for the Geologist*
- RASMUSSEN B., FLETCHER I. R. & McNAUGHTON N. J. 2001. Dating low-grade metamorphic events by SHRIMP U-Pb analysis of monazite in shales. *Geology* **29**, 963-a-966.
- REID A. & HAND M. 2008. Aspects of Palaeoproterozoic orogenesis in the Gawler Craton: the c. 1850 Ma Cornian Orogeny. *MESA Journal* **50**, 26-31.
- REID A., HAND M., JAGODZINSKI E., KELSEY D. & PEARSON N. 2008. Paleoproterozoic orogenesis in the southeastern Gawler Craton, South Australia. *Australian Journal of Earth Sciences: An International Geoscience Journal of the Geological Society of Australia* **55**, 449 - 471.

- REID A., ZWINGMANN H. & GILES A. 2010. Constraints on the Timing of Brittle Faulting at Challenger Mine *In, Report Book 2010/00015*, Department of Primary Industries and Resources South Australia
- RENNE P. R., MUNDIL R., BALCO G., MIN K. & LUDWIG K. R. 2010. Joint determination of 40K decay constants and 40Ar\*/40K for the Fish Canyon sanidine standard, and improved accuracy for 40Ar/39Ar geochronology. *Geochimica et Cosmochimica Acta* **74**, 5349-5367.
- ROCK N. M. S. 1977. The nature and origin of lamprophyres: some definitions, distinctions, and derivations. *Earth-Science Reviews* **13**, 123-169.
- ROCK N. M. S. & GROVES D. I. 1988. Can lamprophyres resolve the genetic controversy over mesothermal gold deposits? *Geology* **16**, 538-541.
- RODEN M. K., ELLIOTT W. C., ARONSON J. L. & MILLER D. S. 1993. A Comparison of Fission-Track Ages of Apatite and Zircon to the K/Ar Ages of Illite-Smectite (I/S) from Ordovician K-Bentonites, Southern Appalachian Basin. *The Journal of Geology* **101**, 633-641.
- SRIVASTAVA R. K. & CHALAPATHI RAO N. V. 2007. Petrology, geochemistry and tectonic significance of Palaeoproterozoic alkaline lamprophyres from the Jungel Valley, Mahakoshal supracrustal belt, Central India *Mineralogy and Petrology* **89**, 189-215.
- SWAIN G. M., HAND M., TEASDALE J., RUTHERFORD L. & CLARK C. 2005. Age constraints on terrane-scale shear zones in the Gawler Craton, southern Australia. *Precambrian Research* **139**, 164-180.
- TAPPE S., FOLEY S. F., JENNER G. A. & KJARSGAARD B. A. 2005. Intergrating Ultramafic lamprophyres into the IUGS Classification of Igneous Rocks: Rationale and Implications *Journal of Petrology* **46**, 1893-1900.
- THOMAS J. L., DIREEN N. G. & HAND M. 2008. Blind orogen: Integrated appraisal of multiple episodes of Mesoproterozoic deformation and reworking in the Fowler Domain, western Gawler Craton, Australia. *Precambrian Research* **166**, 263-282.
- TOMKINS A. G., DUNLAP W. J. & MAVROGENES J. A. 2004. Geochronological constraints on the polymetamorphic evolution of the granulite-hosted Challenger gold deposit: implications for assembly of the northwest Gawler Craton\*. *Australian Journal of Earth Sciences* **51**, 1-14.
- TOMKINS A. G. & MAVROGENES J. A. 2002. Mobilization of Gold as a Polymetallic Melt during Pelite Anatexis at the Challenger Deposit, South Australia: A Metamorphosed Archean Gold Deposit. *Economic Geology* **97**, 1249-1271.
- VAUGHN A. P. M. 1996. A tectonomagmatic model for the genesis and emplacement of Caledonian clac-alkaline lamprophyres *Journal of the Geological Society, London* **153**, 613-623.
- WINTER J. D. 2010. *Principles of Igneous and Metamorphic Geology* (Second Edition edition). Prentice Hall New Jersey



## **ACKNOWLEDGEMENTS**

Sincere thanks go to my supervisor David Giles for all his help and knowledge in the course of this project. I would also like to thank Dominion Gold Operations for their financial and organisational support of this project, including all the people on site at Challenger including the Dominion Team and the HWE mining contractors. A special thank you goes to the Mine Geology Team in particular Paul Androvic, for their help with transportation, equipment and for sharing their vast knowledge on the deposit and the various aspects of geology.

Thank you to Dr Fred Jourdan at the West Australian Argon Isotope Facility for teaching me the intricacies of Argon Thermochronology and answering all my questions regarding the analysis. Thank you also to Dr Justin Payne for his help in preparing the biotite samples for analysis and for his discussions regarding the Gawler Craton.

Thank you to my family for all their love and support throughout the year. And finally thanks to the 2010 Geology Honours Class for making this a memorable year.

## FIGURE CAPTIONS

### Figure 1: Background

**Image (a):** Map of the Gawler Craton geology showing the locations of major mines in the region including Challenger Gold Mine within the Sleaford and Multhagating Complex. Image from Hand *et al* 2007

**Image (b):** Ore Shoot Geometry showing the shape of both the M1 and M2 ore bodies and the associated level development. Ore body folds are not shown down plunge. This image from Dominion Mining Limited presentation (Poustie 2009).

**Image (c):** The Christie Domain showing the location of Challenger and the regional shear zones. These structures have been interpreted from a Total Magnetic Intensity first vertical derivative image (seen on the right). The thick black lines indicate they have been partially ground-truthed, the grey and thin black lines are wholly interpreted. The grey and thin black lines show subsidiary faults and the general structural grain. Images from Tomkins *et al* 2004.

**Image (d):** (a) Age spectrum measured on biotite from sample AGT089. (b) Age spectrum measured on biotite from sample AGT090. (c) Age spectrum measured on biotite from sample AGT091. (d) Age spectrum measured on retrograde muscovite from sample AGT083. (e) Age spectrum measured on retrograde muscovite from sample AGT087. (f) Age spectrum measured on K-feldspar from sample AGT089. (g) Age spectrum measured on K-feldspar from sample AGT090. (h) Age spectrum measured on K-feldspar from sample AGT091. These show the different ages found for the pristine Challenger gneiss samples AGT 089-091 and sample affected by a late fluid intrusion AGT 083 and 087. Each of these samples has an extensive age range. Image from Tomkins *et al* 2004.

**Figure 2: Stereo-graphic representations of structural data**

**Image (a)** Stereo-graphic representation of the dip and dip direction data from the joint sets observed in the 920rL, 900rL and 880rL and their corresponding mineral lineation.

Plotted as the planes with the mineral lineation (purple dots) on the corresponding plane.

**Image (b)** Stereo-graphic representation of the dip and dip direction data from the joint sets observed in the 920rL, 900rL and 880rL plotted as poles to planes.

**Image (c)** Stereo-graphic representation of the dip and dip direction data from the joint sets observed in the 920rL, 900rL and 880rL plotted as poles to planes and contoured to show the density distribution of data.

**Image (d)** Stereo-graphic representation of the mineral lineation data from the joint sets observed in the 920rL, 900rL and 880rL plotted and contoured to show the density distribution of data.

**Figure 3: Photomicrographs**

**Image (a)** **Challenger 900-3 (CPL)** Challenger Gneiss showing evidence of dynamic recrystallisation within a fracture. There is also evidence of pinitisation (Sr) of the cordierite (Cd) grains and small fractures running parallel to the micro-crystalline quartz (Qz) infilled fracture.

**Image (b)** **Challenger 900-4 (CPL)** Challenger Gneiss showing irregular twinning within cordierite grains and sericitisation surrounding the grains.

**Image (c)** **Challenger 880-8 (CPL)** Contact between the Challenger Gneiss and the Lamprophyre. The Challenger Gneiss has been slightly gouged out by the lamprophyre and small inclusions of Quartz (Qz) and Plagioclase (plag) can be observed. The grain size can be

observed to increase away from the gneiss. The large porphyroblasts are thought to be Olivine (Ol) breaking down to actinolite (act) and tremolite (tre). The smaller porphyroblasts are clinopyroxene (cpx) and orthopyroxene (opx).

**Image (d)**      **Challenger 640-1** (CPL) Sample of Lamprophyre from a wide sill greater than 2m. The sample is coarse grained with large porphyroblasts of clinopyroxene (cpx) and orthopyroxene (opx), with a matrix dominated by Biotite (Bt).

**Image (e)**      **Challenger 880-8** (CPL) Contact between the Challenger Gneiss and the Lamprophyre. Showing microcrystalline quartz along the boundary and the fine grained nature of the lamprophyre at the margins.

**Image (f)**      **Challenger 880-8** (PPL) Contact between the Challenger Gneiss and the Lamprophyre. Showing the pleochroism of the Lamprophyre indicating the high biotite content.

**Image (g)**      **Challenger 880-8** (CPL) Contact between the Challenger Gneiss and the Lamprophyre. Showing micro-fractures along the boundary and the dissection of quartz (Qz) and garnet (gt) grains.

#### **Figure 4: Wall Maps and Photos of Mapped Area**

**Image (a)**      Map of the 880rL Access Right Hand Wall, metres from survey mark 01. The map illustrates the geometry of the lamprophyre (represented in green) and which joints it preferentially fills. In the figure purple represents pegmatite and hatching represents joint planes. The map also displays the dip and dip directions of major joints. Below is a photo compilation of the mapped wall.

**Image (b)**      Map of the 900rL Access Right Hand Wall pillar, metres from laser point. The map illustrates the dip of the joint planes, the offset in the pegmatite vein and the inferred

direction of movement. The pegmatite veins are indicated in purple with quartz veining displayed in grey. The direction of movement is illustrated by blue arrows with important dip and dip directions included. A photograph of the mapped area is displayed alongside.

**Image (c)** Map of the 880rL Right Hand Access entrance, metres from Survey mark 01. Showing the general trend of the lamprophyre sill and the locations of the two Lamprophyre samples used for  $^{40}\text{Ar}/^{39}\text{Ar}$  Thermochemistry (illustrated by red crosses and the corresponding sample number (8=Challenger-880-8 and 9=Challenger-880-9a +Challenger-880-9b)). Adjacent in the photo the pencil (~14cm) indicates the location of sample Challenger-880-9.

**Image (d)** Map of the 920rL Drive right hand wall, metres from survey mark 02. This map illustrates the length and nature of the flat lying fault structures and the relationships between the joints with important dip information displayed. Below is a photo compilation of the mapped walls.

**Image (e)** Map of the 900rL escape way, metres from survey mark 03 and laser 01. This map shows the undulations in the joint surfaces and the interaction of the veining and the joint sets. Below is a photo compilation of the mapped walls.

### Figure 5: Field Observations

**Image (a)** Notebook sketch from the 920rL drive left hand wall showing a vertical joint and the offset of a quartz vein (grey) observed across it. The dip and direction of movement for the joint are also displayed.

**Image (b)** Notebook sketch from the 920rL showing the shallowly north-east dipping fault dipping at 15/050 and the offset of a quartz vein (grey) observed across it. The dip and direction of movement for the joint are also displayed.

**Image (c)** Notebook sketch from the 920rL escape way cutty showing a linking structure where a series of small fractures link into two main joints in a similar manner to a C-S plane. The dip and direction of movement for the joint are also displayed.

**Image (d)** Notebook sketch from the 920rL escape way cutty showing a linking structure where a series of small fractures link into two main joints in a similar manner to a C-S plane. The dip and direction of movement for the joint are also displayed.

**Image (e)** Photo of the 900rL access right hand pillar, shows a mafic intrusion and a centrally located, quartz-rich gneissic inclusion which has rotated.

**Image (f)** Photo from the 900rL escape way right hand wall, showing boudinaging of the quartz veining.

**Image (g)** Photo from the 920rL drive left hand wall, showing the brecciation of a quartz vein as it enters the dominant shallowly north-east dipping fault.

#### **Figure 6: goCad® Model**

**Image (a)** Interpreted model constructed over the three mapped levels. Illustrating the role of the collected data and the interpreted features geometry.

**Image (b)** Showing the interpreted model in relation to the mine infrastructure.

**Image (c)** Location of the mapped areas in respect to the mine infrastructure showing the geometry of the mine levels.

**Image (d)** A birds-eye view of the mine levels with the collected map data displayed.

#### **Figure 7: Potential Model Geometry**

**Image (a)** Shows a series of unconnected faults that run parallel to one another but do not link or provide a site of nucleation for other fault splays.

**Image (b)** Shows no dominant fault but does have a complex network of linking features and splays that follow the same trend. Secondary features occur at approximately  $45^\circ$ .

**Image (c)** Shows a fault network that has two dominant faults, which provide the nucleus for all other fault propagation. This example like (b), has a series of splays and linking features.

### Figure 8: Argon Age Plateau Plots

**Image (a)** *Challenger-880-9a* age plateau shows an initial step at approximately 1100 Ma before increasing in age to 1800 Ma with the following step. A plateau-like feature is observed between 1800 and 2100 Ma during which 55% cumulative  $^{39}\text{Ar}$  is released. This produces an age of  $1944 \pm 45$  Ma ( $\pm 2.31\%$ ) with a MSWD of 1.86.

**Image (b)** *Challenger-880-9b* age spectrum has an initial step is at approximately 1400 Ma before increasing to approximately 1450 Ma. From this range the age significantly increases to approximately 1700 Ma before producing a plateau-like region at approximately 1860 Ma about where 47% of the cumulative  $^{39}\text{Ar}$  is released. This sample produces an age of  $1861 \pm 16$  Ma ( $\pm 0.84\%$ ) with a MSWD of 0.40. Following this is a minor decline to approximately 1800 Ma.

**Image (c)** *Challenger-880-8* age plateau shows a gradual increase in the percentage of  $^{39}\text{Ar}$  released with ages varying between approximately 1750 Ma and 1900 Ma with approximately 90% of  $^{39}\text{Ar}$  being discharged in this range. A plateau-like region is reached using 13 of the sampled steps producing an age of  $1851 \pm 14$  Ma (0.77%) with a MSWD of 1.14 and a probability of 0.32.

**Figure 9: Interpretation of Stress and Strain**

**Image (a)** Stylised stress ellipsoid showing the direction of fault movement towards the north-east with the conjugate joint set overlaid, showing that all brittle deformation could have occurred in the same stress conditions.

**Image (b)** Stereo-graphic representation showing a contoured plot of poles to the shallowly north-east dipping fault, with a great circle and associated beta-axis representing the average dip of the shallowly north-east dipping faults. The contoured band represents the undulations in dip across the fault package.

**Image (c)** Stereo-graphic representation of the mineral lineation data from the joint sets observed in the 920rL, 900rL and 880rL plotted and contoured to show the density distribution of data which can be observed to have a high density area at the same locations as the beta-axis shown in image (b).

**Figure 10: Cooling History of the Challenger Deposit**

Figure compiled using data from Tomkins *et al* (2004) and Reid *et al* (2010), in conjunction with the data collected in the course of the project. The blue samples are data from Tomkins *et al* (2004) which has been excluded from the cooling history for reasons outlined in the discussion. The red samples indicate crystallisation ages and consequently are not included at the cooling history. The closure temperatures are used to define the temperature at a specific time. A number of cooling paths cannot be ruled out in the interval 2450 Ma to 1860 Ma including rapid cooling followed by reheating to approximately 350°C at 1860 Ma or rapid cooling at 1860 Ma after a period of prolonged high temperature or monotonic cooling between 2450 Ma and approximately 1860 Ma at a rate of



approximately 1°C/Ma. (The black bars signify biotite grains and shades of grey signify other minerals.)

### **Figure 11: Geological History of Selected Gawler Craton Domains**

Figure compiled from Reid *et al* (2008), Thomas *et al* (2008) and Direen *et al* (2005).

Using further information from Tomkins *et al* (2004), Daly *et al* (1998) and Reid *et al* (2010) in conjunction with the data collected during the project (blue).

This figure shows parallels with the between the Christie domain and the Southern Gawler Craton (Spencer and Cleve) and features unique each domain. The differences between the Christie domain and the surrounding domains (Nawa and Fowler) are also indicated.

## **TABLE CAPTIONS**


### **Table 1: Joint Characteristics**

Showing Characteristic features of the three main joint sets observed. The shallowly north-east dipping fault and vertical set 1 were the dominant sets with vertical set 2 only being observed in situations where the mine infrastructure was suited.

## APPENDICES

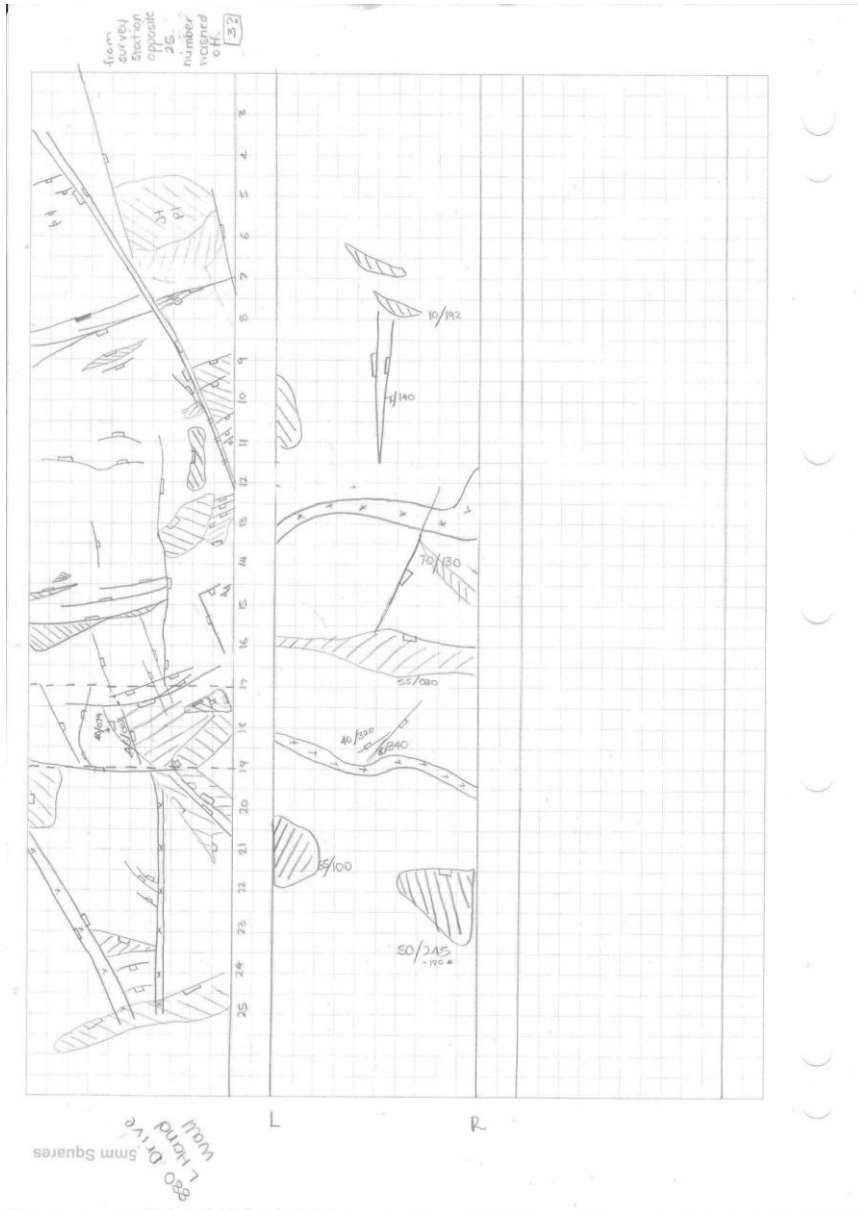
### Appendix 1: goCad® Legend

Line colour	Meaning
Pale Green	Mafic
Magenta	Horizontal joint (shallowly dipping)
Red	Vertical Joint
Black	Lamprophyre within a joint plane
Navy Blue	Conjugate vertical joint (i.e. opposite dip to red)
Purple	Sub-vertical joint
Yellow	Interpretation made to produce a surface
Grey	Gneissic intrusion in the Mafic
Rose Pink	Fracture set or a group of related joints

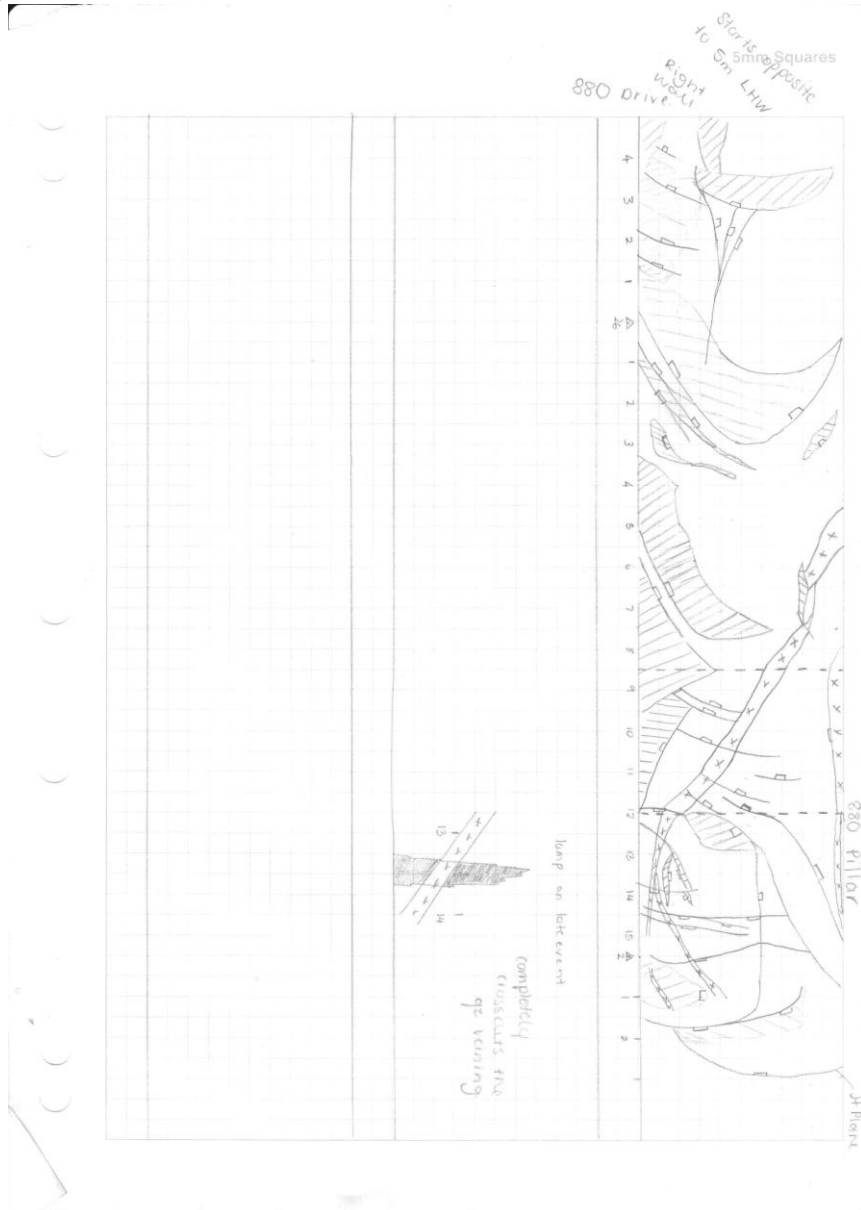
Symbol	Image	Meaning
Dip indicator		This disc displays the orientation of the dip and dip direction of a joint plane.
900_JT_RHW_HL1		The first segment refers to the level, with the second referring to the feature observed, the third refers to the location and the last refers to the joint type and place within the wall.
JT M LM VT HL RHW LHW ACC EW VR		Joint Mafic Lamprophyre Vertical Horizontal Right Hand Wall Left Hand Wall Access Escape way Vent Return



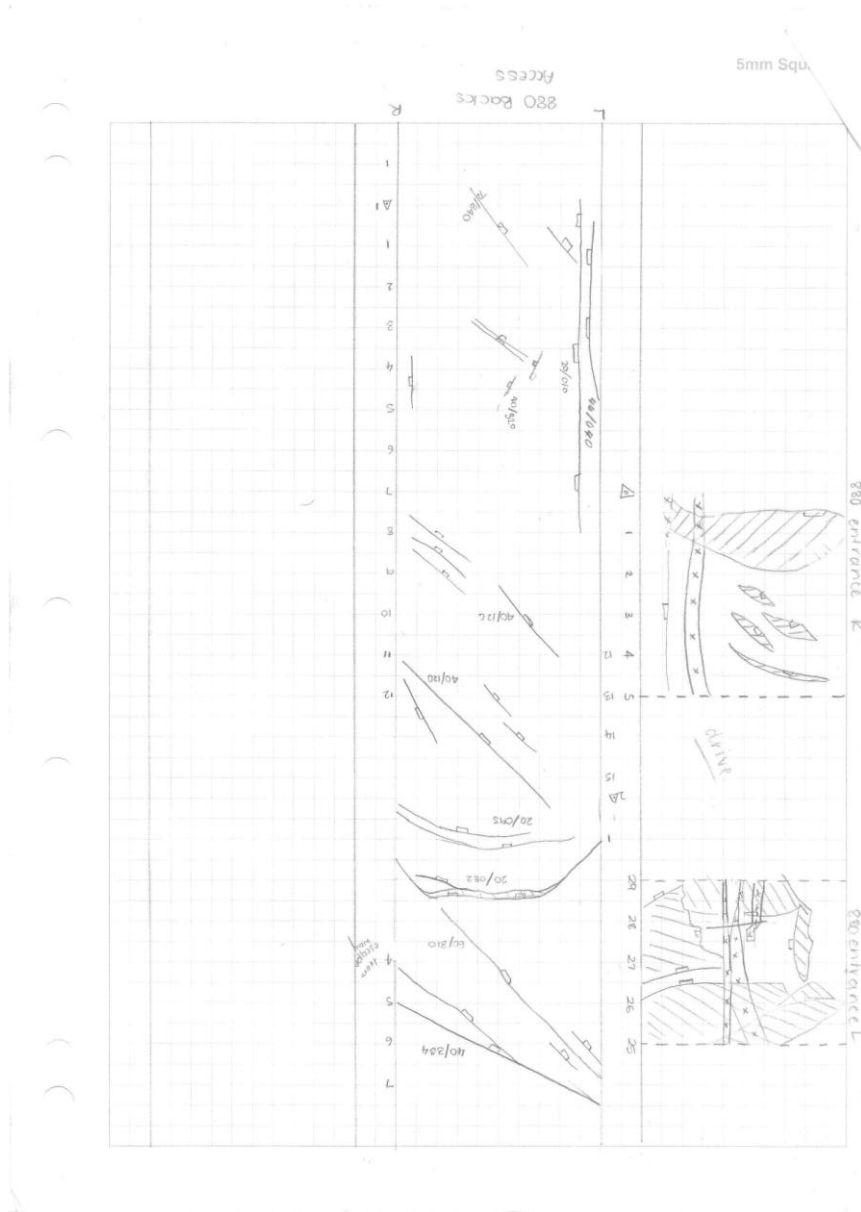
880 Drive Left Hand Wall



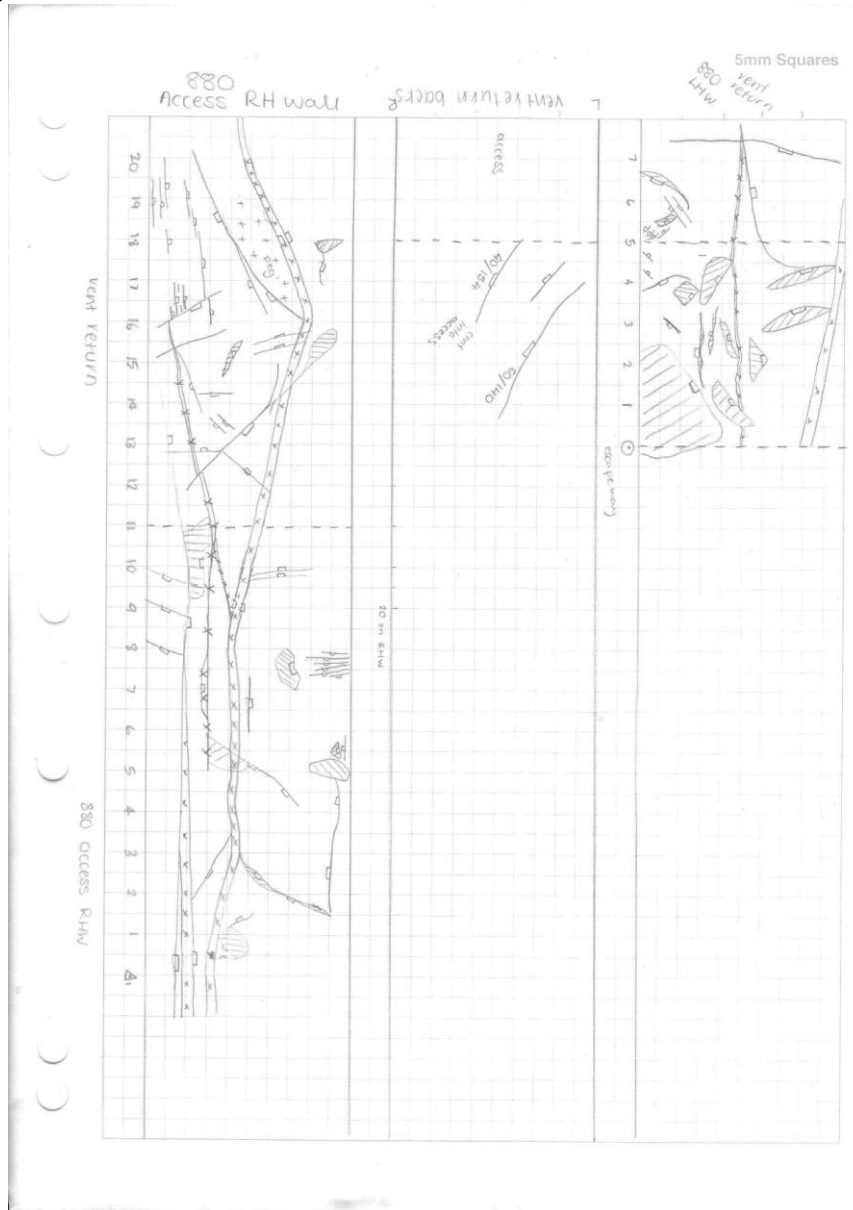
880 Drive Right Wall



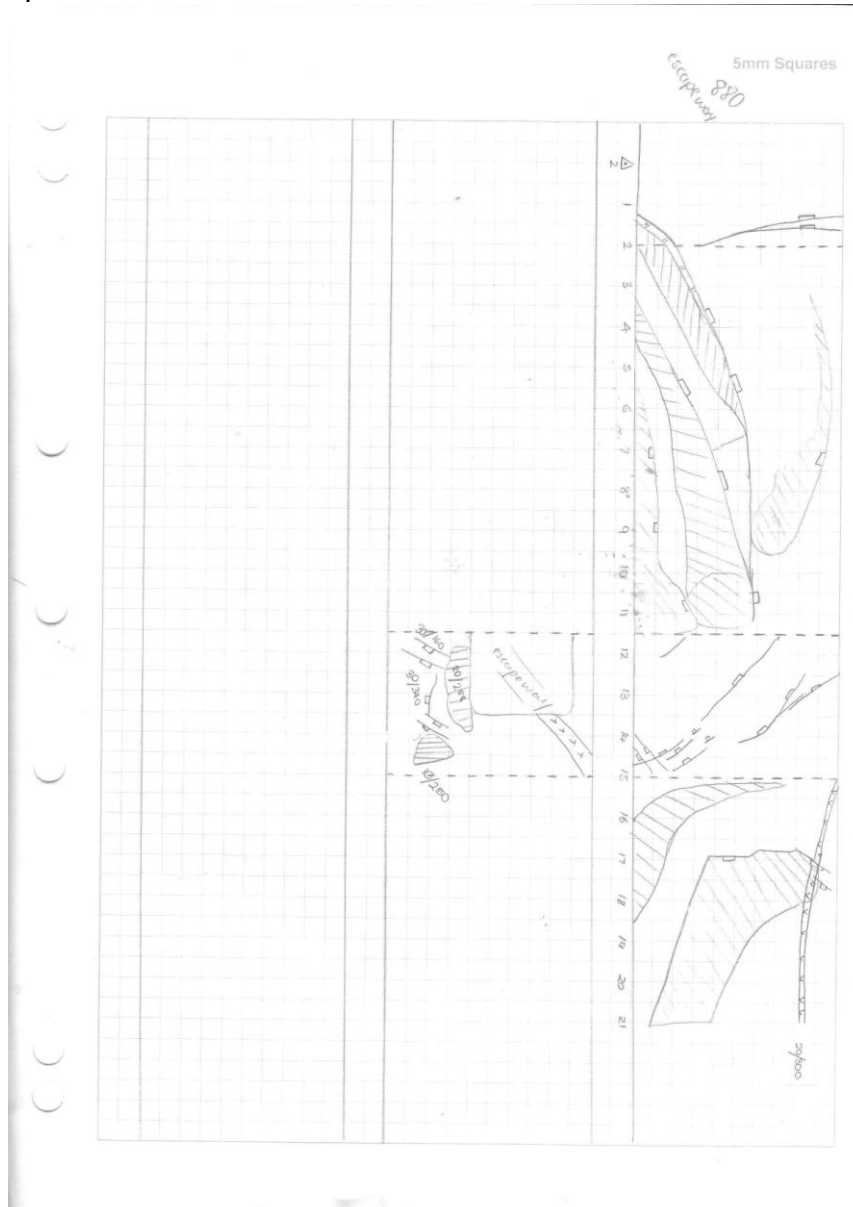
880 Entrance and Backs



80 Access Right Hand Wall and Vent Return

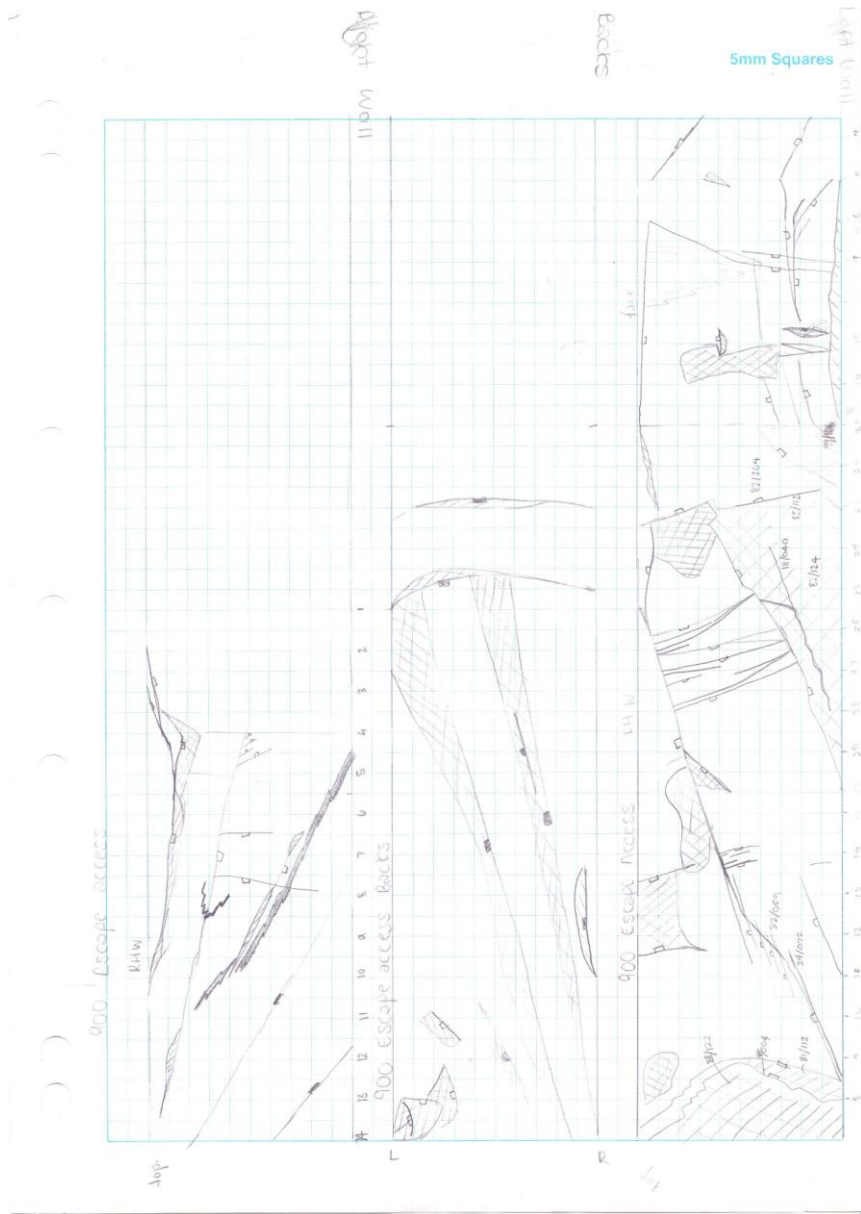


880 Escape way

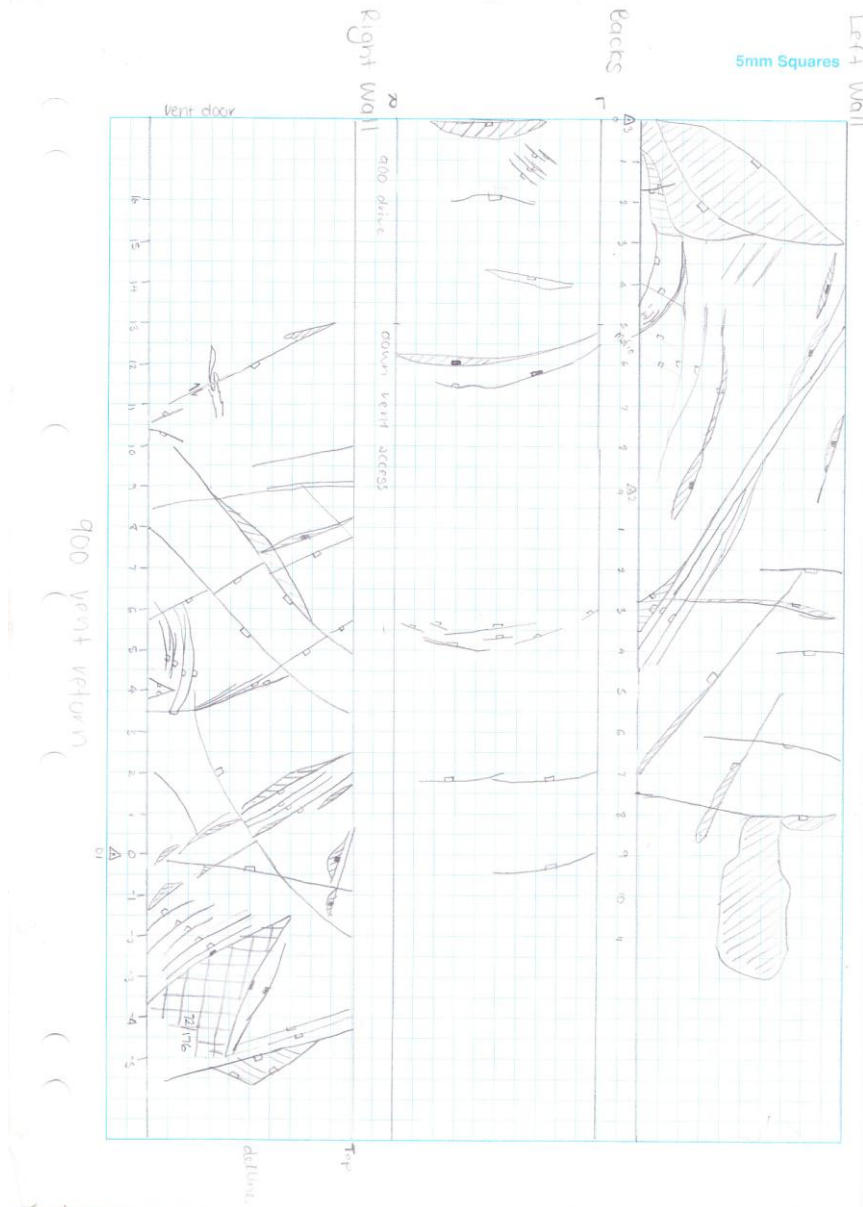




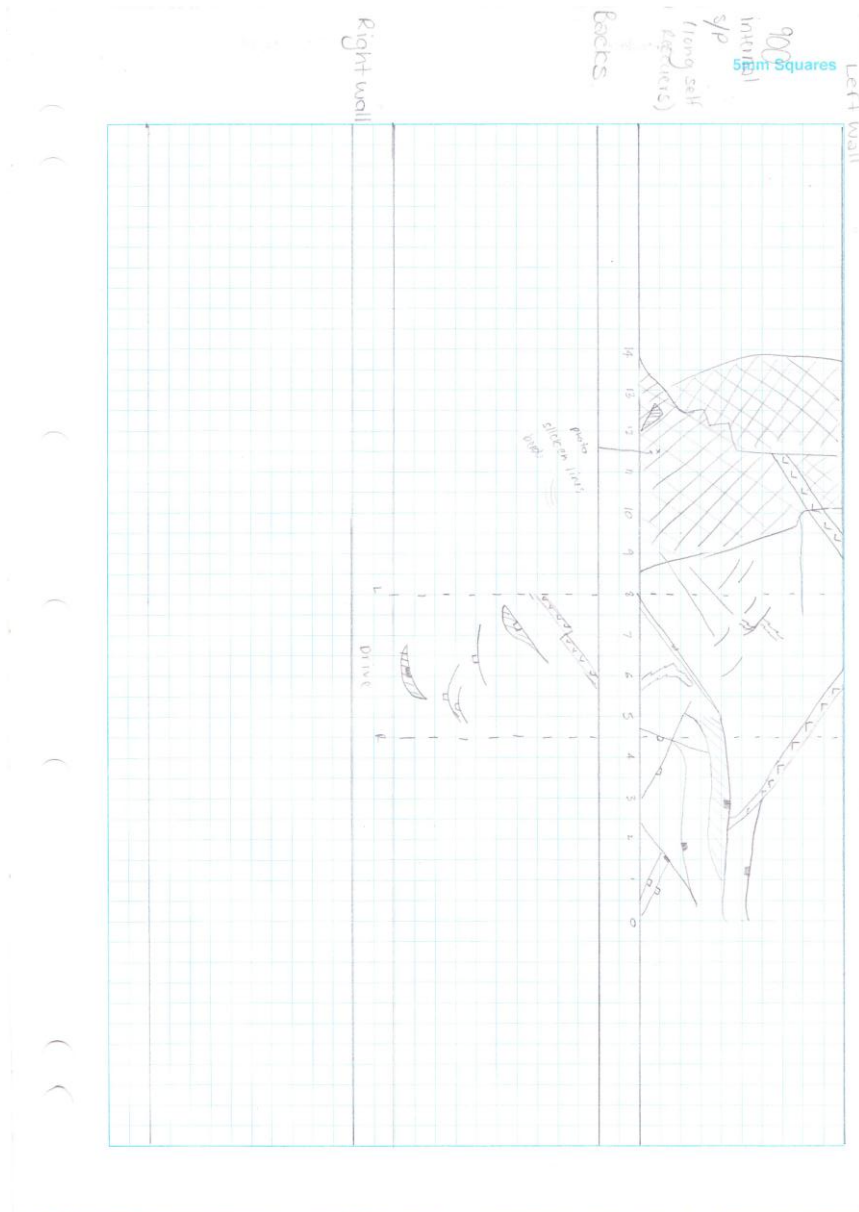
Maps from the 900rL  
Escape way



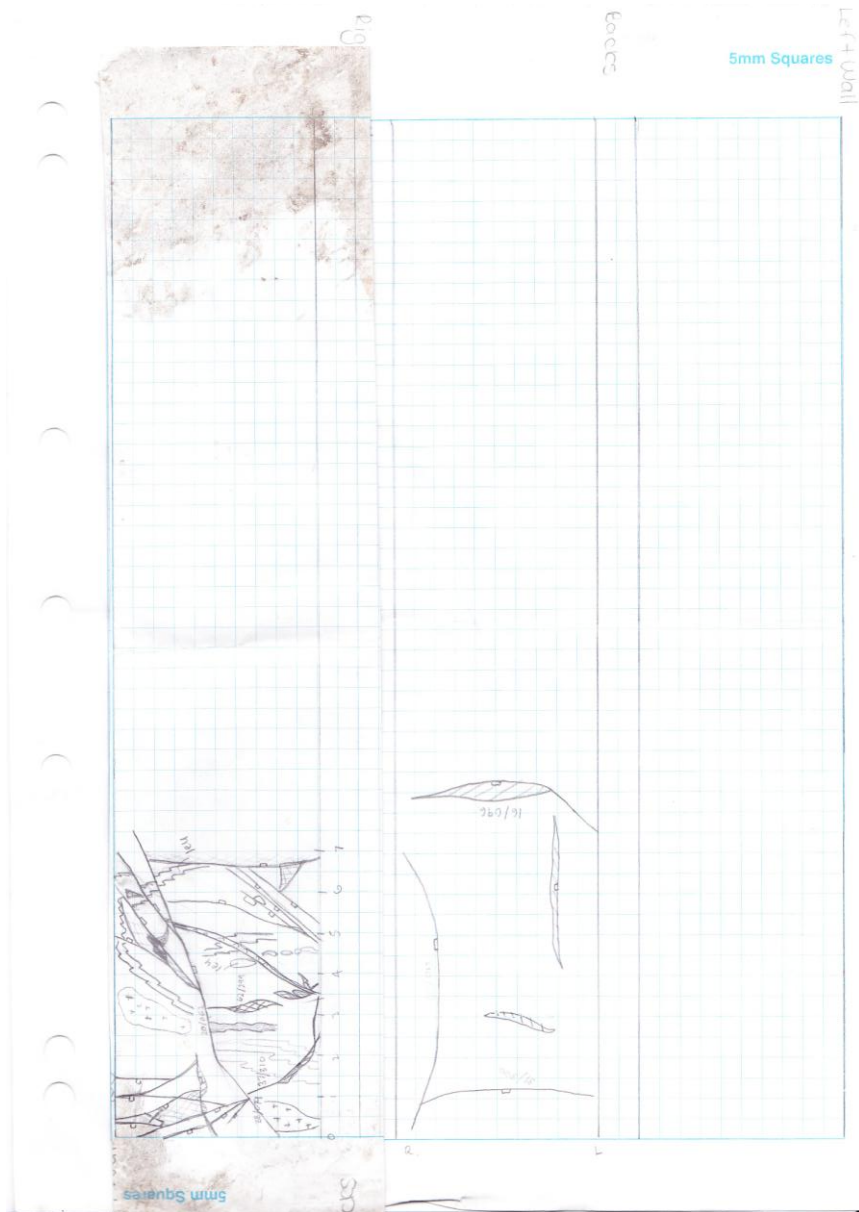
Vent Return



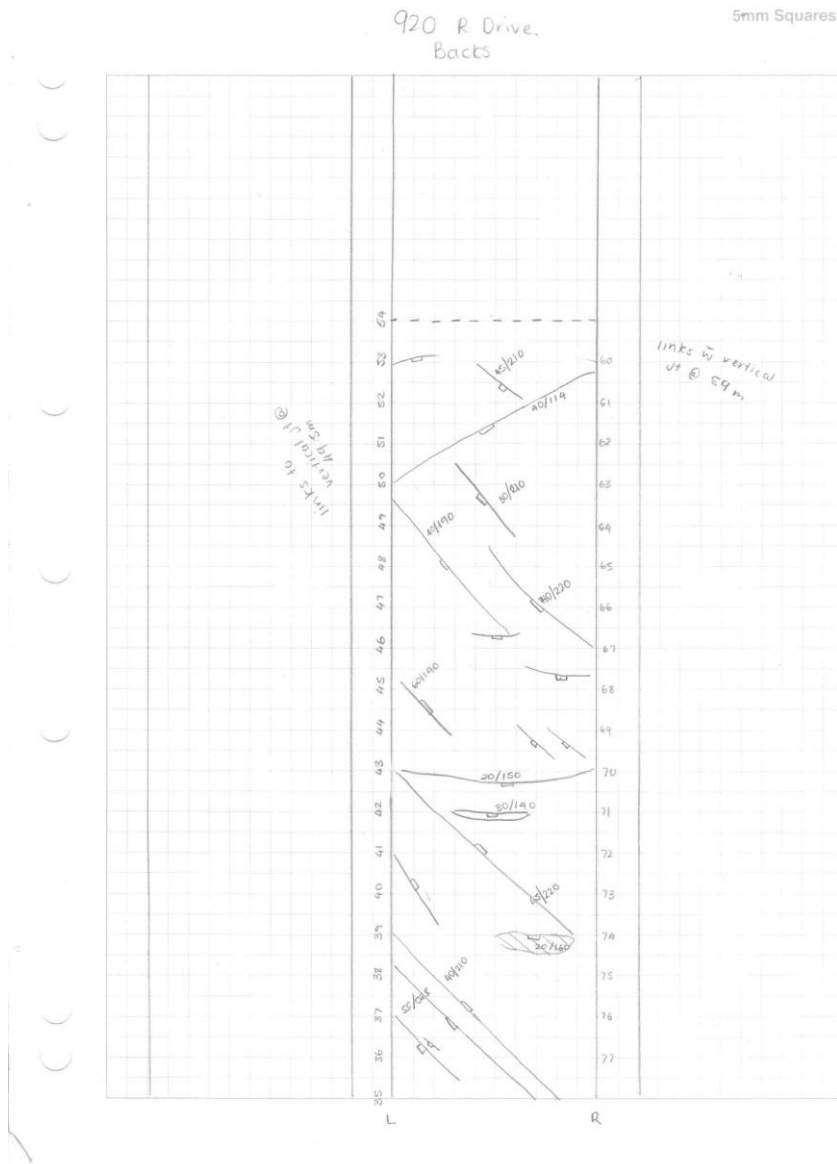
Internal Stock Pile



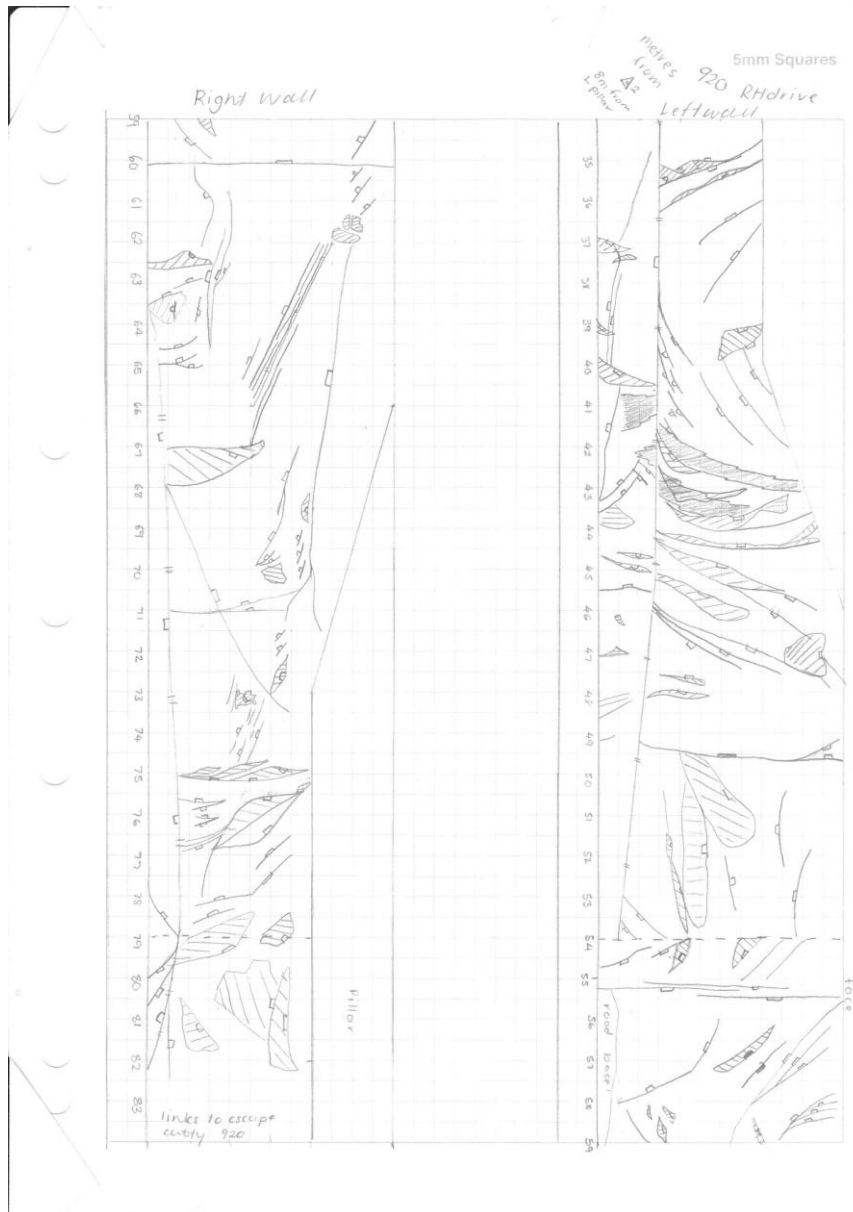
Access Right Hand Pillar



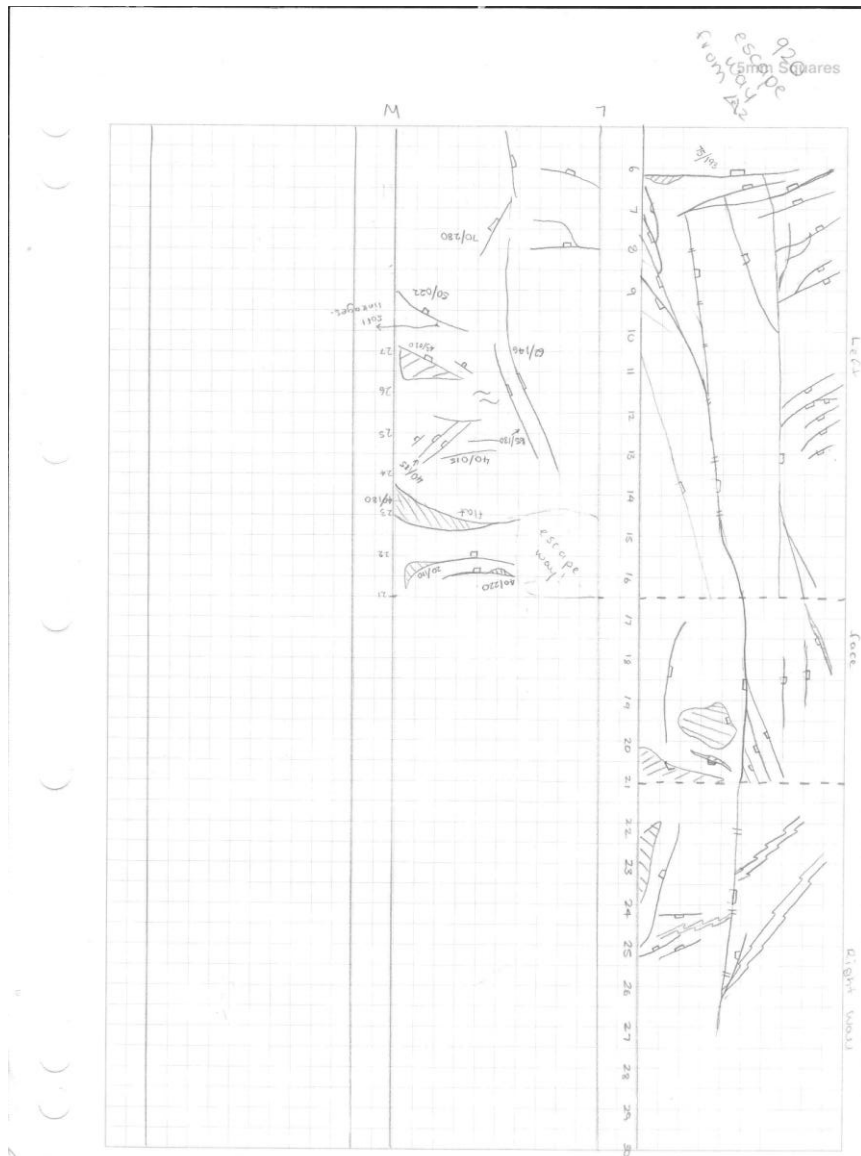
Maps from the 920rL  
Right Hand Drive Backs



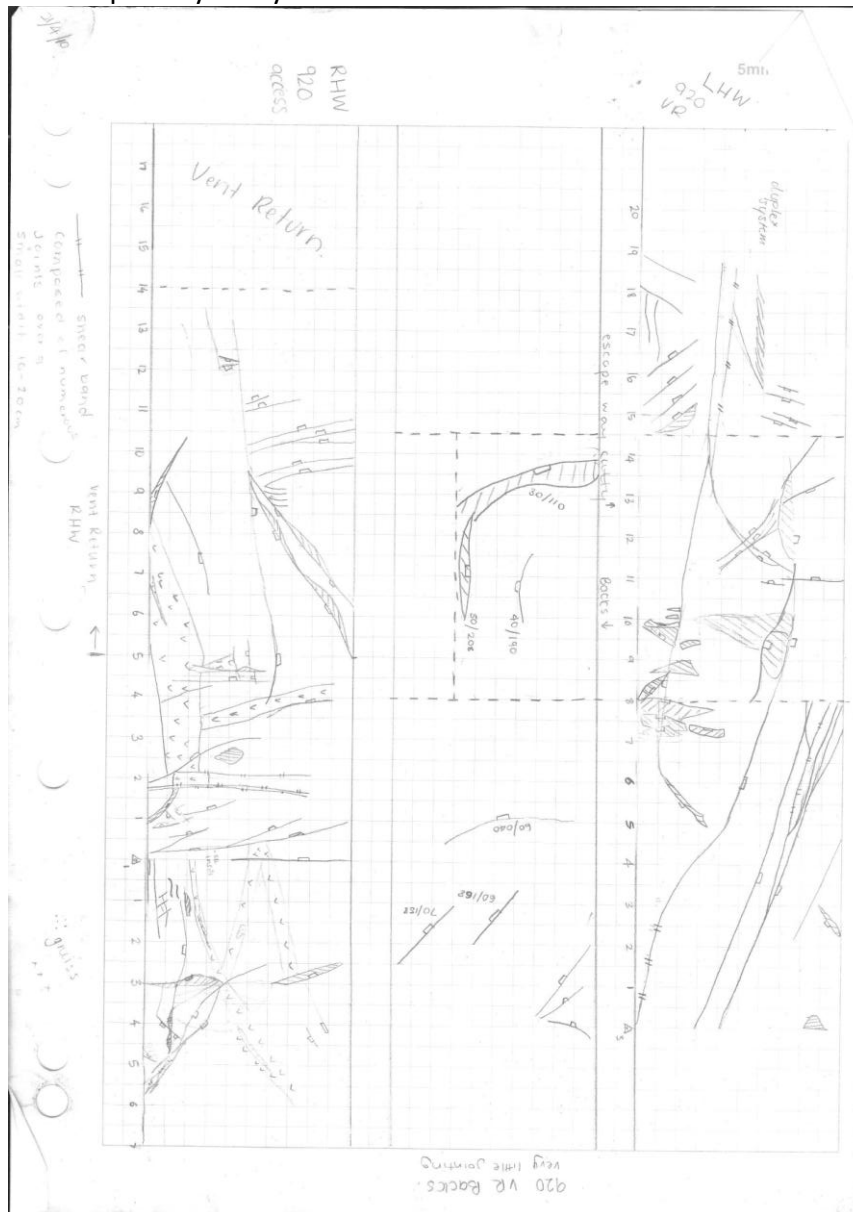
Right Hand Drive



Escape way

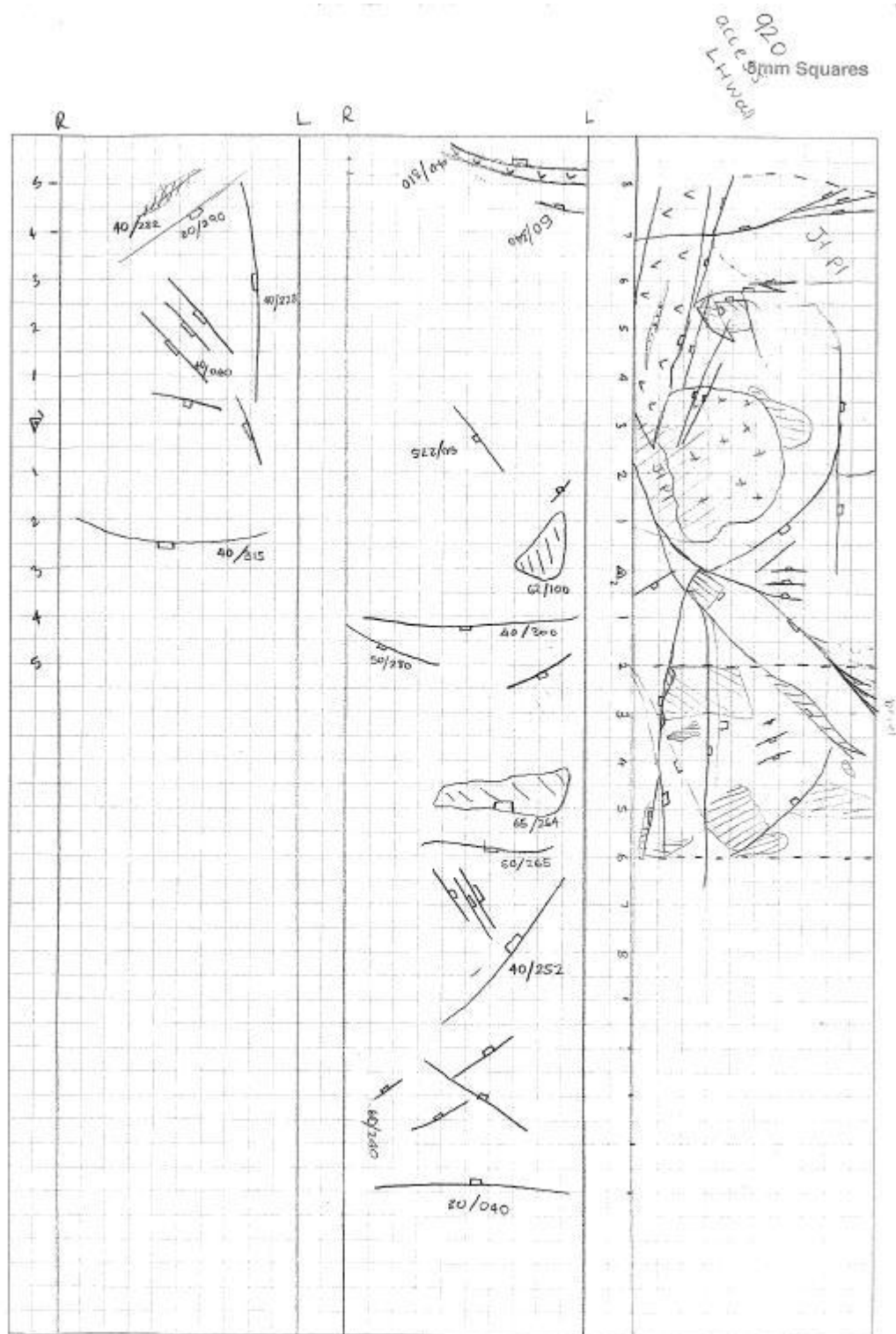


Vent Return and Escape Way Cutty





920 Access



**Appendix 3: Challenger-880-8 Raw Data**

Incremental Heating		36Ar(a)	37Ar(ca)	38Ar(cl)	39Ar(k)	40Ar(r)	Age ± 2σ (Ma)	40Ar(r) (%)	39Ar(k) (%)	K/Ca	± 2σ
0A12589D	62.00 W	0.000080	0.000146	0.000000	0.004612	0.540293	1370.39 ± 31.52	95.75	4.42	13.574	± 12.305
0A12590D	62.50 W	0.000007	0.000001	0.000000	0.001657	0.300882	1835.41 ± 70.44	99.28	1.59	1412.765	± 325623.596
0A12591D	63.00 W	0.000024	0.000041	0.000000	0.002615	0.455793	1788.14 ± 40.73	98.43	2.51	27.206	± 79.655
0A12593D	63.50 W	0.000016	0.000002	0.000003	0.002158	0.381946	1805.87 ± 41.74	98.79	2.07	605.719	± 46393.421
0A12594D	64.00 W	0.000051	0.000039	0.000002	0.003672	0.657904	1819.78 ± 29.72	97.74	3.52	40.008	± 98.808
0A12595D	64.50 W 4	0.000025	0.000045	0.000010	0.003901	0.710064	1838.11 ± 32.32	98.95	3.74	37.381	± 95.451
0A12597D	65.00 W 4	0.000004	0.000007	0.000000	0.003187	0.590091	1857.84 ± 31.92	99.77	3.06	190.049	± 2070.372
0A12650D	66.00 W 4	0.000000	0.000040	0.000000	0.003189	0.603455	1883.28 ± 23.94	100.00	3.06	34.312	± 86.628
0A12651D	66.50 W 4	0.000166	0.003529	0.000017	0.059803	11.017963	1852.10 ± 7.42	99.55	57.36	7.287	± 0.414
0A12652D	66.70 W 4	0.000000	0.000000	0.000000	0.001058	0.189098	1816.84 ± 46.82	100.00	1.01	7.329	± 0.443
0A12654D	67.20 W 4	0.000002	0.000000	0.000000	0.000982	0.182280	1860.76 ± 65.26	99.60	0.94	7.329	± 0.443
0A12655D	68.20 W 4	0.000000	0.000080	0.000014	0.001140	0.208674	1844.27 ± 30.92	100.00	1.09	6.138	± 6.612
0A12656D	70.00 W	0.000092	0.000924	0.000008	0.011475	2.049745	1816.33 ± 11.66	98.68	11.01	5.341	± 0.660
0A12658D	70.50 W 4	0.000041	0.000109	0.000000	0.001984	0.362265	1841.92 ± 41.09	96.76	1.90	7.852	± 10.781
0A12659D	71.50 W 4	0.000104	0.000042	0.000000	0.001854	0.333201	1823.33 ± 43.08	91.44	1.78	18.866	± 42.557
0A12660D	72.20 W 4	0.000040	0.000000	0.000000	0.000534	0.097413	1840.57 ± 100.14	88.99	0.51	30.191	± 98.173
0A12662D	79.20 W 4	0.000026	0.000000	0.000000	0.000167	0.026335	1678.16 ± 357.93	77.43	0.16	30.191	± 98.173
0A12663D	80.50 W 4	0.000033	0.000000	0.000009	0.000193	0.032935	1765.90 ± 272.90	76.92	0.18	30.191	± 98.173
0A12664D	82.00 W 4	0.000056	0.000000	0.000003	0.000077	0.014904	1912.57 ± 732.94	46.94	0.07	30.191	± 98.173
	Σ	0.000770	0.005005	0.000066	0.104258	18.755238					

Information on Analysis	Results	40(r)/39(k) ± 2σ	Age ± 2σ (Ma)	MSWD	39Ar(k) (% <sub>i</sub> ,n)	K/Ca ± 2σ		
1/8/1900	<b>Weighted Plateau (if step 70W excluded)</b>	184.2153 ± 1.0777 ± 0.59%	1852 ± 14 ± 0.77%	1.15	74.88 13	7.314 ± 0.250		
Bio							External Error ± 16	Statistical T Ratio
Laser							Analytical Error ± 7	
FJ								
Project = Challenger_C Rowett	<b>Total Fusion Age</b>	179.8928 ± 0.8810 ± 0.49%	1824.48 ± 13.66 ± 0.75%	1.0720	19	8.958 ± 0.882		
Irradiation = 18t25h							External Error ± 15.01	
J = 0.0095820 ± 0.0000517							Analytical Error ± 5.64	
FCs = 28.305 ± 0.010 Ma								

Normal Isochron		39(k)/36(a) ± 2σ	40(a+r)/36(a) ± 2σ	r.i.
0A12589D	62.00 W	57.4 ± 30.2	7027.7 ± 3691.6	0.9990
0A12590D	62.50 W	226.4 ± 1320.5	41415.1 ± 241542.5	1.0000
0A12591D	63.00 W	107.3 ± 175.8	18999.0 ± 31122.2	0.9999
0A12593D	63.50 W	137.9 ± 174.9	24704.0 ± 31329.7	0.9997
0A12594D	64.00 W	72.2 ± 25.2	13228.0 ± 4613.2	0.9975
0A12595D	64.50 W	4 154.7 ± 135.8	28458.1 ± 24976.5	0.9996
0A12597D	65.00 W	4 713.7 ± 2984.2	132434.7 ± 553761.9	1.0000
0A12650D	66.00 W	4 713.7 ± 0.0	132434.7 ± 0.0	1.0000
0A12651D	66.50 W	4 359.5 ± 60.3	66532.7 ± 11161.0	0.9993
0A12652D	66.70 W	4 363.2 ± 0.0	67427.4 ± 0.0	0.9997
0A12654D	67.20 W	4 403.2 ± 4159.3	75133.0 ± 775097.0	1.0000
0A12655D	68.20 W	4 363.2 ± 0.0	67427.4 ± 0.0	0.9997
0A12656D	70.00 W	124.7 ± 33.2	22580.8 ± 6002.6	0.9994
0A12658D	70.50 W	4 48.8 ± 41.8	9216.4 ± 7878.5	0.9997
0A12659D	71.50 W	4 17.7 ± 4.1	3488.5 ± 796.7	0.9911
0A12660D	72.20 W	4 13.2 ± 7.3	2711.1 ± 1495.3	0.9954
0A12662D	79.20 W	4 6.5 ± 5.8	1323.1 ± 1163.5	0.9747
0A12663D	80.50 W	4 5.8 ± 4.0	1293.6 ± 868.0	0.9811
0A12664D	82.00 W	4 1.4 ± 0.8	562.7 ± 252.0	0.7835

Results	40(a)/36(a) ± 2σ	40(r)/39(k) ± 2σ	Age ± 2σ (Ma)	MSWD
<b>Isochron</b>	209.7635 ± 75.2391 ± 35.87%	185.2925 ± 1.1514 ± 0.62%	1858.74 ± 14.51 ± 0.78% External Error ± 15.83 Analytical Error ± 7.24	0.49

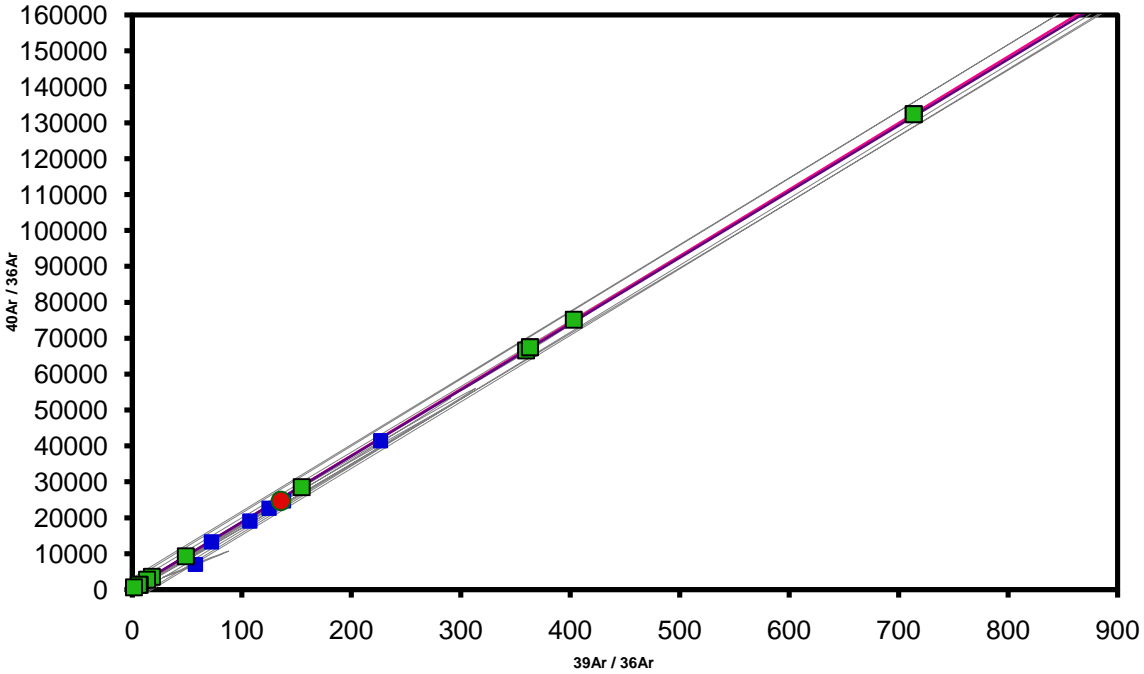
Statistics	Statistical F Ratio Error Magnification n	1.79 1.0000 13	Convergence Number of Iterations Calculated Line	0.0004607815 1 Weighted York-2
------------	---	----------------------	--	--------------------------------------

Inverse Isochron		39(k)/40(a+r) ± 2σ	36(a)/40(a+r) ± 2σ	r.i.
0A12589D	62.00 W	0.008173 ± 0.000188	0.000142 ± 0.000075	0.0005
0A12590D	62.50 W	0.005467 ± 0.000239	0.000024 ± 0.000141	0.0000
0A12591D	63.00 W	0.005648 ± 0.000138	0.000053 ± 0.000086	0.0001
0A12593D	63.50 W	0.005581 ± 0.000184	0.000040 ± 0.000051	0.0002
0A12594D	64.00 W	0.005456 ± 0.000134	0.000076 ± 0.000026	0.0002
0A12595D	64.50 W	4 0.005436 ± 0.000143	0.000035 ± 0.000031	0.0004
0A12597D	65.00 W	4 0.005389 ± 0.000139	0.000008 ± 0.000032	0.0000
0A12650D	66.00 W	4 0.005285 ± 0.000108	0.000000 ± 0.000000	0.0000
0A12651D	66.50 W	4 0.005403 ± 0.000034	0.000015 ± 0.000003	0.0144
0A12652D	66.70 W	4 0.005596 ± 0.000228	0.000000 ± 0.000000	0.0002
0A12654D	67.20 W	4 0.005366 ± 0.000204	0.000013 ± 0.000137	0.0001
0A12655D	68.20 W	4 0.005464 ± 0.000146	0.000000 ± 0.000000	0.0002
0A12656D	70.00 W	0.005524 ± 0.000052	0.000044 ± 0.000012	0.0005
0A12658D	70.50 W	4 0.005298 ± 0.000111	0.000109 ± 0.000093	0.0003
0A12659D	71.50 W	4 0.005088 ± 0.000156	0.000287 ± 0.000065	0.0014
0A12660D	72.20 W	4 0.004878 ± 0.000258	0.000369 ± 0.000203	0.0020
0A12662D	79.20 W	4 0.004902 ± 0.000987	0.000756 ± 0.000665	0.0032
0A12663D	80.50 W	4 0.004501 ± 0.000596	0.000773 ± 0.000519	0.0042
0A12664D	82.00 W	4 0.002420 ± 0.000857	0.001777 ± 0.000796	0.0041

Results	40(a)/36(a) ± 2σ	40(r)/39(k) ± 2σ	Age ± 2σ (Ma)	MSWD
<b>Isochron</b>	249.7682 ± 75.1822 ± 30.10%	184.2672 ± 1.1489 ± 0.62%	1852.29 ± 14.50 ± 0.78% External Error ± 15.81 Analytical Error ± 7.25	0.24
<b>Statistics</b>	Statistical F Ratio	1.79	Convergence	0.0000036807
	Error Magnification	1.0000	Number of Iterations	5
	n	13	Calculated Line	Weighted York-2

**Appendix 4: Challenger-880-8 Normal and Inverse Isochron**  
 Normal Isochron

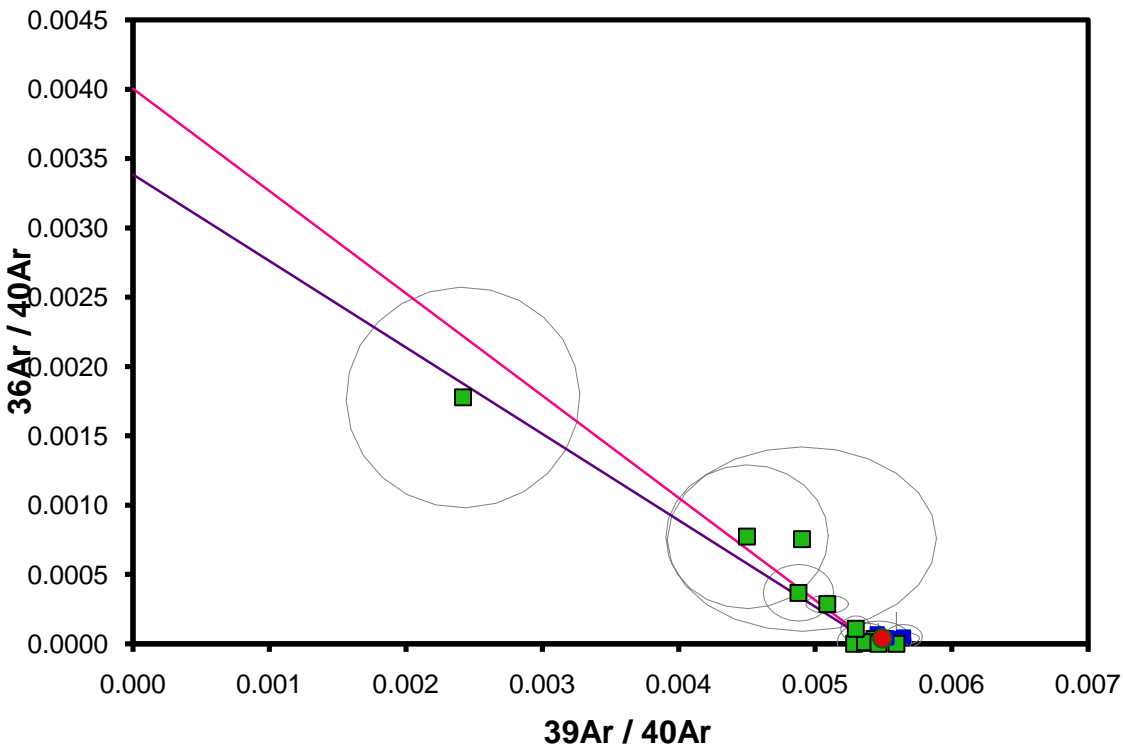
**8.AGE >>> 7/01/1900 >>> CHALLENGER\_C ROWETT PROJECT**



**Sample Info**  
 IRR = 18t25h  
 J = 0.0095820 ± 0.0000517

Inverse Isochron

**8.AGE >>> 7/01/1900 >>> CHALLENGER\_C ROWETT PROJECT**



**Sample Info**  
 IRR = 18t25h  
 J = 0.0095820 ± 0.0000517

**Appendix 5: Challenger-880-9a Raw Data**

Incremental Heating		36Ar(a)	37Ar(ca)	38Ar(cl)	39Ar(k)	40Ar(r)	Age ± 2σ (Ma)	40Ar(r) (%)	39Ar(k) (%)	K/Ca ± 2σ
0A12548D	55.50 W	0.000051	0.000182	0.000027	0.003558	0.317942	1126.28 ± 31.97	95.45	18.66	8.400 ± 6.948
0A12549D	55.40 W	0.000021	0.000137	0.000000	0.004819	0.802258	1736.38 ± 22.24	99.21	25.28	15.085 ± 16.568
0A12550D	55.40 W	0.000000	0.000058	0.000000	0.000348	0.066175	1890.17 ± 74.56	100.00	1.82	2.581 ± 6.532
0A12552D	55.60 W	0.000012	0.000192	0.000000	0.005190	0.989603	1892.25 ± 25.50	99.64	27.23	11.634 ± 8.525
0A12554D	55.70 W 4	0.000000	0.000000	0.000000	0.000561	0.114510	1972.39 ± 124.83	100.00	2.95	14.309 ± 10.676
0A12555D	55.90 W 4	0.000007	0.000000	0.000014	0.000304	0.065281	2033.49 ± 232.47	96.84	1.60	3.380 ± 6.650
0A12556D	56.00 W 4	0.000000	0.000086	0.000000	0.002288	0.476652	1998.28 ± 51.28	99.99	12.00	11.440 ± 21.861
0A12557D	56.10 W 4	0.000000	0.000000	0.000000	0.000217	0.043381	1950.16 ± 161.09	100.00	1.14	1.356 ± 1.598
0A12559D	56.20 W 4	0.000000	0.000052	0.000003	0.000332	0.064584	1914.41 ± 89.13	100.00	1.74	2.737 ± 7.772
0A12560D	56.60 W 4	0.000000	0.000076	0.000000	0.001446	0.276289	1894.92 ± 51.41	100.00	7.58	8.233 ± 16.592
Σ		0.000091	0.000783	0.000045	0.019063	3.216676				
Information on Analysis		Results			40(r)/39(k) ± 2σ	Age ± 2σ (Ma)	MSWD	39Ar(k) (% <sub>n</sub> )	K/Ca ± 2σ	
9A Bio Laser FJ Project = Challenger_C Rowett Irradiation = I8t25h J = 0.0095820 ± 0.0000517 FCs = 28.305 ± 0.037 Ma		<b>Minimum age</b>			199.2014 ± 7.1787 ± 3.60%	1944.14 ± 44.95 ± 2.31%	1.86	27.01 6	1.869 ± 1.830	
		<b>Total Fusion Age</b>			168.7359 ± 2.1048 ± 1.25%	1751.57 ± 18.56 ± 1.06%	1.3650	10	10.469 ± 6.361	
						External Error ± 45.43 Analytical Error ± 43.06	2.57 1.3650	Statistical T Ratio Error Magnification		
						External Error ± 19.49 Analytical Error ± 14.03				

Normal Isochron		39(k)/36(a) ± 2σ	40(a+r)/36(a) ± 2σ	r.i.
0A12548D	55.50 W	70.1 ± 45.5	6558.3 ± 4261.2	0.9994
0A12549D	55.40 W	225.1 ± 344.6	37778.3 ± 57812.1	0.9999
0A12550D	55.40 W	48.8 ± 0.0	9119.7 ± 0.0	0.9999
0A12552D	55.60 W	438.6 ± 1204.8	83933.6 ± 230544.5	1.0000
0A12554D	55.70 W 4	209.2 ± 0.0	39978.5 ± 0.0	0.9998
0A12555D	55.90 W 4	42.6 ± 208.0	9438.5 ± 46047.3	0.9998
0A12556D	56.00 W 4	15469.6 ± 3300297.4	3223583.9 ± 687721349.2	1.0000
0A12557D	56.10 W 4	79045.8 ± 0.0	16450192.2 ± 0.0	1.0000
0A12559D	56.20 W 4	79045.8 ± 0.0	16450192.2 ± 0.0	1.0000
0A12560D	56.60 W 4	79045.8 ± 0.0	16450192.2 ± 0.0	1.0000

Results	40(a)/36(a) ± 2σ	40(r)/39(k) ± 2σ	Age ± 2σ (Ma)	MSWD
<b>Isochron</b>	569.6040 ± 3846.0216 ± 675.21%	208.1112 ± 58.3697 ± 28.05%	1996.82 ± 340.38 ± 17.05% External Error ± 340.45 Analytical Error ± 340.13	0.00

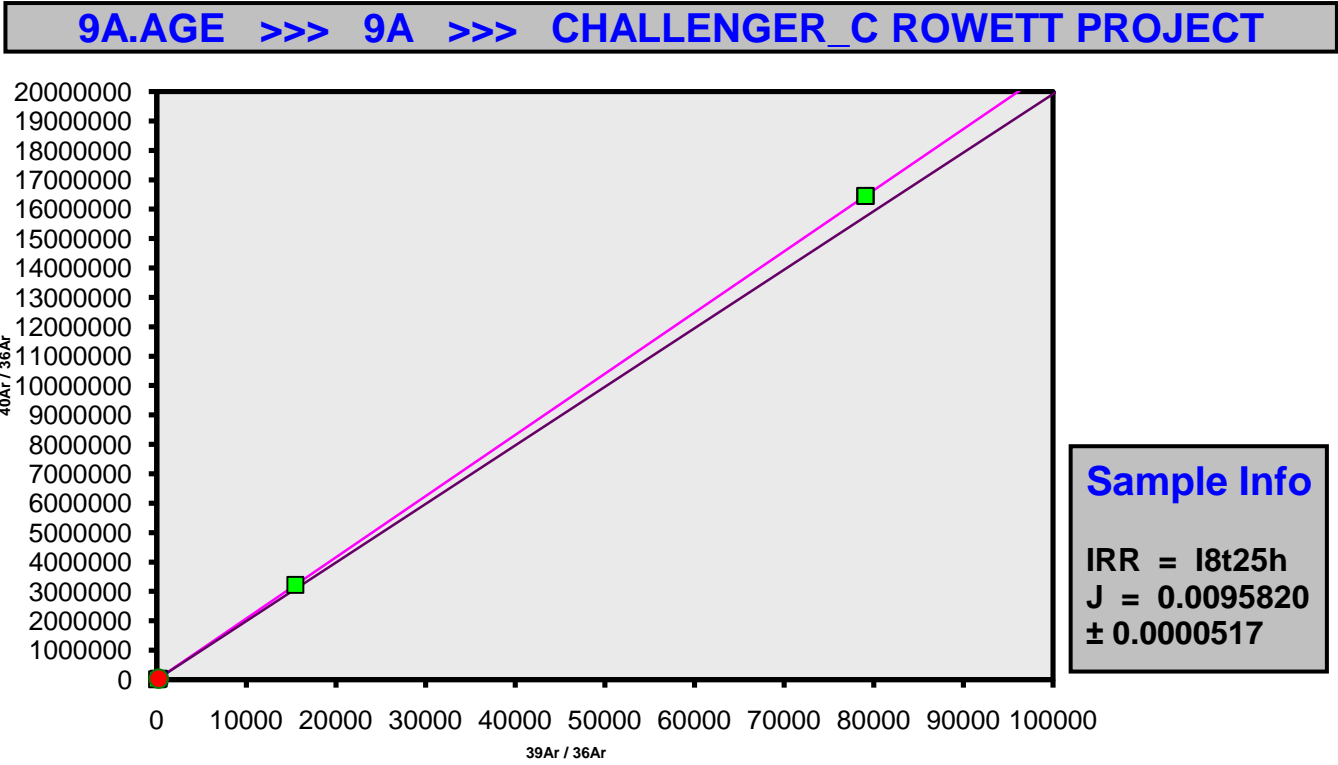
  

Statistics	Statistical F Ratio Error Magnification n	2.37 1.0000 6	Convergence Number of Iterations Calculated Line	0.0000000599 1 Weighted York-2
------------	---	---------------------	--	--------------------------------------

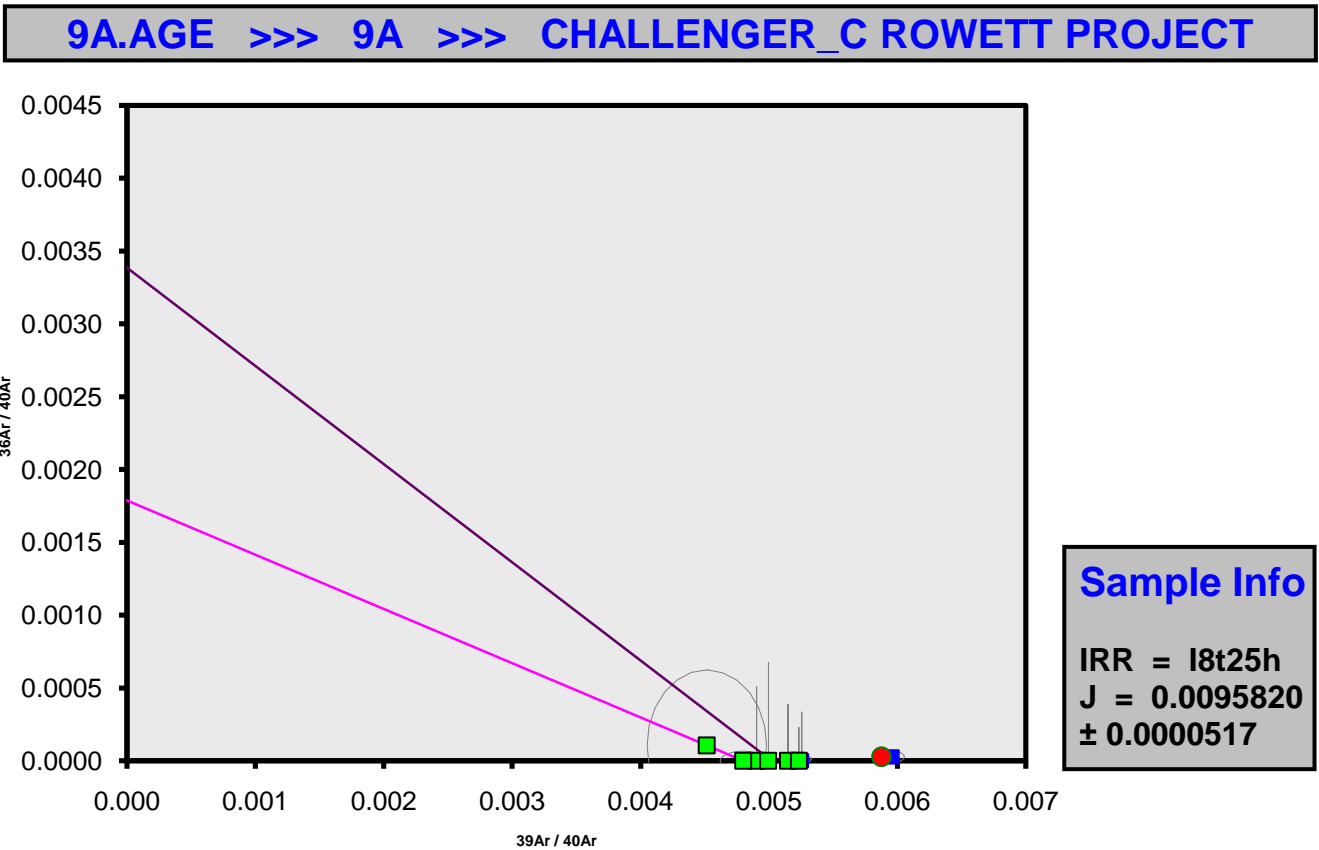
Inverse Isochron		39(k)/40(a+r)	$\pm 2\sigma$	36(a)/40(a+r)	$\pm 2\sigma$	r.i.	
0A12548D	55.50 W	0.010681	$\pm 0.000236$	0.000152	$\pm 0.000099$	0.0005	
0A12549D	55.40 W	0.005960	$\pm 0.000094$	0.000026	$\pm 0.000041$	0.0001	
0A12550D	55.40 W	0.005254	$\pm 0.000333$	0.000000	$\pm 0.000000$	0.0002	
0A12552D	55.60 W	0.005226	$\pm 0.000101$	0.000012	$\pm 0.000033$	0.0000	
0A12554D	55.70 W 4	0.004903	$\pm 0.000508$	0.000000	$\pm 0.000000$	0.0001	
0A12555D	55.90 W 4	0.004515	$\pm 0.000465$	0.000106	$\pm 0.000517$	0.0001	
0A12556D	56.00 W 4	0.004799	$\pm 0.000179$	0.000000	$\pm 0.000066$	0.0000	
0A12557D	56.10 W 4	0.004995	$\pm 0.000672$	0.000000	$\pm 0.000000$	0.0000	
0A12559D	56.20 W 4	0.005147	$\pm 0.000387$	0.000000	$\pm 0.000000$	0.0000	
0A12560D	56.60 W 4	0.005233	$\pm 0.000228$	0.000000	$\pm 0.000000$	0.0000	
Results		40(a)/36(a)	$\pm 2\sigma$	40(r)/39(k)	$\pm 2\sigma$	Age $\pm 2\sigma$ (Ma)	MSWD
Isochron		559.5841	##### $\pm 522.72\%$	208.3455	$\pm 10.9935$ $\pm 5.28\%$	1998.18 $\pm 65.34$ $\pm 3.27\%$ External Error $\pm 65.69$ Analytical Error $\pm 64.01$	0.00
Statistics		Statistical F Ratio Error Magnification n	2.37 1.0000 6	Convergence Number of Iterations Calculated Line		0.0000000015 3 Weighted York-2	



**Appendix 6: Challenger-880-9a Normal and Inverse Isochron**  
 Normal Isochron



Inverse Isochron



**Appendix 7: Challenger-880-9b Raw Data**

Incremental Heating		36Ar(a)	37Ar(ca)	38Ar(cl)	39Ar(k)	40Ar(r)	Age ± 2σ (Ma)	40Ar(r) (%)	39Ar(k) (%)	K/Ca ± 2σ
0A12566D	55.10 W	0.000012	0.000078	0.000000	0.001144	0.141194	1421.24 ± 71.69	97.62	1.64	6.327 ± 8.767
0A12567D	55.40 W	0.000007	0.000124	0.000003	0.001344	0.174566	1472.31 ± 65.54	98.88	1.92	4.646 ± 2.843
0A12569D	70.20 W	0.000175	0.001237	0.000033	0.021861	3.645891	1738.45 ± 16.52	98.59	31.30	7.602 ± 0.659
0A12570D	55.70 W	4 0.000009	0.000003	0.000002	0.000272	0.046037	1753.76 ± 302.33	94.41	0.39	38.005 ± 972.499
0A12572D	55.80 W	4 0.000000	0.000013	0.000011	0.002206	0.409143	1859.69 ± 34.85	100.00	3.16	70.624 ± 534.108
0A12573D	55.90 W	4 0.000018	0.000828	0.000027	0.011231	2.083805	1860.31 ± 12.31	99.75	16.08	5.831 ± 0.741
0A12574D	56.00 W	4 0.000000	0.000173	0.000017	0.005200	0.977114	1875.12 ± 27.94	100.00	7.44	12.957 ± 7.178
0A12575D	56.10 W	4 0.000016	0.001022	0.000022	0.013150	2.436826	1858.82 ± 18.05	99.81	18.83	5.533 ± 0.593
0A12577D	56.20 W	0.000018	0.000683	0.000014	0.008420	1.459905	1782.27 ± 18.57	99.63	12.05	5.305 ± 0.843
0A12578D	56.30 W	0.000000	0.000130	0.000005	0.001567	0.274738	1795.12 ± 40.88	100.00	2.24	5.169 ± 4.714
0A12579D	56.40 W	0.000000	0.000000	0.000000	0.000516	0.096650	1871.30 ± 137.11	100.00	0.74	6.021 ± 6.383
0A12580D	56.40 W	0.000000	0.000139	0.000000	0.001239	0.217629	1797.02 ± 56.86	100.00	1.77	3.835 ± 2.652
0A12582D	56.60 W	0.000000	0.000174	0.000005	0.001701	0.349066	1979.80 ± 37.56	100.00	2.44	4.202 ± 2.493
Σ		0.000254	0.004604	0.000138	0.069852	12.312565				
Information on Analysis		Results		40(r)/39(k) ± 2σ	Age ± 2σ (Ma)	MSWD	39Ar(k) (% <sub>n</sub> )	K/Ca ± 2σ		
9B Bio Laser FJ Project = Challenger_C Rowett Irradiation = I8t25h J = 0.0095820 ± 0.0000517 FCs = 28.305 ± 0.037 Ma		<b>Minimum age</b>		185.7096 ± 1.4675 ± 0.79%	1861.36 ± 15.60 ± 0.84% External Error ± 16.84 Analytical Error ± 9.21	0.40 2.78 1.0000	45.90 5 Statistical T Ratio Error Magnification	5.680 ± 0.495		
		<b>Total Fusion Age</b>		176.2664 ± 1.2063 ± 0.68%	1801.10 ± 14.62 ± 0.81% External Error ± 15.85 Analytical Error ± 7.83		13	6.524 ± 0.511		

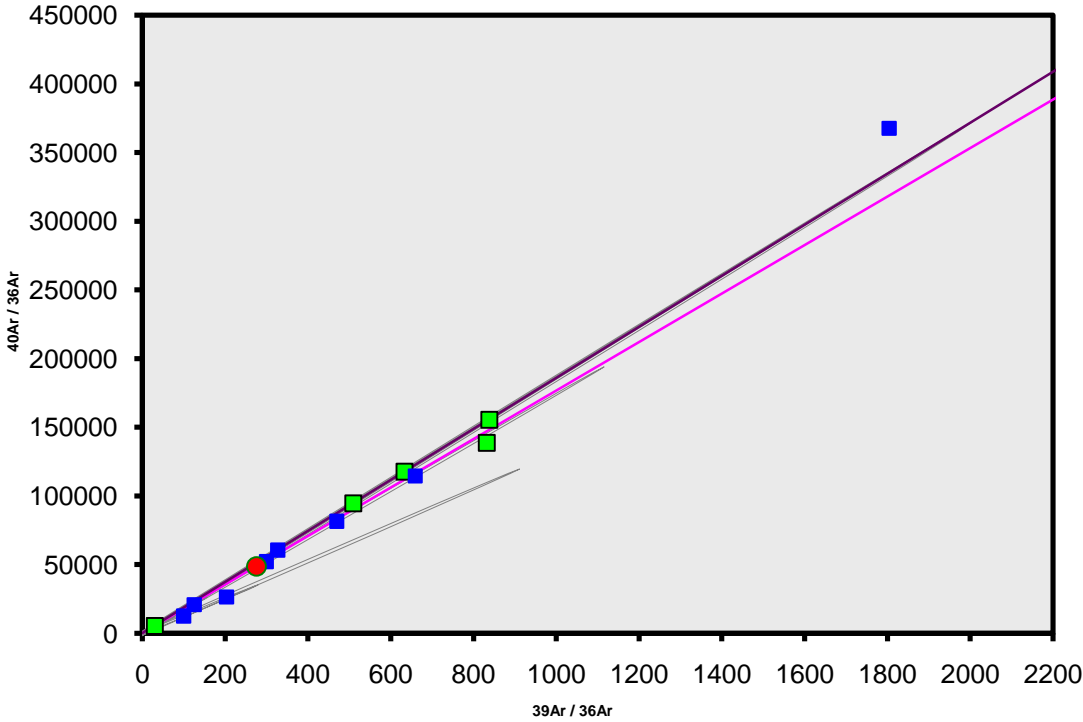
Normal	39(k)/36(a) ± 2σ	40(a+r)/36(a) ± 2σ	r.i.
--------	------------------	--------------------	------

<b>Isochron</b>						
0A12566D	55.10 W		99.4 ± 179.4	12564.7 ± 22674.0		0.9995
0A12567D	55.40 W		203.3 ± 707.2	26711.0 ± 92902.6		0.9999
0A12569D	70.20 W		124.8 ± 30.0	21108.8 ± 5059.7		0.9982
0A12570D	55.70 W	4	29.8 ± 75.1	5343.5 ± 13403.1		0.9960
0A12572D	55.80 W	4	831.8 ± 0.0	138678.2 ± 0.0		1.0000
0A12573D	55.90 W	4	633.1 ± 1042.4	117764.0 ± 193905.6		1.0000
0A12574D	56.00 W	4	508.9 ± 0.0	94639.2 ± 0.0		1.0000
0A12575D	56.10 W	4	837.8 ± 1165.9	155540.9 ± 216456.8		0.9999
0A12577D	56.20 W		468.7 ± 645.5	81569.5 ± 112320.9		0.9999
0A12578D	56.30 W		658.3 ± 0.0	114751.5 ± 0.0		1.0000
0A12579D	56.40 W		327.0 ± 0.0	60644.1 ± 0.0		0.9999
0A12580D	56.40 W		298.7 ± 0.0	52258.6 ± 0.0		1.0000
0A12582D	56.60 W		1804.0 ± 0.0	367709.5 ± 0.0		1.0000
<b>Results</b>			40(a)/36(a) ± 2σ	40(r)/39(k) ± 2σ	Age ± 2σ (Ma)	MSWD
<b>Isochron</b>			248.7450 ± 1340.2257 ± 538.79%	176.4697 ± 11.1069 ± 6.29%	1802.42 ± 73.07 ± 4.05% External Error ± 73.32 Analytical Error ± 72.01	1.09
<b>Statistics</b>			Statistical F Ratio Error Magnification n	2.60 1.0448 5	Convergence Number of Iterations Calculated Line	0.0006555389 1 Weighted York-2

Inverse Isochron		39(k)/40(a+r)	$\pm 2\sigma$	36(a)/40(a+r)	$\pm 2\sigma$	r.i.	
0A12566D	55.10 W	0.007909	$\pm 0.000458$	0.000080	$\pm 0.000144$	0.0002	
0A12567D	55.40 W	0.007612	$\pm 0.000393$	0.000037	$\pm 0.000130$	0.0002	
0A12569D	70.20 W	0.005911	$\pm 0.000085$	0.000047	$\pm 0.000011$	0.0006	
0A12570D	55.70 W	4	$\pm 0.005584$	0.000187	$\pm 0.000469$	0.0001	
0A12572D	55.80 W	4	$\pm 0.005392$	0.000000	$\pm 0.000000$	0.0000	
0A12573D	55.90 W	4	$\pm 0.005376$	0.000008	$\pm 0.000014$	0.0001	
0A12574D	56.00 W	4	$\pm 0.005322$	0.000000	$\pm 0.000000$	0.0001	
0A12575D	56.10 W	4	$\pm 0.005386$	0.000006	$\pm 0.000009$	0.0001	
0A12577D	56.20 W		$\pm 0.005747$	0.000012	$\pm 0.000017$	0.0002	
0A12578D	56.30 W		$\pm 0.005703$	0.000000	$\pm 0.000000$	0.0002	
0A12579D	56.40 W		$\pm 0.005339$	0.000000	$\pm 0.000000$	0.0000	
0A12580D	56.40 W		$\pm 0.005694$	0.000000	$\pm 0.000000$	0.0000	
0A12582D	56.60 W		$\pm 0.004873$	0.000000	$\pm 0.000000$	0.0000	
Results		40(a)/36(a)	$\pm 2\sigma$	40(r)/39(k)	$\pm 2\sigma$	Age $\pm 2\sigma$ (Ma)	MSWD
Isochron		191.2958	$\pm 1037.3949$ $\pm 542.30\%$	186.1875	$\pm 2.5957$ $\pm 1.39\%$	1864.36 $\pm 20.58$ External Error $\pm 1.10\%$ Analytical Error $\pm 21.53$ $\pm 16.27$	0.02
Statistics		Statistical F Ratio Error Magnification n	2.60 1.0000 5	Convergence Number of Iterations Calculated Line		0.0000002845 4 Weighted York-2	

**Appendix 8: Challenger-880-9b Normal and Inverse Isochron**  
 Normal Isochron

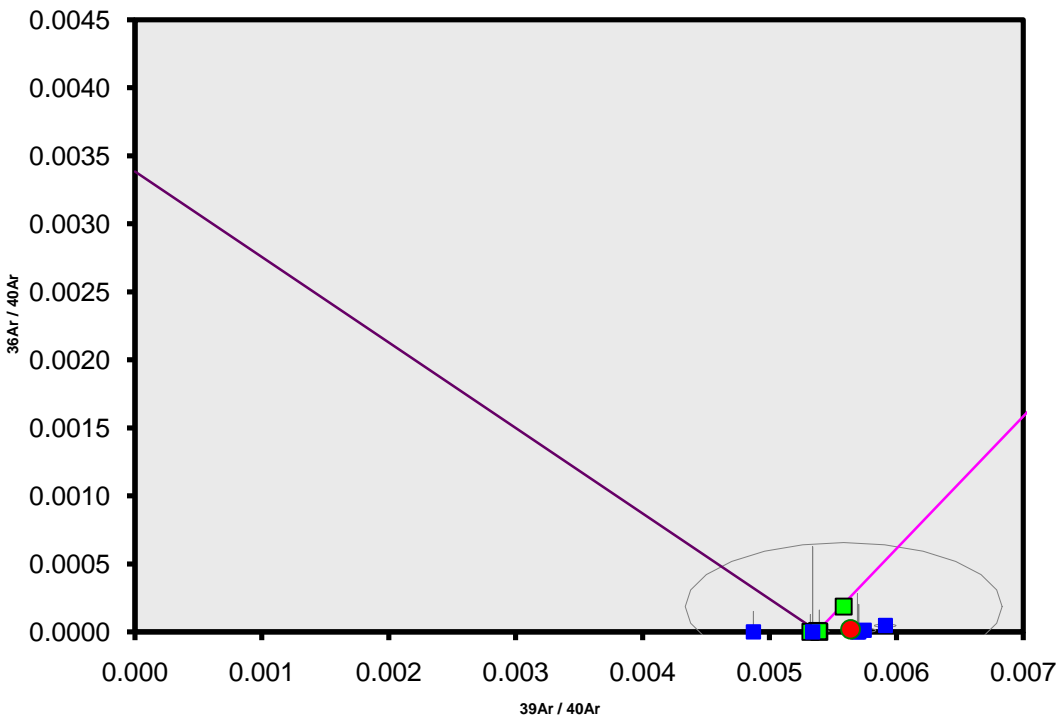
**9B.AGE >>> 9B >>> CHALLENGER\_C ROWETT PROJECT**



**Sample Info**  
 IRR = 18t25h  
 J = 0.0095820  
 $\pm 0.0000517$

Inverse Isochron

**9B.AGE >>> 9B >>> CHALLENGER\_C ROWETT PROJECT**

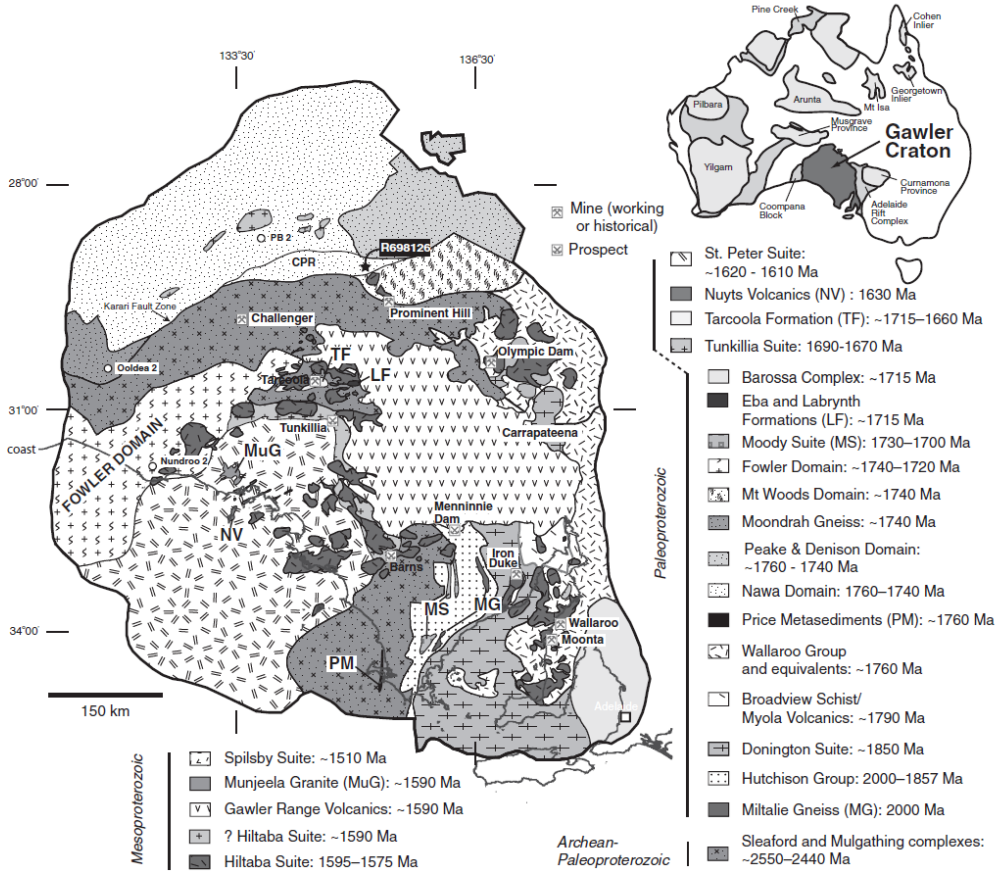


**Sample Info**  
 IRR = 18t25h  
 J = 0.0095820  
 $\pm 0.0000517$

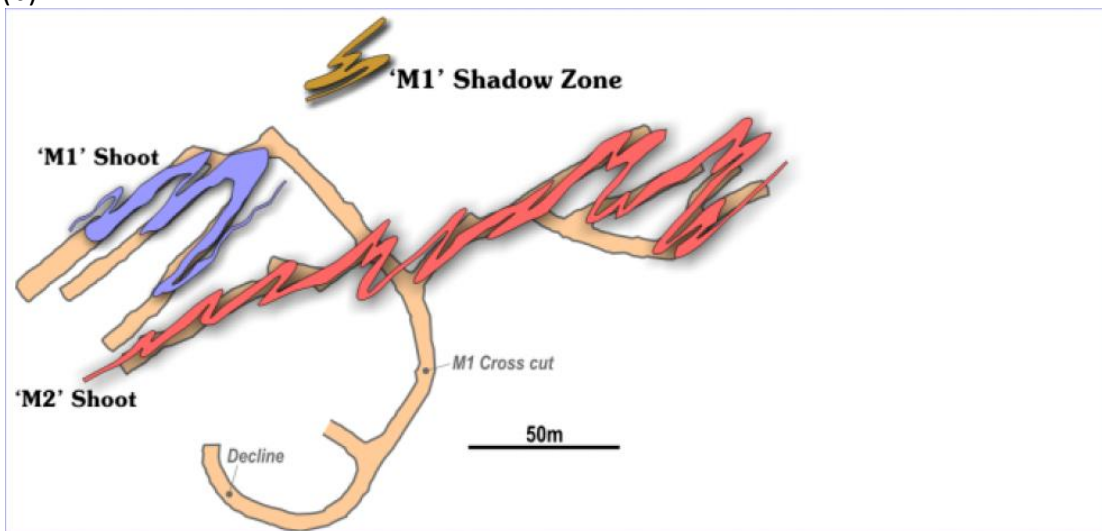
FIGURES

Figure 1: Background

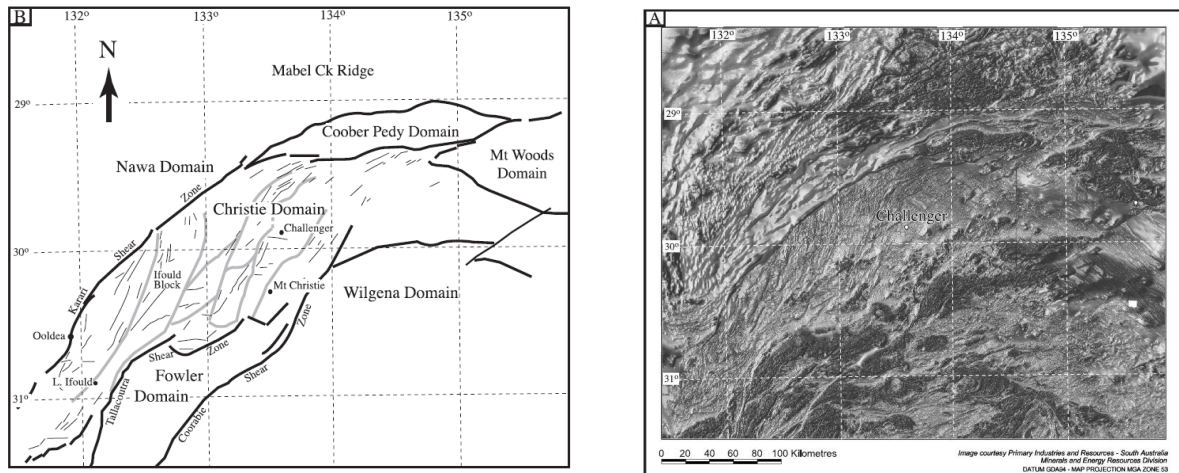
(a)



(b)



(c)



(d)

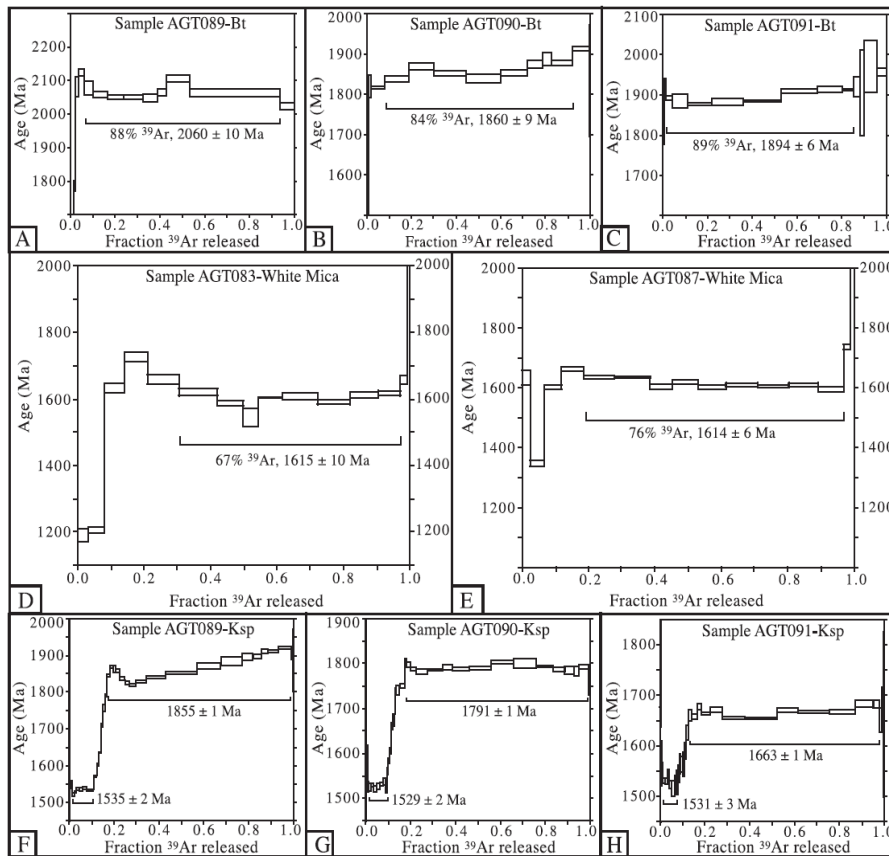


Figure 2: Stereo-graphic Representations of Structural Data

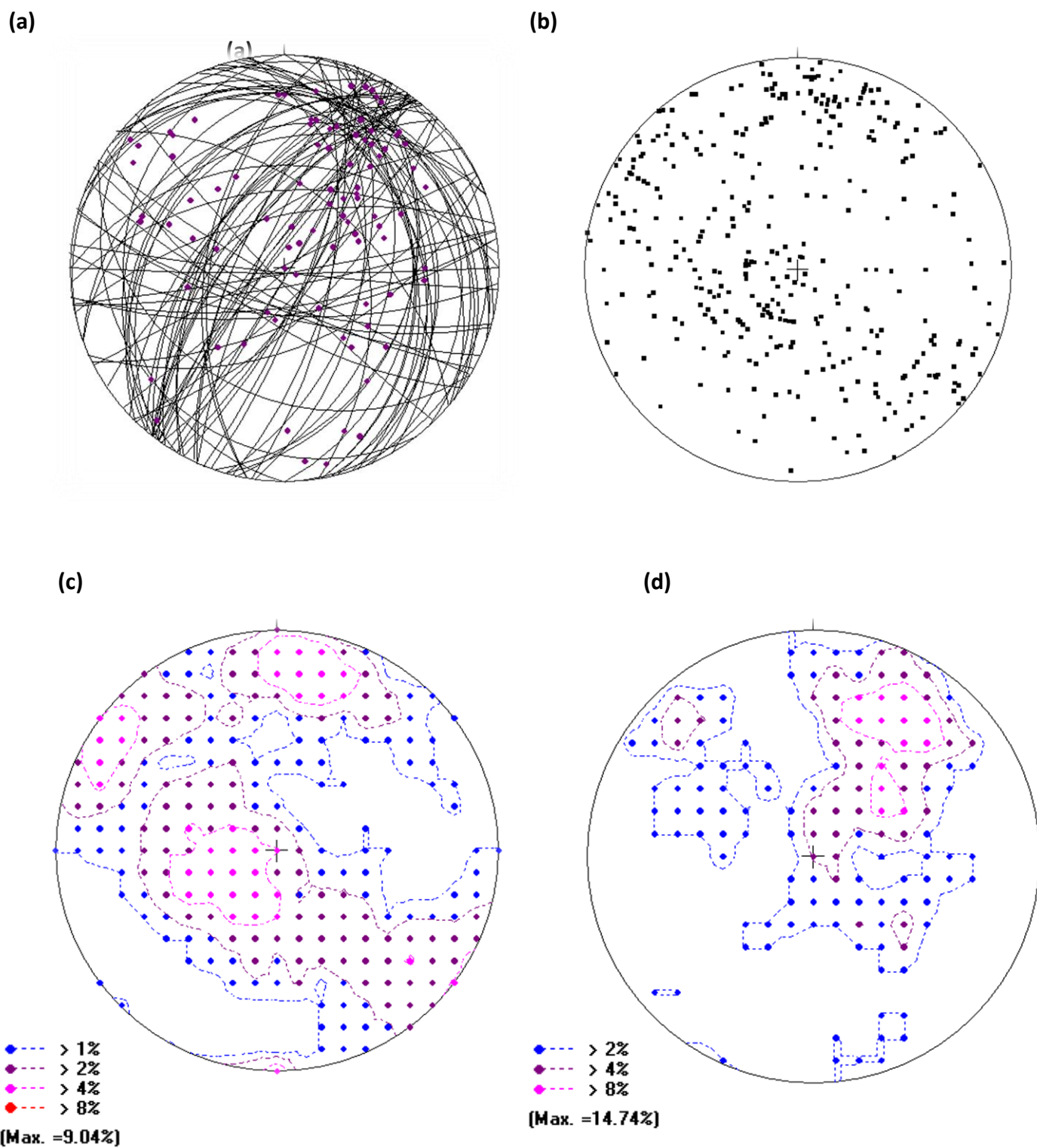
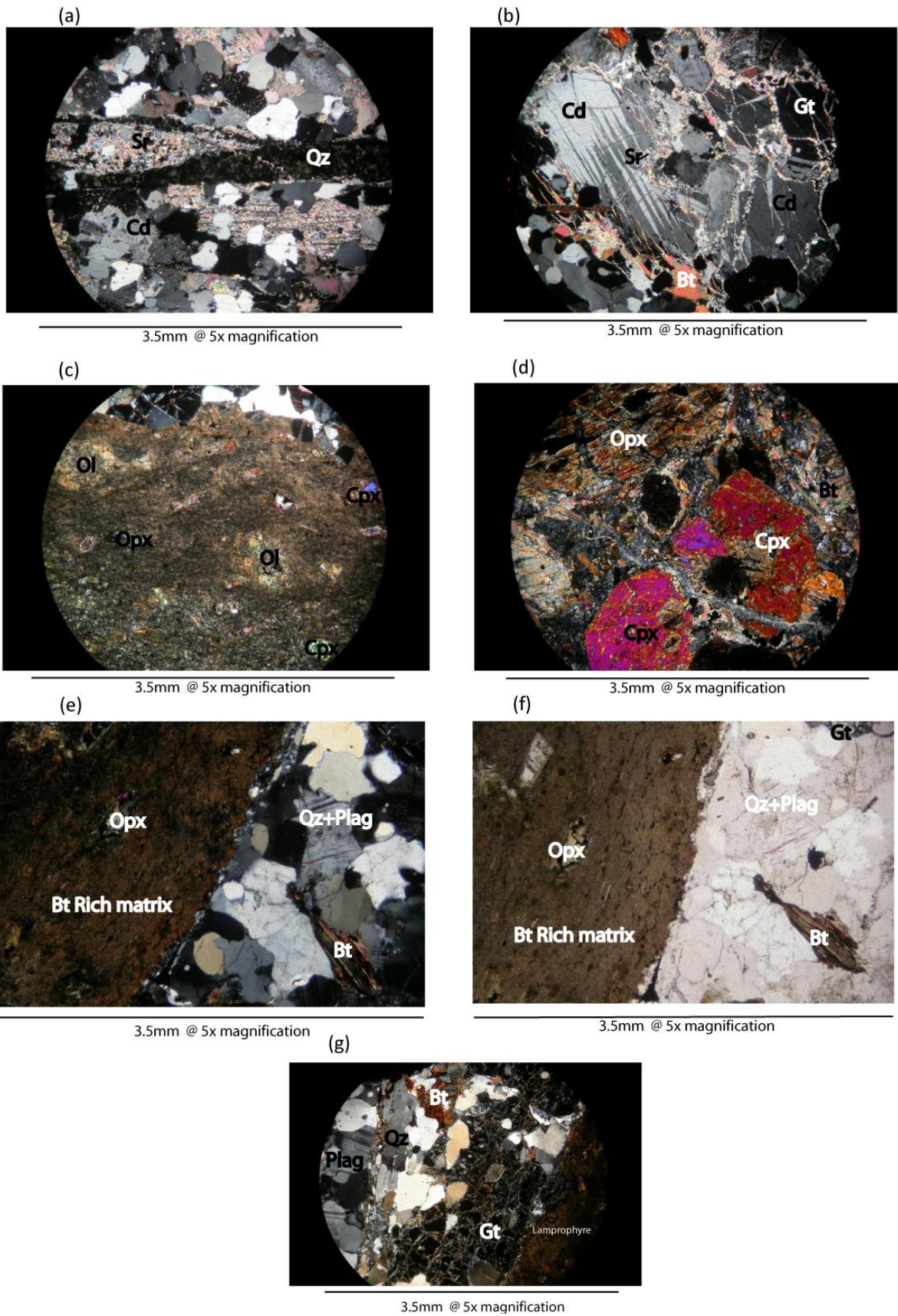
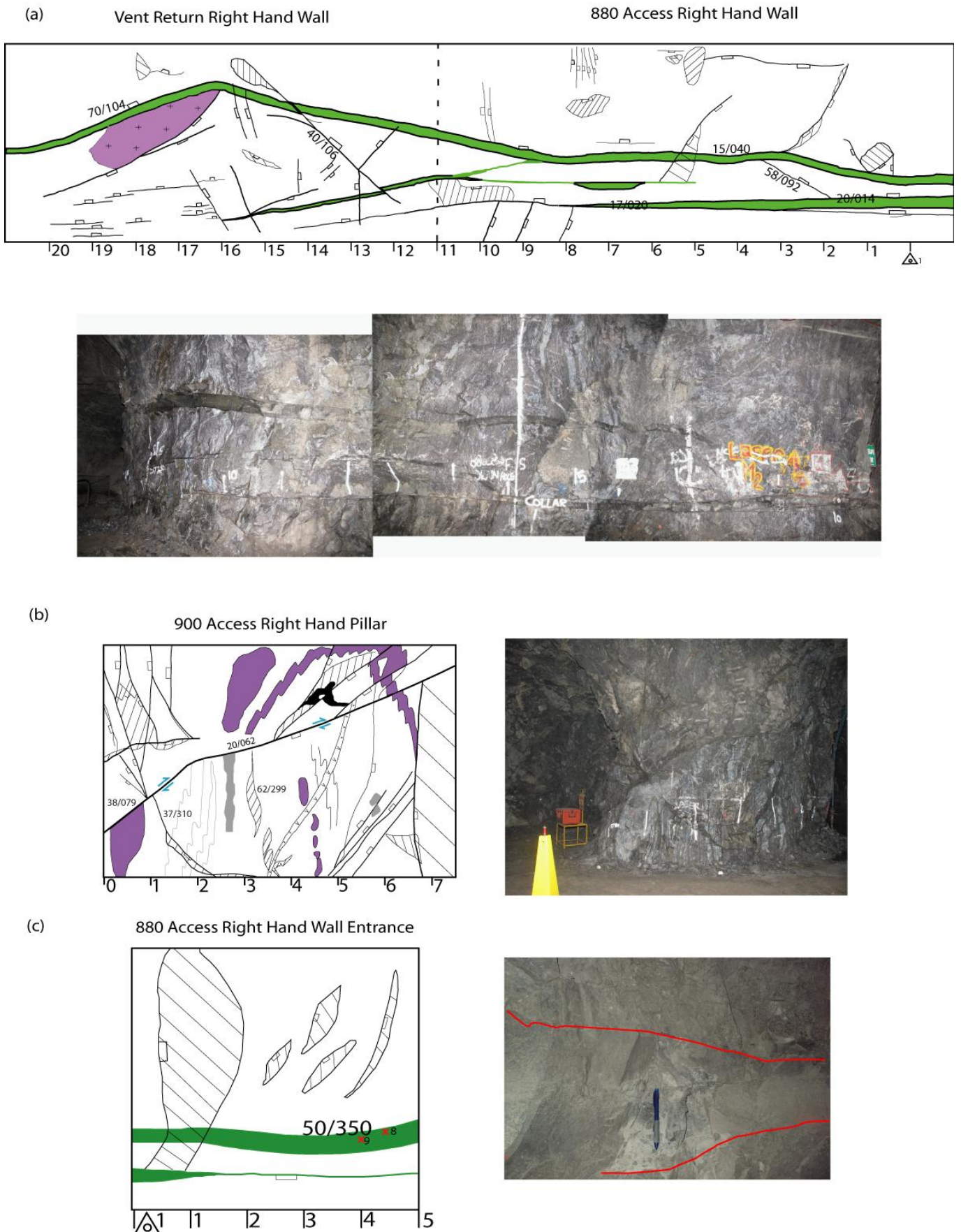




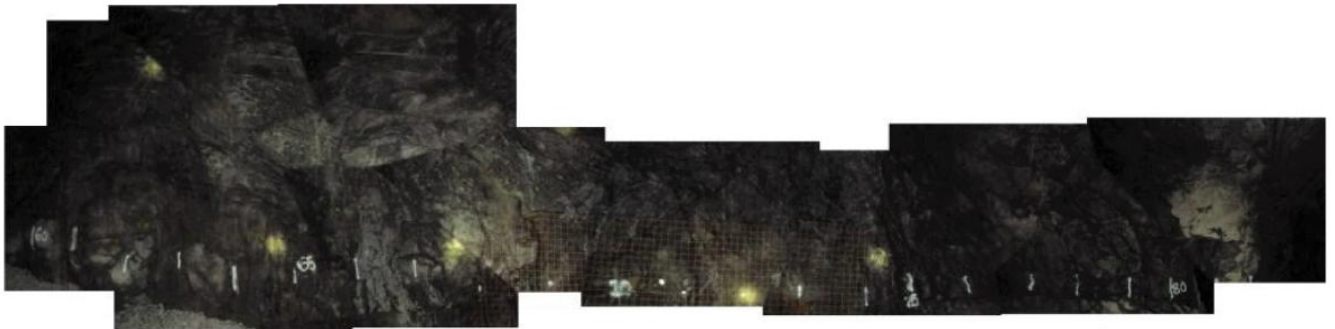
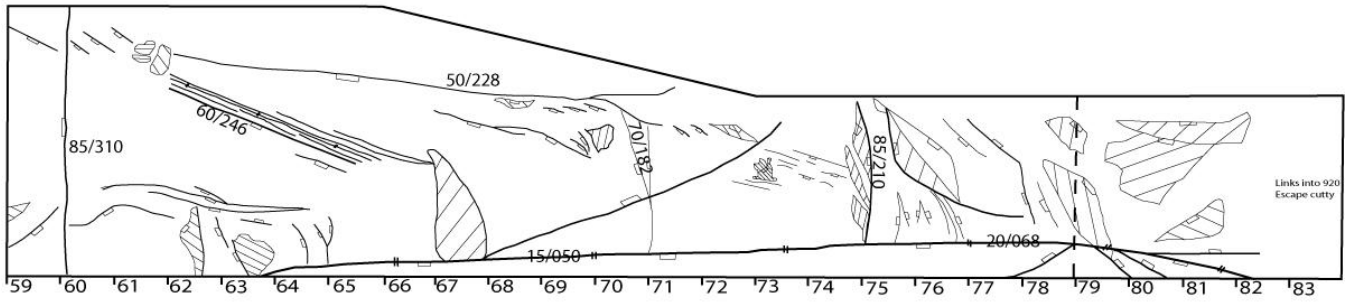
Figure 3: Photomicrographs



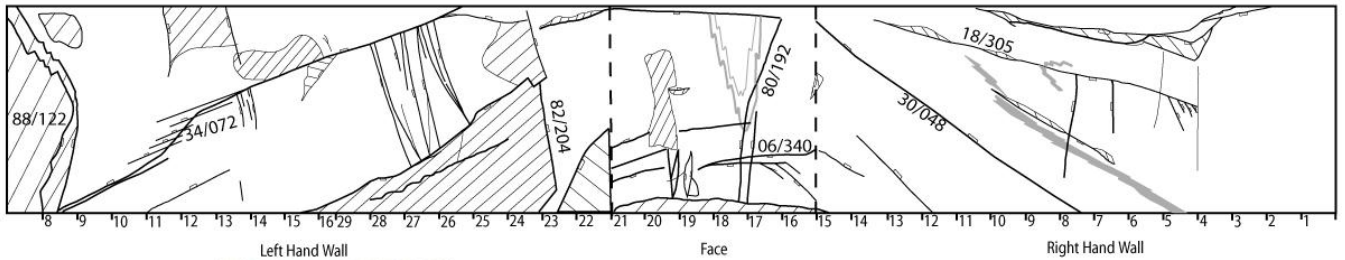
**Figure 4: Wall Maps and Photos of Mapped Area**



(d) 920 Drive Right Hand Wall



(e) 900 Escape Way Access



Images locations within the mine infrastructure

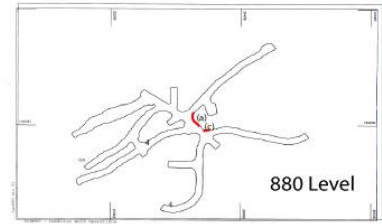
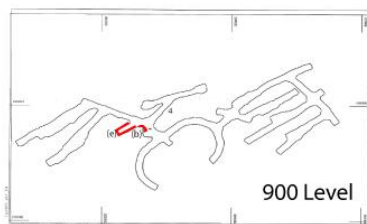
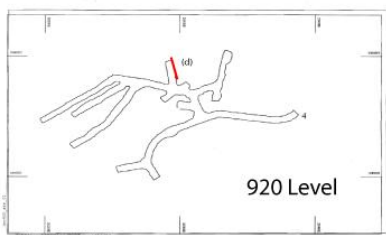


**Figure 5: Field Observations**

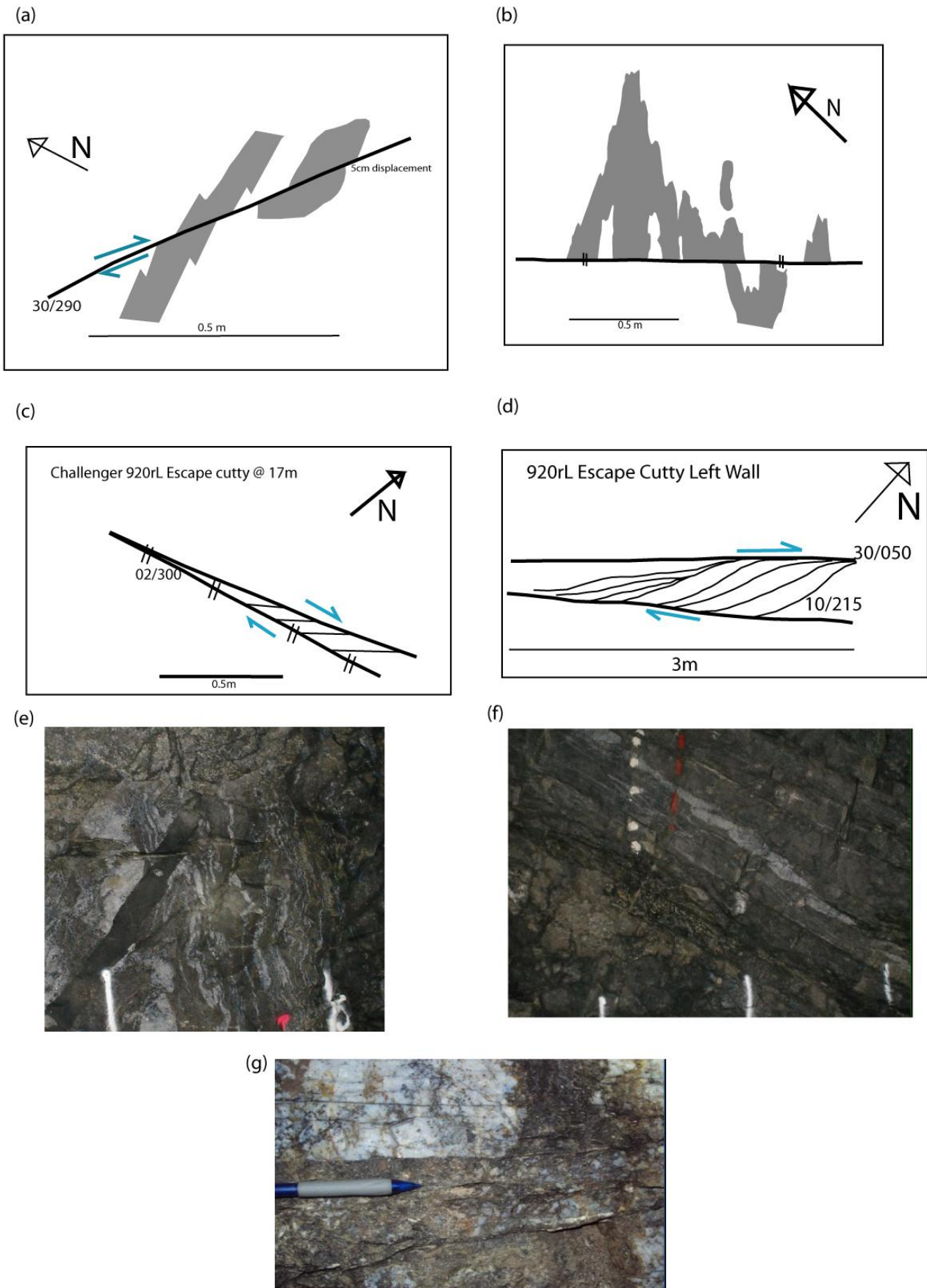
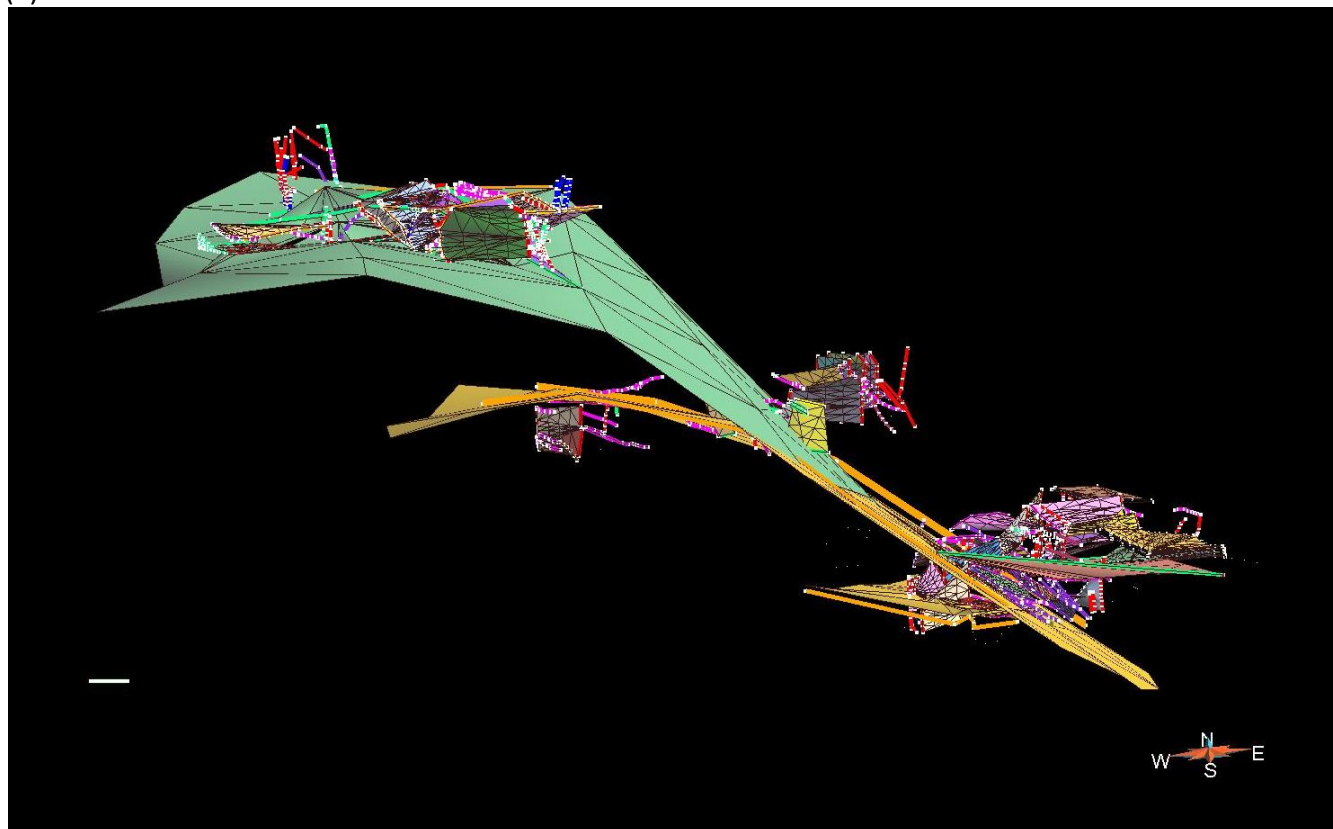


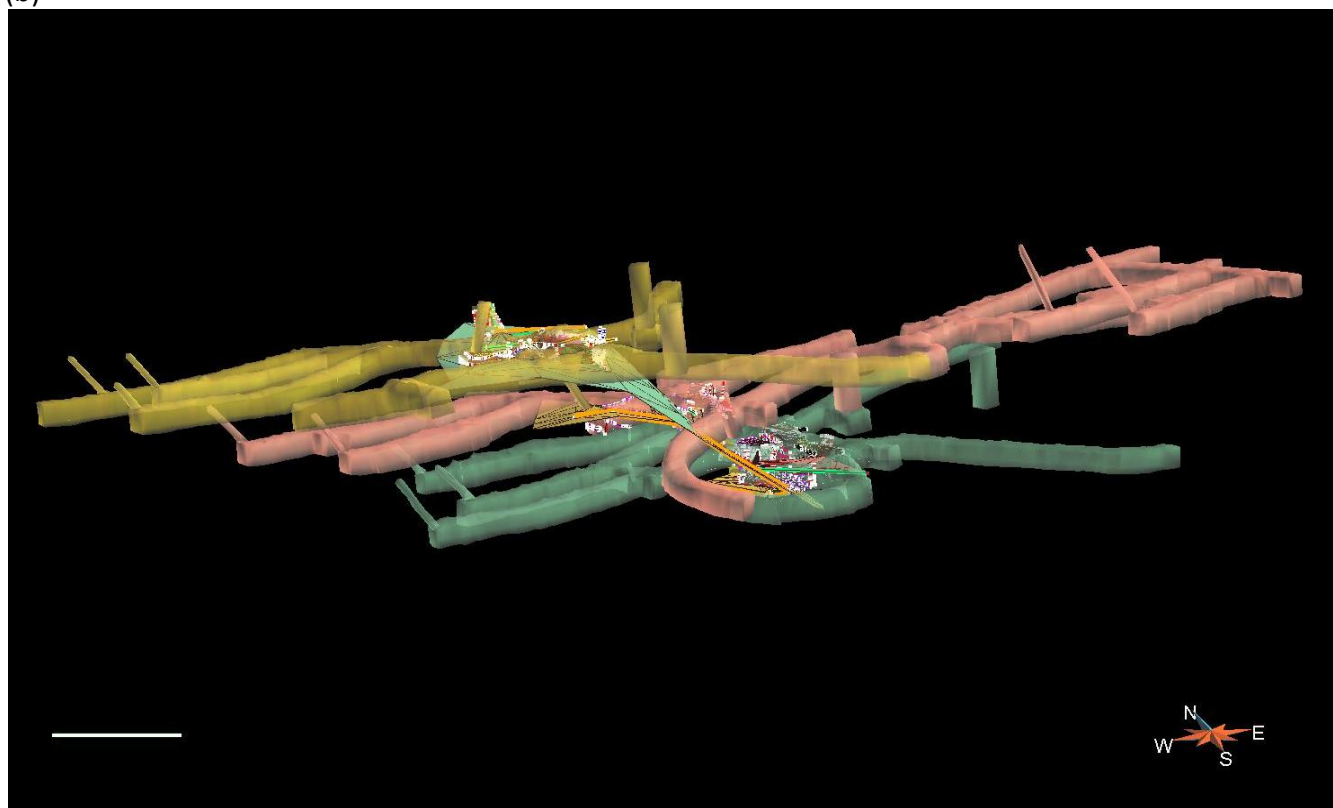
Figure 6: goCad® Model representations and mapped data

(a)



Scale =3.5m

(b)



Scale =30m

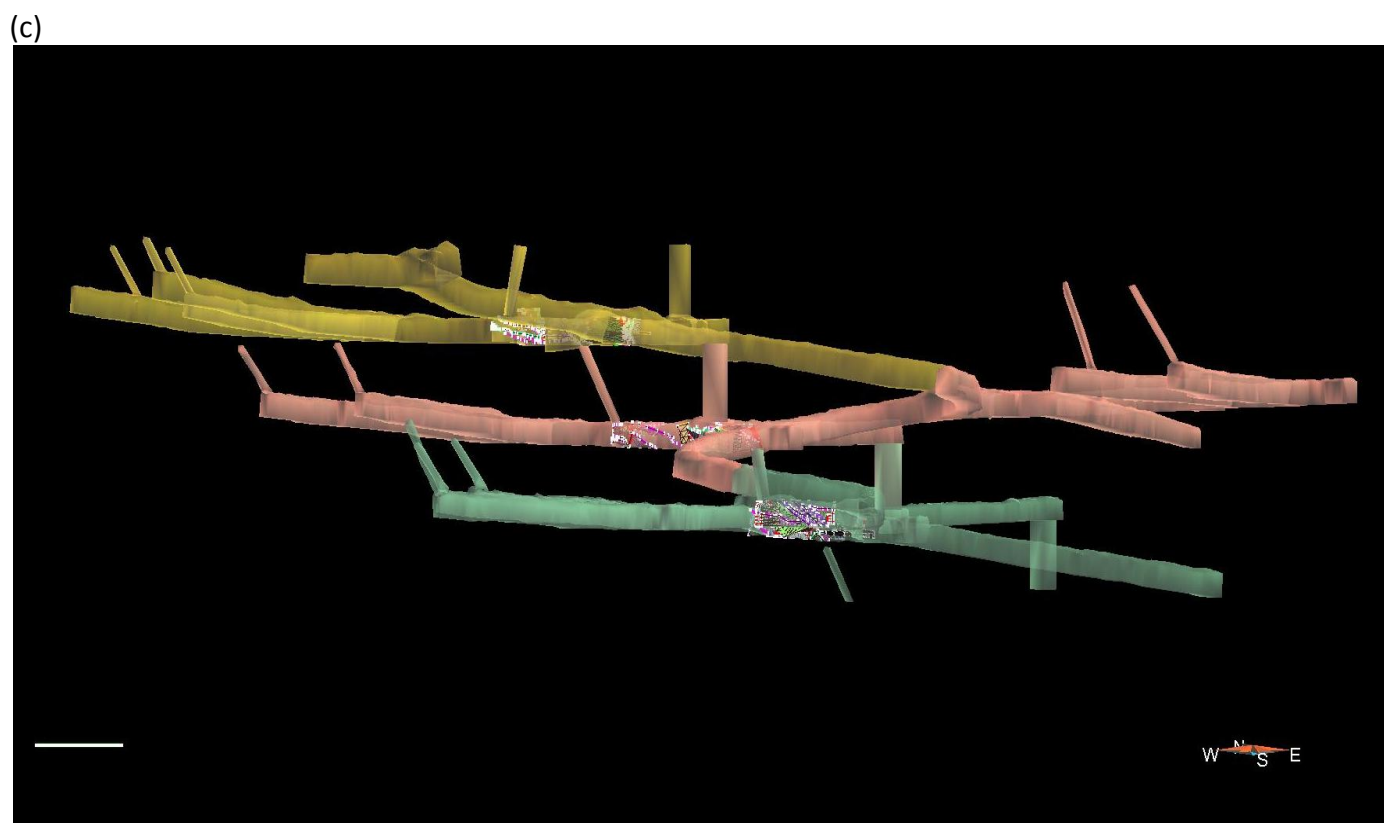


Figure 7: Potential Model Geometries

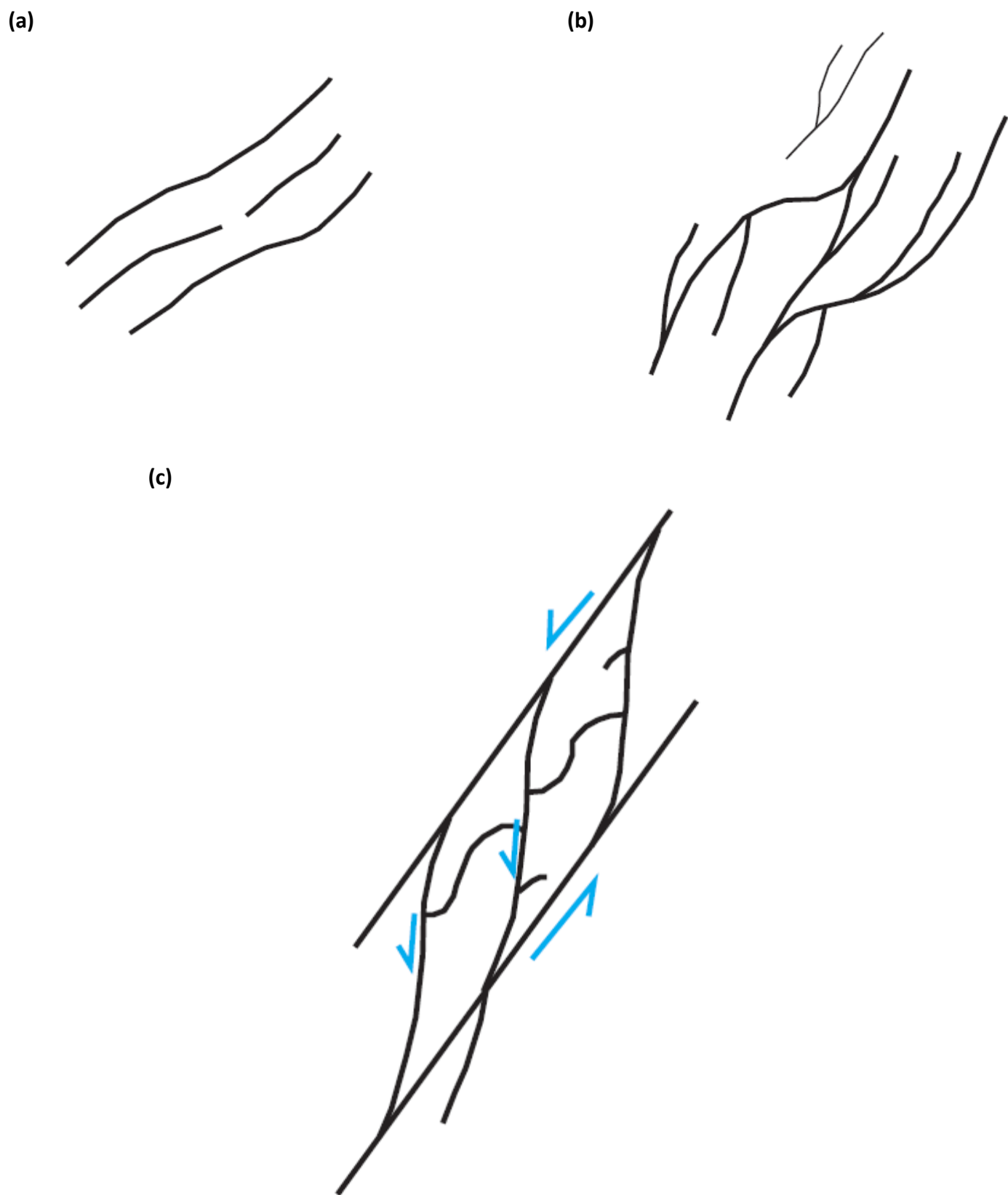
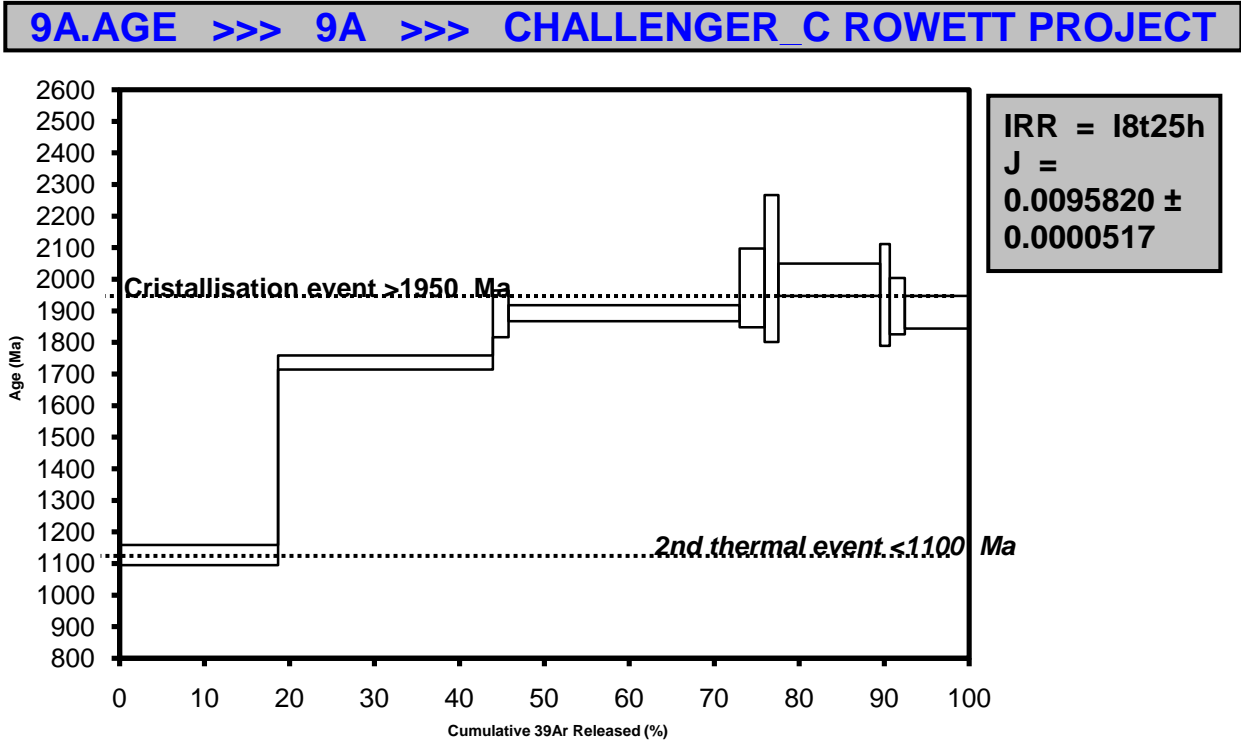
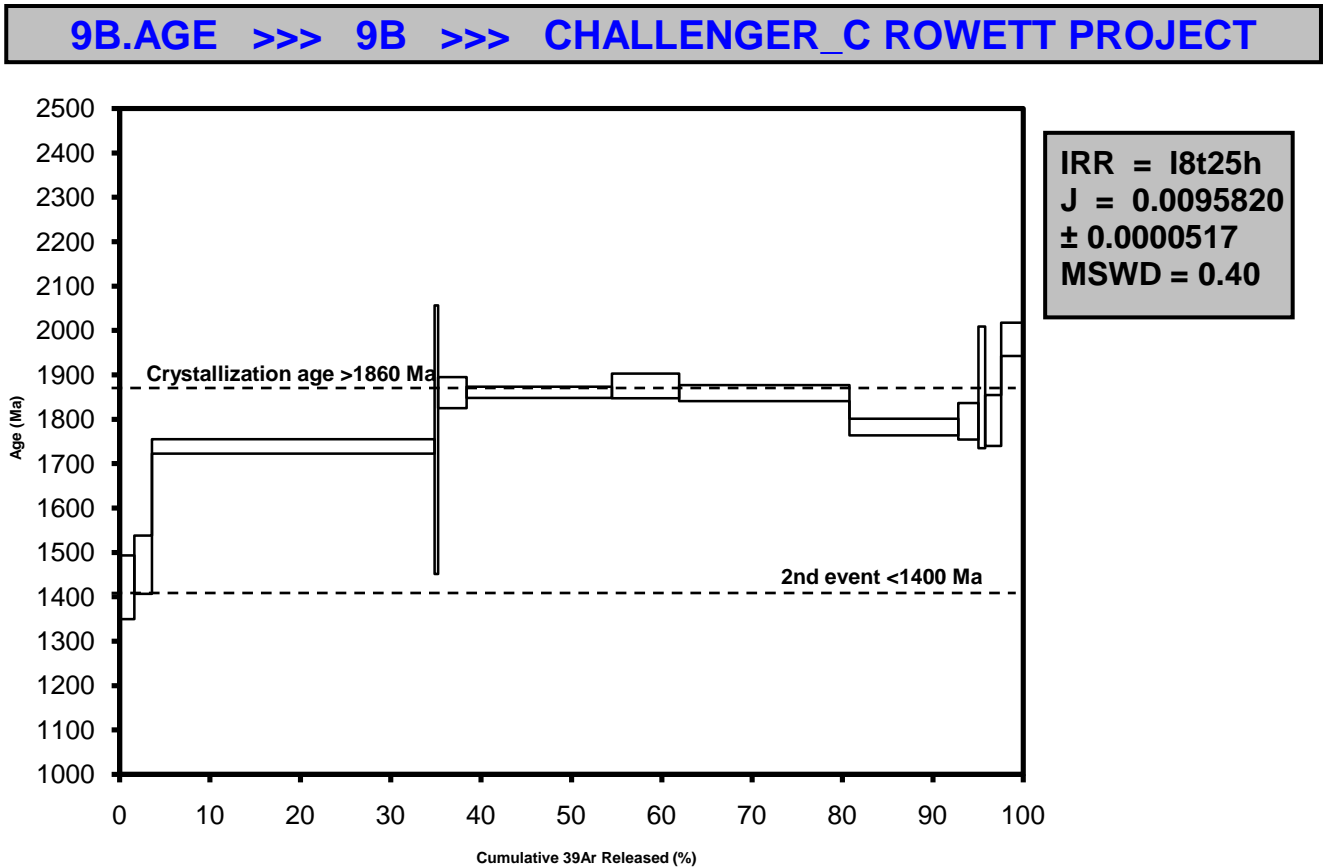


Figure 8: Argon Age Plateau Graphs  
(a)



(b)





(c)

**8.AGE >>> 8 >>> CHALLENGER\_C ROWETT PROJECT**

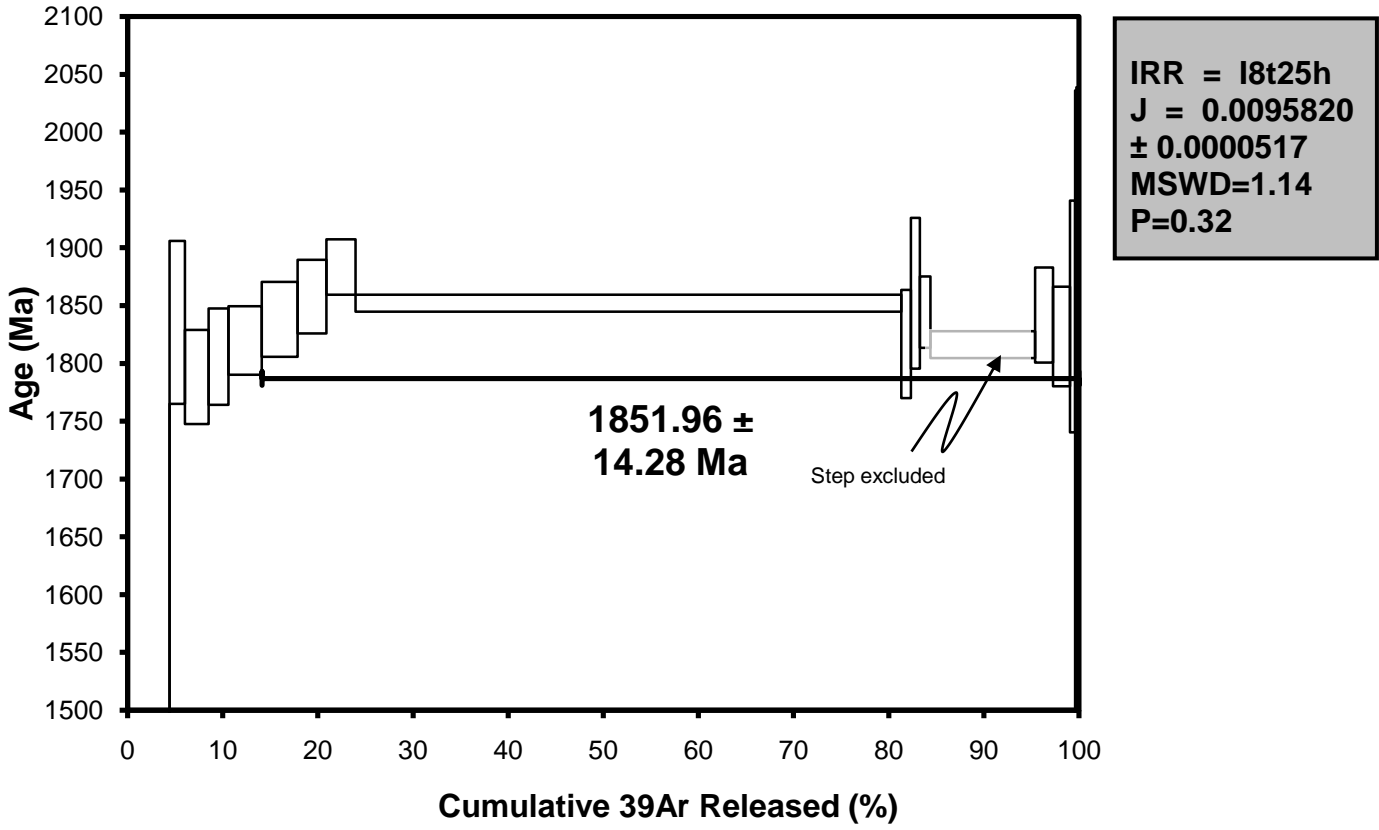
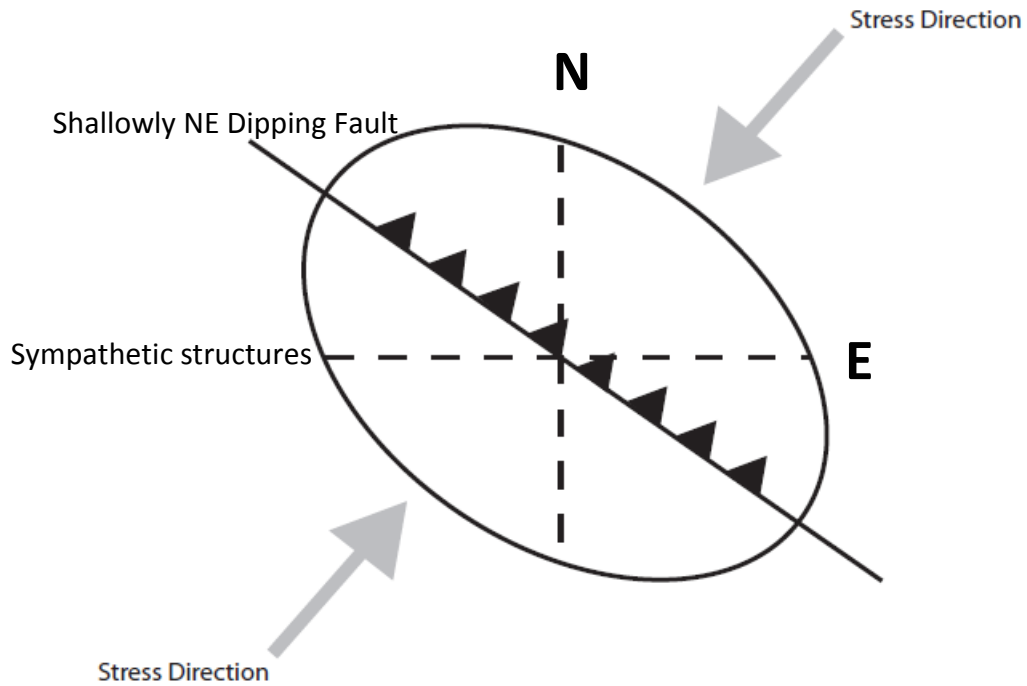
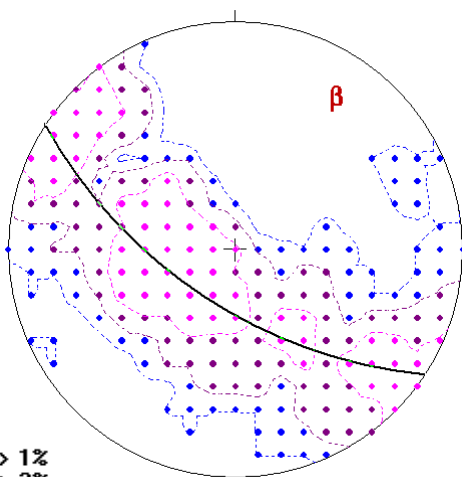


**Figure 9: Interpretation of Stress and Strain**

(a)

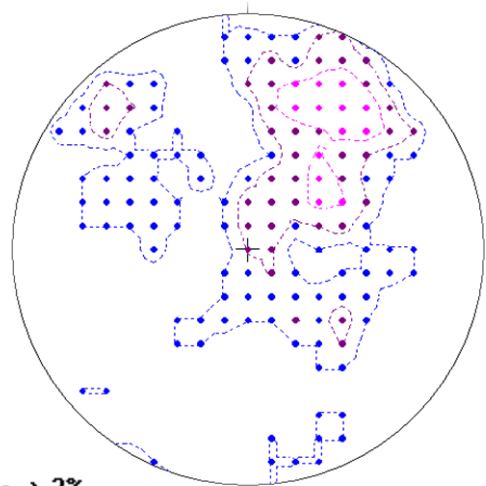


(b)



● --- > 1%  
 ● --- > 2%  
 ● --- > 4%  
 (Max. =7.72%)

(c)



● --- > 2%  
 ● --- > 4%  
 ● --- > 8%  
 (Max. =14.74%)

Figure 10: Cooling History of the Challenger Gold Mine

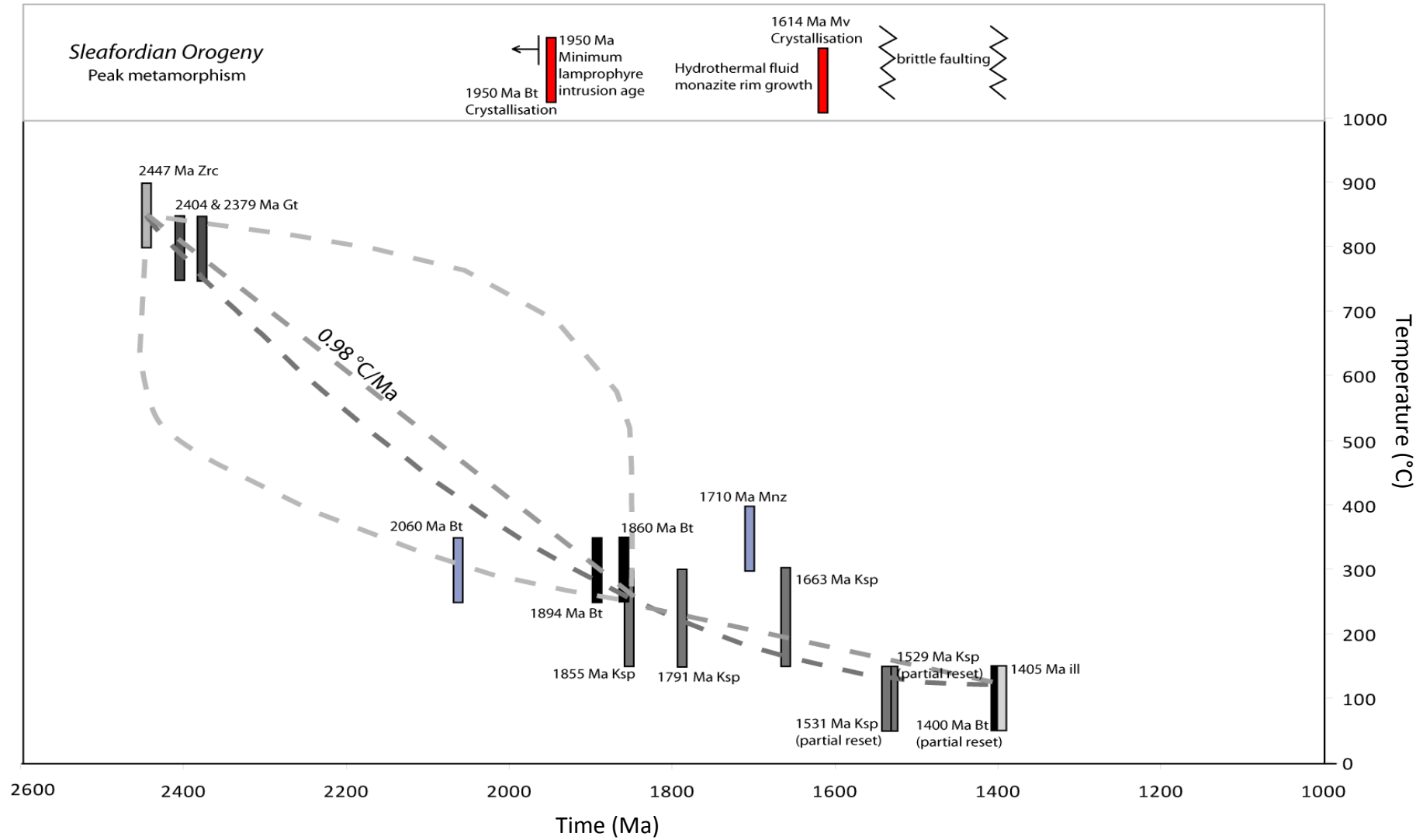


Figure 11: Geological History of Selected Gawler Craton Domains

